ALMA MATER STUDIORUM
UNIVERSITÀ DI BOLOGNA

DOTTORATO DI RICERCA IN

Chimica

Ciclo 36

Settore Concorsuale: 03/C2 – CHIMICA INDUSTRIALE

Settore Scientifico Disciplinare: CHIM/04 - CHIMICA INDUSTRIALE

STUDY AND DEVELOPMENT OF BaCe0.65Zr0.20Y0.1503-Δ (BCZY) – Gd0.2Ce0.8O2- Δ (GDC) DENSE CERAMIC MEMBRANES SYSTEM FOR HIGH TEMPERATURE H2 PURIFICATION

Presentata da: Pio Gramazio

Coordinatore Dottorato

Luca Prodi

Supervisore

Francesco Basile

Co-supervisore

Stefania Albonetti

Esame finale anno 2024

Abstract

Steam Reforming streams must be separated to purify H_2, and the commercially available technologies are pressure swing adsorption (PSA) and cryogenic distillation. Unfortunately, these are only suitable for continuous and large-scale operation [1]. In this scenario membranes attract much interest as they show low cost and low energy consumption [2], combined with a more scale down flexibility. The use of inorganic dense mixed proton-electron conducting ceramic membrane (DPECCM) shows great promise for membranes technology. It has been demonstrated that these membranes show high stability at the operating temperature (550-900°C), full H_2 selectivity and low cost in respect to the Pd-based technology. Previously, Montaleone *et al* [3] investigated, for the first time, $BaCe_{0.65}Zr_{0.20}Y_{0.15}O_{3-\delta}$–$Gd_{0.2}Ce_{0.8}O_{2-\delta}$ (BCZY–GDC) composite with a planar asymmetrical architecture as a hydrogen separation membrane in the 600 °C to 750 °C temperature range.

In literature the employment of Pt catalyst, deposited on ceramic membranes, is deemed necessary in order to avoid surface kinetic effect. It has been previously reported that the Pt catalyst is active in the reaction of Water Splitting. Some interesting literature works observed an effect of Pt morphology, and different metallic species. Nevertheless, detailed information on morphology and catalyst amount is generally lacking in literature papers, and the role of the catalyst is confined to the adsorption kinetics limitations. A detailed investigation was conducted to study the technique of catalyst deposition and its potential impact on the observable phenomenon of hydrogen permeation. The study also examined the influence of the characteristics of the porous layer. This investigation seeks to comprehensively consider all the factors that contribute to the apparent hydrogen permeation. The author's intent is to determine a suitable combination of separation conditions, membrane architecture and catalyst deposition method to achieve industrially attractive H_2 permeated flows.

The approach selected for conducting experiments focused on the effect of crucial factors: temperature, H_2 partial pressure, streams configuration, membrane architecture and Pt catalyst amount and deposition method. The permeation measurements were carried out in a double chamber quartz reactor, where H_2 was separated from a mixture of H_2-He, using argon as sweep gas. Both currents were saturated in water at 28°C to provide steam that also participates in the separation mechanism. The separation was conducted at atmospheric pressure, employing a feed composition of 20%, 50% and 80% H_2 in He (w/w %).

The first main conclusion drawn from this dissertation concerns the amount of Pt deposited on the asymmetric layer of membrane produced by tape casting porosity shaping method. Three different amounts were investigated (0.15, 1.5 and 4.5 mg cm^{-2}). The most optimal performance, based on H_2 permeation performances, was attained when 1.5 mg cm^{-2} of Pt was deposited on the porous layer, resulting in a 0.642 mL $min^{-1}cm^{-2}$ permeated H_2 when 80% H_2 in He was employed as the feed. Pt deposition method is influenced by the concentration of the Pt precursor, which results in different morphology of the catalyst. In particular, high precursor concentration causes formation of Pt agglomerates, which in the end cause less effective Pt catalyst particles for WS reaction at high temperatures.

The second development focused on further optimization on tape casting membranes concerning the solvent employed for the Pt catalyst deposition. The same concentration of Pt was employed, depositing 1.5 mg cm^{-2} on the porous side of the membrane, but a mixture of acetone and water was employed as solvent. This mixture allowed the suppression of effects leading to poorly dispersed particles that in the previous experiments affected negatively permeation performances, in particular at higher Pt concentration. As a result, it was possible to achieve 0.74 mL $min^{-1}cm^{-2}$ at 750°C with 50% H_2 in He.

Lastly, first-ever permeation performance measurements into an innovative ceramic membrane type for hydrogen separation was investigated. In-depth research was done on a group of hierarchically-structured $BaCe_{0.65}Zr_{0.20}Y_{0.15}O_{3-\delta}$(BCZY) - $Gd_{0.2}Ce_{0.8}O_{2-\delta}$(GDC) membranes produced by freeze casting porosity shaping method. Membranes were thoroughly investigated observing the effect of deposition solvent and the effect of porous layer thickness. Employing a mixture of Acetone and water resulted in better hydrogen permeation at temperatures (T > 650°C), reaching 0.26 mL $min^{-1}cm^{-2}$ at 750°C with 50% H_2 in He. The reduction of porous layer thickness led to a hydrogen apparent permeated flow of 0.33 mL $min^{-1}cm^{-2}$, at 750°C with 50% H_2 in He (%vol), with both streams humidified at 28°C.

The results of this investigation have demonstrated that the metallic catalyst—which is frequently employed in literature to get around surface kinetics constraints—is directly related to membrane permeation performance. This discovery could fundamentally alter our understanding of membrane technology and its uses, with far-reaching consequences. Besides, this study emphasizes how important it is to have a deeper comprehension of the basic principles guiding the interaction between catalysts and membranes.

Summary

1. Introduction

1.1 World population and energy consumption

The magnitude of the world population has increased nearly three-fold since the mid-twentieth century. Specifically, the global human population has risen to 8.0 billion individuals as of mid-November 2022, in contrast to a mere 2.5 billion people estimated to have existed in 1950. This exponential growth has significant implications for the well-being of the planet and the sustainability of its resources[4] (Figure 1a.). The rise in the number of individuals who survive to reproductive age, the gradual extension of human lifespan, the increasing trend of urbanization, and the accelerating pace of migration are all linked to the significant growth in resource consumption. It is evident that power generation, which plays a crucial part in the industrial development of any nation, poses a clear challenge (Figure 1b) [5].

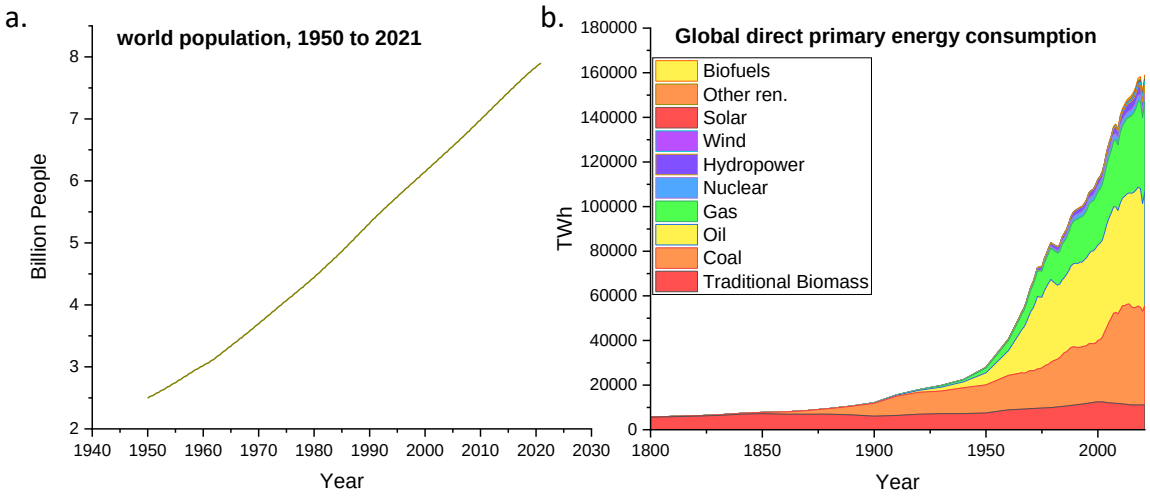

Figure 1 Time series for world population and energy consumption (adpt.)[6], [7].

The expanding energy demand is being partly met by fossil fuels, which confront formidable obstacles such as depletion, geographical constraints on extraction, and a rise in the emission of Greenhouse Gases (GHG) that causes global warming [8], [9]. Even though population growth is facing a gradual small decline, it is urgent to find sustainable development means for human society. Hydrogen has the potential to provide economically feasible, socially advantageous and energetically efficient solution[10], and could be potentially considered as a pillar of the energy transition, a critically needed process to contrast global warming and other problems linked to traditional energy system[11]. As mentioned, hydrogen systems could potentially have significant roles during the energy transition[12], and some are listed hereafter:

- Renewable energy integration to existing infrastructure with multigeneration approach[13]–[15].
- Accessible, reliable, safe and resilient energy system to all sector and regions[16].
- Cleaner energy source for transportation, industrial application, and residential application[17]–[20].

Renewable Energy (RE) resources will be crucial in the shift to a clean and sustainable energy system[21], [22]. However, variable and intermittent nature of RE resources poses the main challenge in transitioning towards entirely RE systems[23], [24]. Generally, RE based energy production are more susceptible to potential system interruption or drops in performance to a greater extent if compared to other energy sources, like nuclear, coal or natural gas. Energy demand fluctuates with the time of the day but never falls below a certain value, referred as base load. A possible solution to the incompatibility of RE and energy demand can be seen in employing hydrogen as energy carrier, exploiting the possibility to store, transport and then utilize it to cope with the balancing variable supply and variable demand[22], [25]–[27].

1.2 Hydrogen and current production processes

Hydrogen is the most prevalent element in the universe and is mostly found in water and organic molecules on planet earth[21], [28]. In the realm of literature and academic discourse, hydrogen molecule (H_2) is often lauded for its high energy density. This is particularly evident when comparing energy density by weight, as H_2 boasts an impressive 120 MJ kg^{-1} at 298 K, while the more conventional hydrocarbon fuel, gasoline, only manages 44 MJ kg^{-1} at the same temperature. However, it is important to note that while hydrogen may have a higher energy density by weight, its energy density by volume pales in comparison to hydrocarbon fuels like gasoline, with liquid hydrogen only possessing approximately four times less energy density by volume (namely 8 MJ L^{-1} while gasoline 32MJ L^{-1}).[29]–[32]. This last piece of information implies that in order to store it, larger tanks are necessary[33], [34]. Not only this happens to be inconvenient but destructive capability (hydrogen embrittlement) and escape properties due to small molecule size coupled with flammability pose large risks associated with its usage[35]. Lastly, it is worth reporting that the liquefaction temperature is 20.25 K, requiring sophisticated insulated vessels to be transported. The production of hydrogen (Figure 2) can be classified into three main categories defined by colours, such as green (RE-based hydrogen production), pink or purple (nuclear energy-based hydrogen production) and blue (coal gasification and natural gas-based hydrogen production integrated with carbon capture and storage (CCS)[5], [36]. Other technologies that rely on coal gasification and natural gas-based hydrogen production devoid of carbon capture and storage are defined as grey hydrogen productions, while, using black coal or lignite (brown coal) in the hydrogen-making process provides black or brown hydrogen[37]. The last group is considered the most environmentally damaging of the whole colour spectrum. It should be emphasized that hydrogen produced from fossil fuels using the gasification method is occasionally referred to as black or brown hydrogen, with the terms being used interchangeably, adding another degree of complexity to an already unnecessary, deliberately convoluted classification.

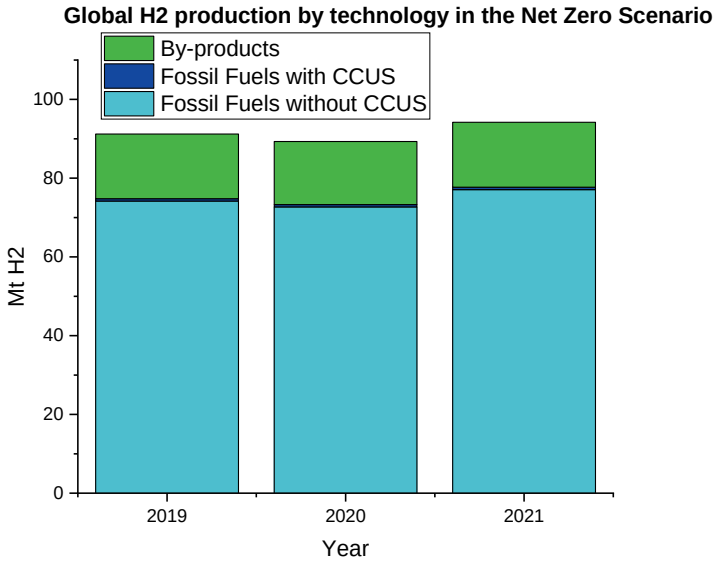

Figure 2 Global Hydrogen production by technology in the Net Zero Scenario (adpt.)[38]

At present, the majority of hydrogen (95%) is generated through the utilization of non-renewable resources such as fossil fuels, with natural gas reforming, methane partial oxidation and coal gasification being the primary methods employed [5]. The primary mechanisms that safeguard the worldwide hydrogen requirement undergo a transformation as they are substituted or assimilated with carbon capture and storage (CCS) or carbon capture and utilization (CCU) processes that detain carbon dioxide emissions that would have otherwise been discharged into the environment.

1.2.1 Natural gas reforming

A substantial portion of conventional produced hydrogen comes from reforming of natura gas and methane partial oxidation. In this process the first step is desulfurization, achieved in Claus plants, where sulphur, normally present in natural gas, is recovered using the Claus process from gaseous H_2S, that reacts with oxygen[39]. The presence of adequate sulphur level in the feedstock may lead to corrosion of the refinery plant, deactivate catalysts in the subsequent chemical steps and lead to air emission of sulphur compounds[40]. The catalyst employed is activated titanium or aluminium oxide and the process can be separate in two stages, one thermal stage followed by a catalytic stage. Reactions happening during the thermal step are reported in Eq. 1.

$$H_2S + \frac{1}{2}O_2 \rightarrow S + H_2O$$

$$H_2S + \frac{3}{2}O_2 \rightarrow SO_2 + H_2O \quad (1)$$

The sulphur dioxide resulting from combustion reacts with gaseous H_2S and elemental sulphur is separated[41]. Catalytic step reaction is reported in Eq. 2.

$$2H_2S + SO_2 \rightarrow 3S + 2H_2O \quad (2)$$

Generally, lower temperatures in the catalytic stage can secure higher conversions, but sulphur deposition on catalyst is a cause of problems, thus dew point temperature is employed, with multiple stage design, combined with condensation and removal of sulphur for each stage[226]. If

the Sulphur is present as H_2S then reaction with an oxide (ZnO) or scrubbing with a solvent might be applied[241].

The following step is hydrocarbon reforming, to produce hydrogen through different paths. The first one is steam methane reforming (SMR), where steams reacts with natural gas at high temperatures (700-1000 °C)[42] to form carbon monoxide and hydrogen gas, with an endothermic reaction[227]:

$$CH_4 + H_2O \rightarrow CO + 3H_2 \quad (3)$$

The produced carbon monoxide then reacts with steam, in water gas shift (WGS) reactor, to further convert CO to carbon dioxide so that additional hydrogen can be generated[43]. The WGS reaction exhibits an exothermic nature and is conventionally executed in a two-fold manner: a stage characterized by high temperature shift (HTS) and a stage characterized by low temperature shift (LTS). The HTS stage is customarily performed within the temperature range of 350 to 450°C over iron-based catalysts, while the LTS stage is executed within the temperature range of 200 to 250°C, over copper-based catalyst[44]. The efficacy of the WGS reaction is significantly contingent upon the temperature of the catalyst bed. In the event that the temperature is excessively low, the reaction will not advance expeditiously enough to be deemed advantageous. Conversely, if the temperature is excessively high, the catalyst may incur damage or the reaction may yield undesirable by-products[44].

$$CO + H_2O \rightarrow CO_2 + H_2 \quad (4)$$

It is worth noticing that SMR it necessitates a substantial quantity of energy and results in the generation of a notable volume of carbon dioxide[227]. Commercial catalyst for SMR are generally based of heterogeneous nickel[228]. A simplified P&ID of a typical unit for SMR is reported hereafter.

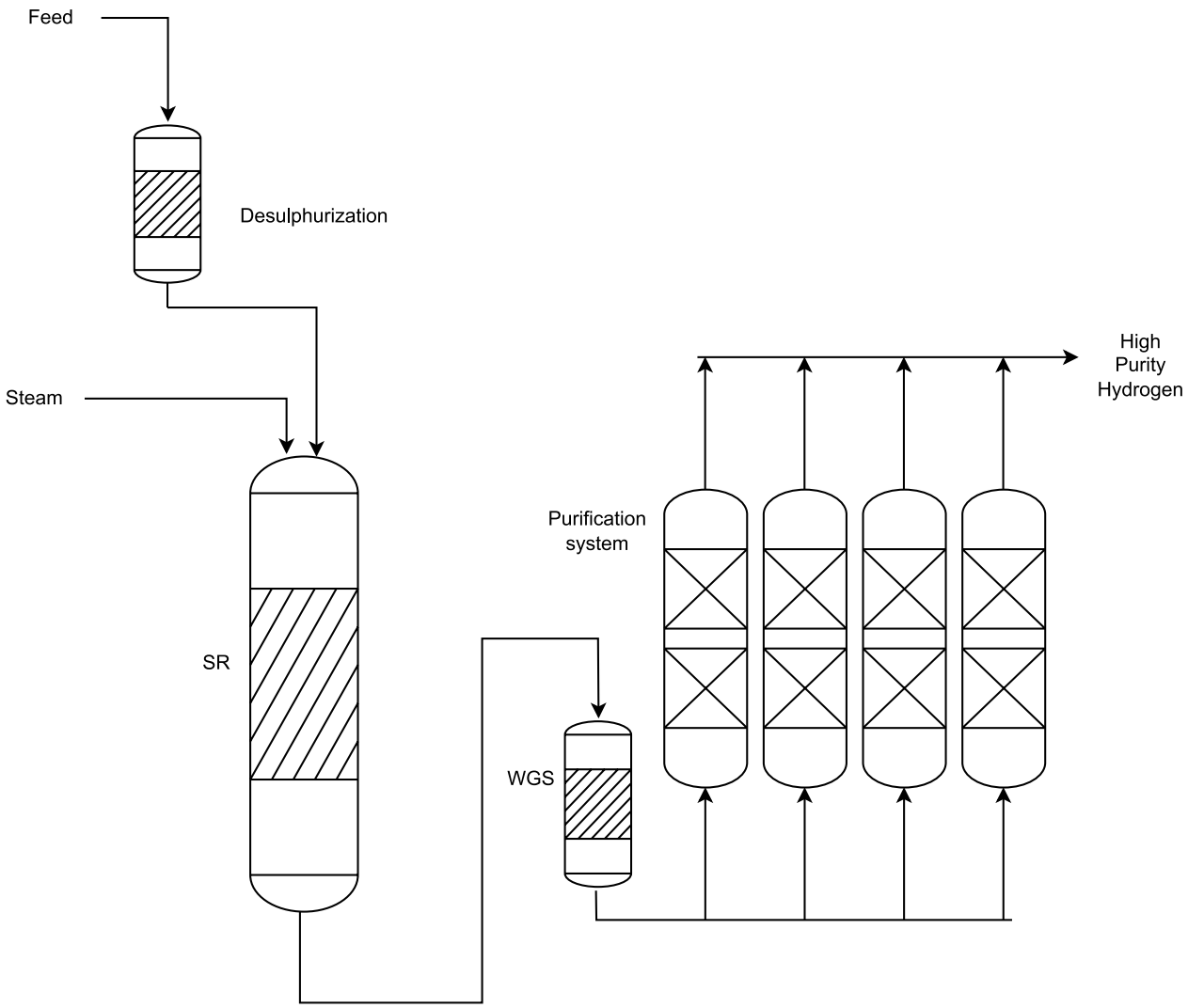

Figure 3 Simplified P&ID of a typical unit of Steam Reforming of Methane [adpt.][227].

The second alternative reaction is known as partial oxidation (POx), with exothermic nature[227]. It basically involves the conversion of hydrocarbons, steam and oxygen into to hydrogen and carbon oxides. Temperature of the process depends on the feedstock. Generally, it is possible to carry the reaction in presence and absence of catalyst, in the first case at 950°C operating with feedstock ranging from methane to naphtha, in the latter at 1150-1315°C, allowing operation with hydrocarbons including methane heavy oil and coal (Eq. 5).

$C_nH_m + \frac{1}{2}nO_2 \rightarrow nCO + \frac{1}{2}mH_2$ (catalytic)

$C_nH_m + nH_2O \rightarrow nCO + \left(n + \frac{1}{2}m\right)H_2$ (non catalytic) (5)

After the removal of sulfur, the process employs pure oxygen to partially oxidize the hydrocarbon feedstock. The resulting syngas is further treated in a manner similar to the product gas of the sulfur removal SR process. The high capital intensity of this plant is attributed to the costs of the oxygen plant and the additional expenses associated with the desulfurization steps. A base simplified P&ID of a unit of POx of hydrocarbon is reported hereafter.

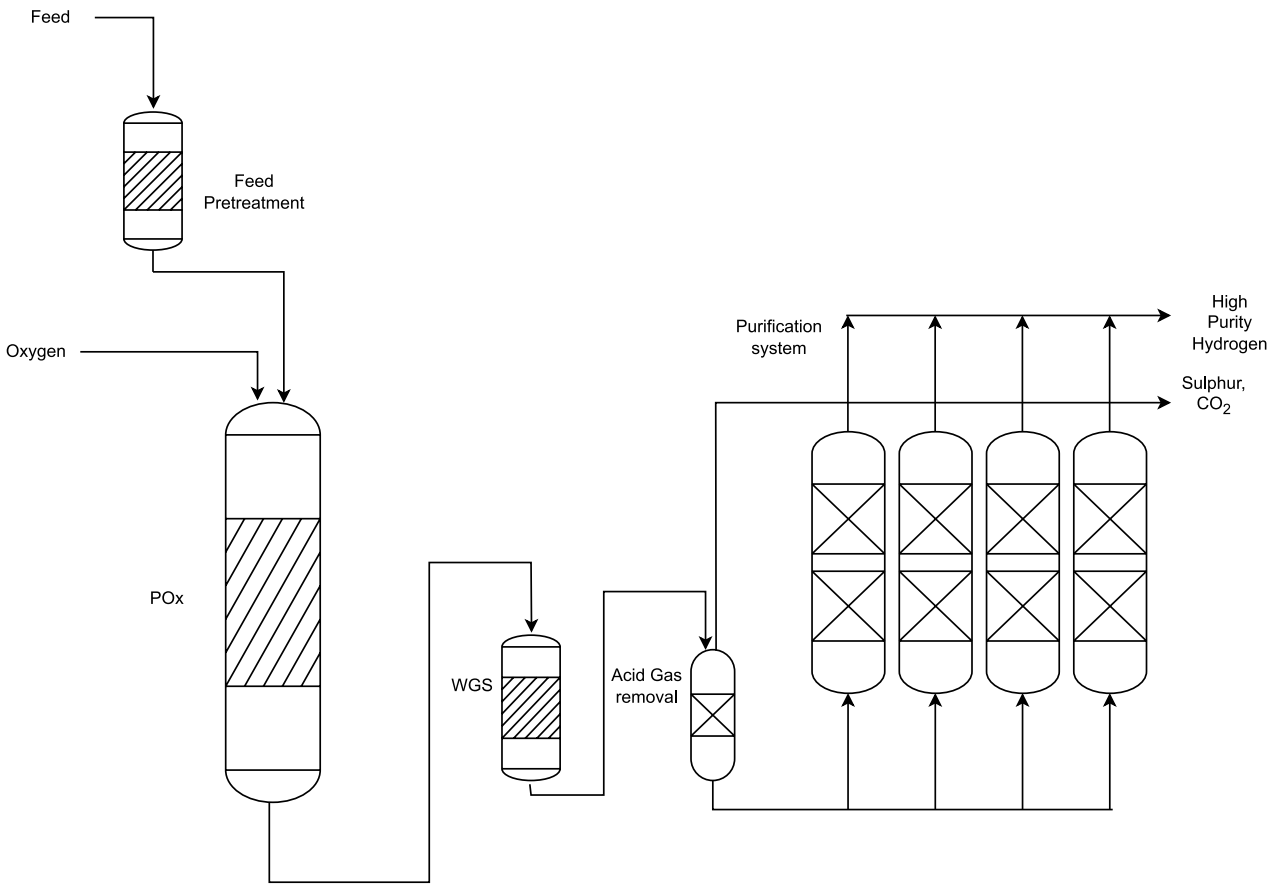

Figure 4 A base simplified P&ID of a unit of POx of hydrocarbon.

Lastly, the Autothermal Reforming (ATR) method is a process that utilizes the exothermic partial oxidation to provide heat and the endothermic steam reforming to increase hydrogen production (Eq. 6). This process involves injecting steam and oxygen or air into the reformer, which causes the reforming and oxidation reactions to occur simultaneously.

$$C_nH_m + \frac{1}{2}nH_2O + \frac{1}{4}nO_2 \rightarrow nCO + \left(\frac{1}{2}n + \frac{1}{2}m\right)H_2 \quad (6)$$

ATR conditions are typically more challenging than those for conventional reforming, necessitating very robust hardware and catalysts. Commercial catalysts are based on mixed oxides of non-noble metals[229]. A simplified P&ID of an ATR unit is reported hereafter[250].

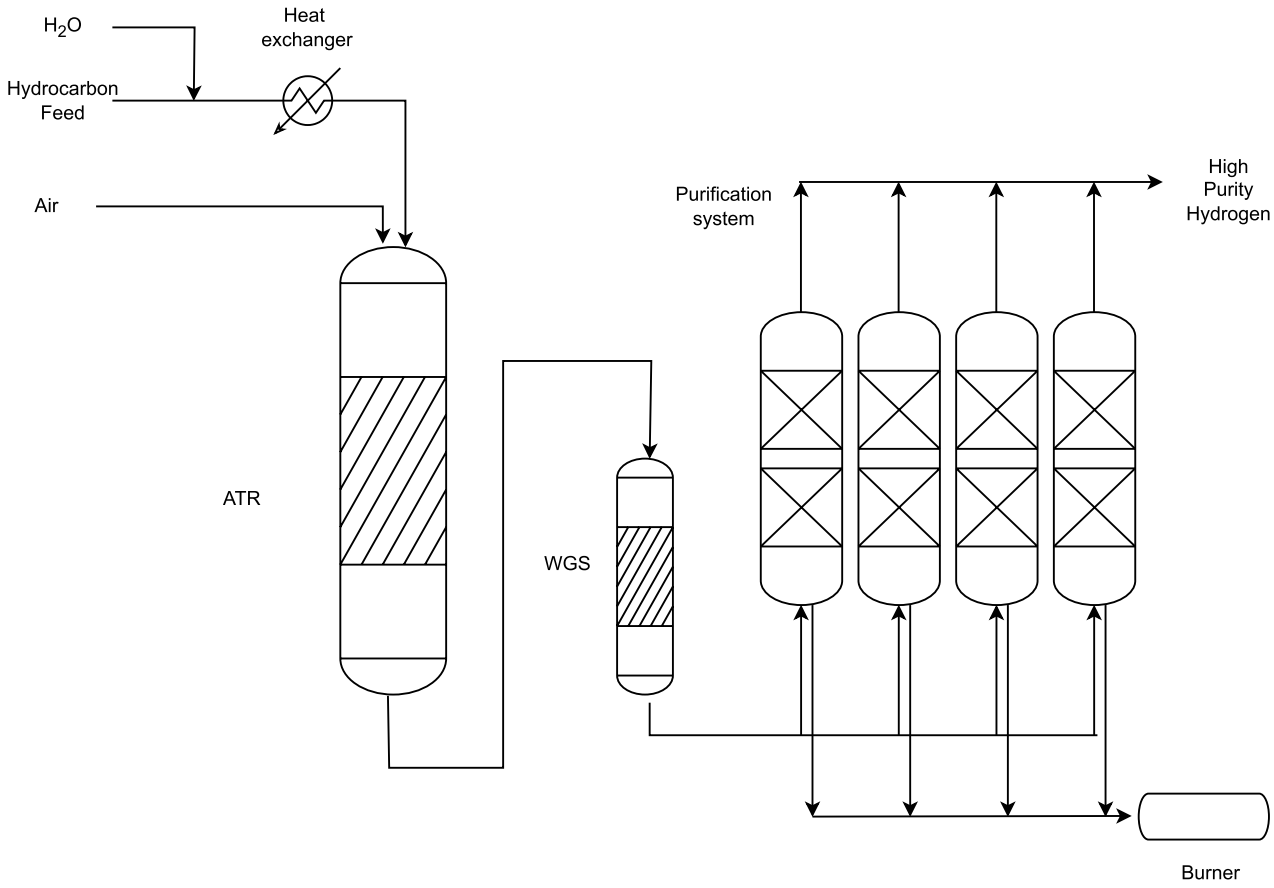

Figure 5 Simplified P&ID of an ATR unit [adpt.][230].

In order to keep the process carbon neutral and to label the produced hydrogen as "blue", natural gas reforming has to be integrated with carbon capture and storage technique to avoid CO_2 emission in the environment[45].

1.2.2 Coal gasification

Gasification of coal is another conventional method of hydrogen production. The first step of this process consists in air separation by conventional separation technologies, such as membrane separation, cryogenic air separation or pressure swing adsorption[5]. Subsequent step consists in coal pyrolysis where two inputs of steam and oxygen are required to react with coal to produce two main products, such as volatile matter and char. Volatile matter (represented by generalized chemical formula C_6H_6) includes moisture and tar[46]. Pyrolysis reaction is reported hereafter:

$$Coal \rightarrow Char + (C_6H_6 + H_2 + CO + H_2S + CO_2 + N_2 + CH_4 + H_2O) \quad (7)$$

After the pyrolysis, combustion of volatile matter happens as follows[46]:

$$C_6H_6 + 7.5O_2 \rightarrow 6CO_2 + 3H_2O \quad (8)$$

$$H_2 + 0.5O_2 \rightarrow H_2O \quad (9)$$

$$CO + 0.5O_2 \rightarrow CO_2 \quad (10)$$

$$CH_4 + 2O_2 \rightarrow CO_2 + 2H_2O \quad (11)$$

Next step is reaction of char elemental decomposition products (Eq. 7), products of volatile combustion, gasification oxidant and the gasification agent as follows[46]:

$$C + O_2 \rightarrow CO_2 \quad (12)$$

$$C + 0.5O_2 \rightarrow CO \quad (13)$$

$$C + H_2O \rightarrow CO + H_2 \quad (14)$$

$$C + CO_2 \rightarrow 2CO \quad (15)$$

$$C + 2H_2 \rightarrow CH_4 \quad (16)$$

$$S + H_2 \rightarrow H_2S \quad (17)$$

$$CO + H_2O \rightarrow CO_2 + H_2 \quad (18)$$

$$CH_4 + H_2O \rightarrow CO_2 + 3H_2 \quad (19)$$

Net result of Eq. 11-19 is exit of raw syngas from the gasifier. An acid gas removal is necessary to subtract hydrogen sulfide (H_2S) and carbon dioxide (CO_2). Potential heat recovery could be present due to next step being rapid quenching process trough rapid cooling of the exit stream. This step is necessary to reach WGS optimal reaction conditions. Generally, temperature of coal gasification can vary from below 1000°C to above 1200°C[231] while WGS reaction is instead conducted in two different temperature stage, one in the range 320-450°C and one in the range 150-250°C[232].

Following water gas shift unit converts CO to CO_2 and H_2O into H_2. Hydrogen purification is typically achieved employing pressure swing adsorption process. Similar to what previously mentioned with natural gas steam reforming, to keep the process carbon neutral and to label the produced hydrogen as “blue”, natural gas reforming has to be integrated with carbon capture and storage technique to avoid CO_2 emission in the environment [45].

1.2.3 Nuclear Energy-based production process

Nuclear fission inside the nuclear reactor generates energy trough steam that gets converted by using turbines. Energy is then employed to feed water electrolysers that produce hydrogen gas. Another alternative is to utilize nuclear produced energy to power fuel cells that produce hydrogen gas. Because nuclear fission does not include direct hydrocarbon fuel-burning it is accepted as non-greenhouse gasses generating. Essentially, nuclear fission of atom inside the reactor core produces thermal energy that is utilized to heat up and vaporize water. Next step is harvesting thermal energy from steam to convert it to electric energy, and the most widely used apparatus is a turbine, as previously mentioned. When hydrogen is produced by electrolysers powered by nuclear reactors the conventional colour code is pink[5], [36].

1.3 Hydrogen, new possibilities.

Hydrogen colour classification determines that green label is to be assigned to renewable energy-based hydrogen productions. In short terms, low-carbon renewable sources generate electricity that is used to feed water electrolysis process. The following paragraph will present a brief description of water electrolysis.

1.3.1 Electrolysis

The electrolyser produces hydrogen by electrochemically converting water to hydrogen and oxygen, consuming electricity and water. The reaction involved can be summarized as follows[47]:

$$H_2O_{(l)} \rightarrow H_2 + O_2 \quad (20)$$

Where 237.2 KJ/mol energy units have to be supplied in electricity and 48.6 KJ/mol have to be supply in heat. Generally, the categorization of electrolysers is based on the electrolyte type, namely proton exchange membrane electrolyser (PEM), alkaline electrolyser and solid oxide electrolyser (SOEC)[48]. Brief description of different electrolysers categories properties follows. PEM electrolysers are constituted by two electrodes (cathode and anode) and an electrolyte. No separation units are necessary because production of oxygen and hydrogen are produced at different electrodes, according to the following reactions:

$$Anode\ H_2O \rightarrow 2H^+ + 0.5O_2 + 2e^- \quad (21)$$

$$Cathode\ 2H^+ + 2e^- \rightarrow H_2 \quad (22)$$

Notable disadvantages lie in the materials requirement to operate under acidic condition and high voltage. Huge capital costs are necessary for noble metal catalysts. Among advantages, compact design, no leaking issues, high working pressure aptitude, decreased Ohmic loss and highest rate of current density are currently listed[48], [49]. Worthy of notice is absence of deterioration of PEM electrolysers when part-loading operation condition are employed. Alkaline electrolyser has aqueous 30% KOH or NaOH liquid electrolyte. Water is fed to the cathode, and the reaction can be shown as follows:

$$Anode\ 4OH^- \rightarrow O_2 + 2H_2O + 4e^- \quad (23)$$

$$Cathode\ 2H_2O + 2e^- \rightarrow H_2 + 2OH^- \quad (24)$$

Alkaline electrolysers suffers leaking problems, high Ohmic loss and deterioration under part-load performances, but they have lowest capital cost when compared to all other electrolyser types[48]. Lastly, Solid oxide electrolyser cells (SOEC) are the newest kind. Water is fed to the cathode and the reaction can be summarized as it follows:

$$Cathode\ H_2O + 2e^- \rightarrow H_2 + O^{2-} \quad (25)$$

$$Anode\ O^{2-} \rightarrow 0.5O_2 + 2e^- \quad (26)$$

One key factor to highlight is higher temperature conduction (900-950°C)[48]. Most important drawback of SOEC is long term degradation[50], high capital cost due to thermal requirements, and source for thermal energy requirement. Due to high temperature, though, electrical energy necessary for electrolysis process is reduced. Creating electrical energy is more expensive than creating heat energy. As a result, increasing the temperature of the cell might lower the amount of electrical energy required and instead use more thermal energy to perform the electrolysis process, lowering the cost of produced hydrogen[51].

1.3.2 Renewable Sources

Hereafter will be listed most relevant technologies to produce electricity from renewable sources to feed electrolyser and produce green hydrogen.

- Solar

The solar energy source can be categorized into solar thermal, solar photovoltaic and photo electrochemical classes.

- Wind

The wind turns turbines, converting kinetic energy into mechanical energy, which is then converted into electrical energy by a generator.

- Geothermal

Geothermal energy is described as heat generated under the earth's surface. Steam or hot water is used to transport geothermal energy to the earth's surface.

1.4 Separation processes

The utilization of hydrogen can be broadly categorized into the subsequent domains: (1.) As a reactant in hydrogenation procedures, hydrogen is employed to generate compounds with a lower molecular weight. Additionally, it is utilized to saturate compounds, crack hydrocarbons, and eliminate sulphur and nitrogen compounds; (2). As an oxygen scavenger, hydrogen is employed to chemically eliminate minute quantities of oxygen. This serves the purpose of preventing oxidation and corrosion. (3.) As a propellant in rocket engines. (4.) As a coolant in electrical generators, hydrogen is implemented to exploit its distinctive physical properties[52]. The first domain represents the major sector of hydrogen utilization, with almost 50% employment for ammonia production, about 37% for petroleum processing and 8% for methanol [53]. In the majority of these applications, the reaction depends on hydrogen partial pressure, and as a result, the process necessitates the utilization of elevated purities and pressures.

Process viewpoints (e.g., primary purification requirements, feed composition, feed pressure, product flow rate, purity, and by-product recovery) and project considerations (e.g., process flexibility, feed turndown ratio, reliability, and ease of future development) influence the choice of hydrogen separation technologies (in terms of its generation costs)[54]. In oil and gas industry, main hydrogen purification processes are pressure swing adsorption, cryogenic distillation and

permeation. Next paragraph will review methods for hydrogen purification to highlight advantages and disadvantages present for purification of hydrogen from a hot gas mixture.

1.4.1 Pressure Swing Adsorption (PSA)

This purification method is based on the different adsorption properties of adsorber at high and low pressure. Gasses are, in fact, selectively adsorbed at high pressure and desorbed at low pressure. The adsorbent bed depends on the process gasses involved. For CO and CH_4 adsorption, in previous patent reviews, the most popular adsorbent is Type X zeolite, that belongs to the family of aluminosilicate molecular sieves with a faujasite-type structure (FAU). It is characterized by the formula $|(Ca, Mg, Na_2)_{29}\ (H_2O)_{240}|[Al_{58}Si_{134}O_{384}]$– FAU (International zeolite association (IZA))[55]. Usually Type X zeolite are exchanged with Ba, Sr, Ca, Li, and also mixture like Ca/Sr and Ba/Sr[56]. For what concerns N_2 adsorption, in patent reviews, Type X zeolites exchanged with Ca^{2+}, Sr^{2+}, Ag^{+} are preferred. Type A zeolites exchanged with Ca^{2+}, Mg^{2+} and Ag^{+} are also reported[56].

PSA process involves rotating pressure between high-pressure feed and low-pressure tail gas, using a high-purity purge stream of hydrogen. With this procedure small hydrogen adsorption ensures high purity and is achieved with cyclic regime. Typically, 4-12 adsorbed bed are used in industrial units to offer constant flow rates of feed, products and tail gas[57], [58]. Hydrogen purification *via* PSA relies on adsorbent capacity to sequester impurities at high gas-phase partial pressure to later be desorbed at lower partial pressure. To lower partial pressure a “swing” of pressure from feed (optimum of absolute pressure 14-27.5 bar)pressure to tail gas (optimum of absolute pressure 0.138-0.345 bar) is used, employing high-purity hydrogen purge[59]. Advantages are briefly reported here after:

- Cost reduction (5-7%) in feed and fuel, resulting in cost reduction of produced hydrogen.
- Simplicity, reliability flexibility and reduced maintenance required.
- High purity range of hydrogen (99-99.999 vol%), removal to 0.1-10 ppm level of CO and CO_2[59].
- Less capital cost for small hydrogen plants; slightly increased operating costs for larger plants (> 3 million standard $ft^3\ day^{-1}$)
- Avoid hydrogen compression costs[60].

Main disadvantages are low recovery and the viability of operating at 20-30 bar of gaseous feed pressure. Hydrogen recovery achievable by PSA units are moderate, 80-92% at optimum conditions, but 60-80% when tail gas is delivered at higher pressure (2.75-5.51 bar). PSA affordability strongly depends on the ability to use tail gas at low pressure. If tail gas has to be compressed to the refinery fuel gas system pressure, compression equipment costs reach costs of PSA unit[54].

1.4.2 Cryogenic distillation

Cryogenic distillation process happens at temperatures between -153° and 0°C. Relative volatilities at low temperatures are exploited for separation of gaseous compounds. Hydrogen relative volatility is much higher when confronted with hydrocarbons one. Simplest and most conventional separation method for hydrogen is partial condensation of impurities by cooling exits products of steam reforming[54]. Hydrogen purity requirements dictates the preferrable choice of separation

process between PSA and cryogenic distillation[58]. Most relevant positive aspect of cryogenic distillation is low initial investment and energy consumption coupled with high recovery for gaseous currents. Two methods are available:

- Cryogenic Process without Distillation

Offers high recovery, high pressure in operation, contained operating costs and finally low pressure drop of light products. Disadvantage lies on the limit of purity achievable, which is up to 98%[54].

- Cryogenic Process with Distillation

With distillation of light products higher purity is available (up 99.5% hydrogen purity) while still maintaining same positive aspect, except for economical aspect, due to increase of costs and energy consumption[54].

1.5 Hydrogen separation membrane technology

1.5.1 Membrane separation technology

One necessary consideration about current industrial separation method concerning practical factors, is that technology previously listed, due to high capital and operational costs, are viable for medium and large-scale plants and/or continuous operations. Advanced membrane technology, on the other hand, could allow recovery from low purity or low-pressure hydrogen containing streams that would be uneconomical otherwise *via* PSA or cryogenic technologies[1], [61]. Hydrogen separation market could potentially benefit the following membranes technologies benefits: increased energy efficiency, operation simplification, affordability for smaller units, compactness and portability[62], [63]. IUPAC definition states that a membrane is a structure with substantially larger lateral dimensions than thickness, through which transfer can occur under a range of driving pressures[64]. In addition, it can be said that a membrane can act as a selective barrier which implies that only some components of a mixture can pass through while others are blocked. Some interesting concepts arise from recent literature regarding membrane technologies. Coupling reactor with membrane separation, thus intensifying hydrogen production processes, has been progressively recognised as a promising tactic to ensure diversification in clean hydrogen production processes[65]–[73]. Moreover, process intensification can cut costs while increasing the quality of blue hydrogen production[74] and implementing carbon capture technology constitutes new hydrogen production processes for clean hydrogen from conventional fuels[65], [74].

1.5.2 Membrane classification

Following paragraph present classification and brief description of pros and cons of different categories of membranes. Membrane for gas separation constitute a wide variety of materials, and literature proposed classification is based on two major categories centred on structural property: porous membrane and non-porous (dense) membrane[75].

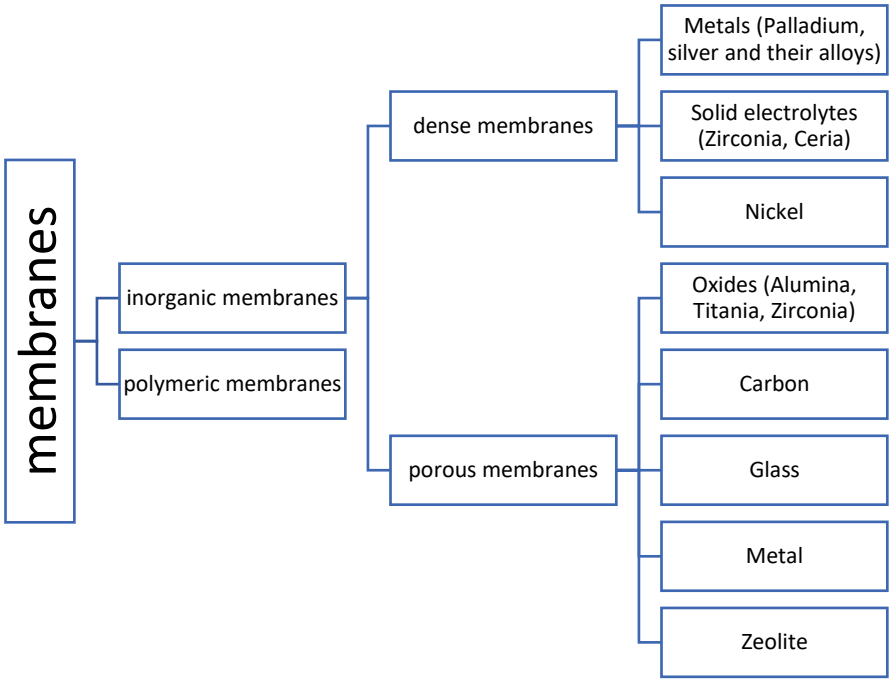

Figure 6 classification of gas separating membrane (adp.)[75], [76]

As stated, a brief list of main different membrane technologies will follow, starting from polymeric membranes.

1.5.3 Polymeric membranes

Polymerics membranes can show separation selectivity for H_2 or CO_2. Commonly, selectivity is achieved through size variation, and H_2-selective membranes are generally fabricated using glassy polymers[77]. Separation process is based on solution-diffusion model, postulated by Thomas Graham[78], in which a potential gradient between upstream and downstream is created across the membrane and the permeability of a determined specie (e.g. H_2) is defined as[79]:

$$J_i = \frac{k(p_2 - p_1)}{l} \qquad (27)$$

Where p_1 and p_2 are partial pressure respectively in downstream and upstream, and l is membrane thickness and k is the Darcy's law coefficient. Important considerations have to be taken into account when performances are represented in terms of selectivity versus permeability (Robeson's upper bound). From available data, there a clear indication that majority of existing polymeric membranes do not reach good enough characteristics to justify a trade-off between selectivity and permeability[80]. In addition, recompression of separated hydrogen may defeat the cost-saving advantage when compared to traditional PSA or cryogenic distillation.

1.5.4 Inorganic porous membranes

In this category, main components are Silica-based membranes, Zeolite-based membranes and Carbon molecular sieves. The transport mechanism in inorganic porous membranes is mainly related to pore radius, permeating gas molecule radius, interaction pore-wall molecules, and pressure difference between upstream and downstream[81]–[83]. Practically, macropores (d_p > 50

nm) allow viscous flow, mesopores (2 nm < d_p < 50 nm) indicate Knudsen regime and surface and/or activated gaseous diffusion are contributors in presence of micropores (d_p < 2 nm). In porous membranes Poiseuille flow or Knudsen diffusion dominates the gas transport. Ratio between mean free path (λ) and pore radius (r) determines which transport dominates[77]. Mean free path is calculated as follows:

$$\lambda = \frac{3\eta}{2P}\left(\frac{\pi RT}{2M}\right) \quad (28)$$

Where η is gas viscosity, P and T are pressure and temperature respectively, M is molecular weight and R is universal gas constant. When r/λ >> 1 Poiseuille flow is major transport phenomena and gas-gas collision are more frequent the gas-pore wall collisions, while when r/λ << 1 Knudsen diffusion is major transport phenomena and gas-pore wall collisions are more frequent than gas-gas collisions. Lastly molecular sieving implies that only smaller molecules can permeate through membranes. Figure 7 show a schematic representation of beforementioned transport mechanisms.

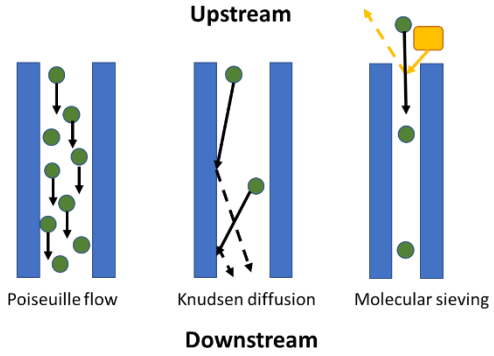

Figure 7 Schematic representation of major gas transport mechanism in porous inorganic membranes(adp)[77]

- Silica Porous Membranes

SiO_4 tetrahedrons sharing corners make up microporous amorphous silica membranes with covalent bonds to form a continuous infinite three-dimensional (3D) network with controlled pore diameters of about 0.5 nm. Typically produced as thin film deposited on support for mechanical stability, they show easy and scalable synthesis methods characterized by low cost, attracting interest in hydrogen separation sector[84], [85]. Usually, silica-based membranes involve of different layer: 1) active for selectivity, 2) intermediate and 3) support layer for mechanical stability. One key aspect to consider when evaluating silica-based membrane is the non-100% selectivity for a particular component[84]. Nevertheless, the main drawback of silica membranes is linked to chemical and structural instability when exposed to humidity, which represent a large problem due to constant presence of steam in industrial hydrogen production processes, potentially limiting their application[85]–[87].

- Zeolite

AlO_4^{5-} and SiO_4^{4-} tetrahedra sharing oxygen edge atoms constitute 3D, crystalline and hydrated microporous alumino-silicate material known as Zeolites. Due to formal negative charge of the framework, mobile alkali or alkali-earth cations occupy position in well-defined cavities, typical characteristic of this class of materials. Dimensions of cavities are typically in molecular range (0.3 -

0.1 nm[88]). Published separation performance data are in major part capable of surpassing beforementioned Robeson's upper bound of trade-off between selectivity and permeation[89]. Despite literature supposed successful development[89], only one application was developed up to industrial scale[88]. The reason for this lack of Zeolite presence in membrane technology has to be found in the difficult production of defect free and thin membrane for practical gas-separation application[77].

- Carbon molecular sieve membranes

Carbon molecular sieve membranes are produced by pyrolysis of a polymeric precursor, and synthesis condition allow tuning pore size distribution[89]. Some advantages worth reporting are thermal and chemical resistance, pore size distribution, high selectivity and permeability towards selected gasses (H_2, O_2, N_2). For what concerns Robeson upper bound, results are well above[76]. Identified drawbacks of carbon molecular sieve membranes are related to mechanical characteristics, such as brittleness and fragility, and to reproducibility and production costs[90]. Also, some stability complications arise when humidity and O_2 are present in streams. Due to chemical reactions, open total porosity may reduce, forming cluster that may block the membrane[91].

The handling and manufacture of carbon and zeolite membranes on a wide scale are also challenging due to their inherent fragility. As a result, before commercialisation is practical, more technological advances in the production and processing of carbon and zeolite membranes are required[77]. Amorphous silica membranes are the easiest and least expensive porous membranes to make, but because they are unstable in the presence of moisture, which is inevitable in hydrogen separations, they must be functionalized with precursors or doped with transition metals. Zeolite, zeotype, and CMSMs are promising candidates for hydrogen separation because their pore size distribution and gas-solid interactions can be tailored by controlling the synthesis conditions and functionalization. Their permeability-selectivity plots frequently exceed the well-known Robeson upper boundary. Composite CMSMs, in particular metal-CMSM, have been created to enhance selectivity and reduce or eliminate several limitations such brittleness, fragility, and synthesis repeatability. However, no industrial-scale uses exist at this time[89].

1.5.5 Dense metallic membrane

The comprehensive classification of dense membrane falls under various material-based technologies, which are elaborated in the ensuing paragraph, as depicted in Figure 6.

The ability to acquire hydrogen through a solitary process has led to a heightened interest in dense metallic and metallic alloy. Palladium-based materials are commonly favoured due to their capacity for selective permeation of hydrogen and catalytic efficiency of the surface. Owing to these advantageous properties, palladium-based materials have become increasingly popular for a variety of applications [92]. This work provides a concise overview of the transport of hydrogen, beginning with a description of the permeation mechanism as characterized by the Ward and Dao model [93] . According to this model, hydrogen transport occurs through a solution-diffusion mechanism that involves a series of distinct steps. These steps include the transport of hydrogen from bulk gas to the surface, followed by surface dissociative adsorption of hydrogen, the progression of atomic

hydrogen (H) from metal surface to metal bulk, bulk diffusion, the progression of atomic hydrogen (H) from metal bulk to metal surface, and finally, recombinative molecular desorption of hydrogen, which ultimately results in transport from metal surface to gas bulk. To describe the permeation of hydrogen, a semi-empirical expression is employed (Eq. 29), which provides a quantitative model for understanding the transport of hydrogen through various materials. This model is of great interest to researchers and engineers alike, as it has important implications for the development of new technologies and materials that can be used to effectively store and transport hydrogen.

$$J_{H_2} = \frac{P_{m,H_2}(p_{H_2,ret}^n - p_{H_2,perm}^n)}{\delta} \quad (29)$$

Where J_{H_2} (mol m^{-1} s^{-1}) is hydrogen flow through the membrane, P_{m,H_2} (mol m^{-1}s^{-1}Pa^n) stands for the permeability, δ (m) for the thickness, $p_{H_2}^n$ (Pa) is the partial pressure of hydrogen. The exponent (*n*) ranges from 0.5 to 1, depending on the limiting step of the hydrogen permeation mechanism. When *n* value is 0.5 Eq.(28) becomes Sievert's Law[94]. Vanadium, Niobium, and Tantalum would all have higher hydrogen permeability of several order than Palladium. These metal, though, undergo prompt oxidation, hindering transport properties and need catalytic layer to ensure surface dissociation kinetics while palladium readily dissociates hydrogen and is resistant to oxidation, and thus is considered very attractive for hydrogen separation[84], [95]. It is noteworthy that some limitations with the use of palladium are linked with typical gas stream impurities (hydrogen sulfide, ammonia, mercury, carbon dioxide, carbon monoxide *etc.*) leading to Palladium surface poisoning[96]. However, as a result of the recurrent shifting between phases during heat cycling, irreversible changes in the Pd lattice structure might occur, resulting in membrane breakdown. Furthermore, the excessive cost of palladium limits their use in large-scale H_2 synthesis. In order to reduced Pd usage, further research to improve this technology, ensuring cost-effectiveness and sustainability is necessary[97], [98]. Other metals that show certain attractiveness are Nickel and Vanadium[99]–[103].

1.6 Dense mixed ionic electronic conductive ceramic membranes

In the context of hydrogen separation with membranes, mixed Proton-Electron Conductor (MPEC) represent promising alternative for low-cost hydrogen purification with virtually 100% selectivity and high chemical and thermal stability [3]. As the other membranes, MPEC membranes extract hydrogen from hydrogen enriched streams thanks to a driving force achieved thanks to the difference in hydrogen partial pressure. To perform the hydrogen separation, MPEC membranes employ ambipolar diffusion of both proton and electrons in the same direction to keep electroneutrality, without the use of an external circuit. This process is schematized in Figure 8.

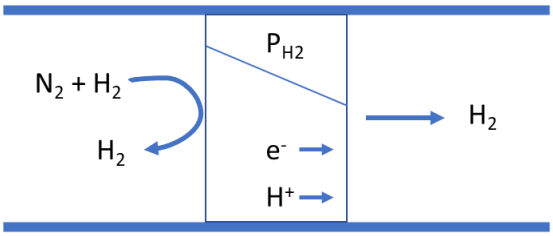

Figure 8 Schematic representation of hydrogen permeation in a MPEC membrane using N_2 mixture as an example(adp.)[104].

1.6.1 Perovskite structure

For reasons linked to the hydrogen transport mechanism that will be presented in the next paragraph, the most popular material and structure is the perovskite structure with ABO_3 chemical formula.

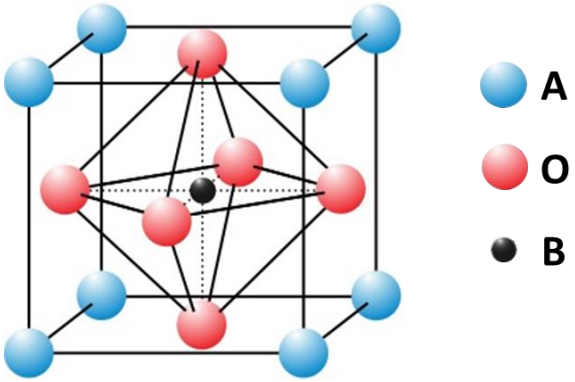

Figure 9 ABO_3 perovskite structure(adp.)[105].

In Figure 9 it is possible to see a schematic representation of the perovskite structure, where B represent a transition metal cation element (Mn, Cr, Fe etc) or a rare earth element (Ce or Zr) that has a high positive valence and occupies the centre of the perovskite structure by constructing a six-coordinate octahedron with neighbouring oxygen ions (represented by O). The large A-site cation occupies the centre of the cavity between 8 octahedra (BO_6)[106]. A-site cation can be lanthanides (e.g., La, Pr, and Gd) or alkaline earth metals (e.g., Ba and Sr). Doping a trivalent element into the structure affects the distance between the oxygen ions, resulting in dramatic variations in the structure's proton conductivity[107]. Doping a trivalent element (M), the chemical formula of these high-temperature, proton-conducting perovskite oxides can be seen as $AB_{1-x}M_xO_3$. The effect of trivalent cation M doping into the B site can increase the vibration distance between the oxygen ions and also increase the amount of oxygen vacancies, leading to higher proton conductivity[108]–[110].

1.6.2 Hydrogen transport mechanism

The presence of substantial amount of oxygen vacancies enables the mixed protonic-electronic conductivity forming considerable number of protons within the perovskite lattice. These protons come from gas source as either water vapor or hydrogen gas. In a dry atmosphere proton intake into lattice happens by formation of interstitial proton (Eq. 30) by interaction between hydrogen and lattice oxygen electronic cloud[111].

$$H_2 + O_O^X + 2h^\bullet \rightleftarrows 2OH_O^\bullet \quad (30)$$

In a humidified source a surface oxygen vacancy act as water dissociation site for water, into hydroxide ion and a proton. The oxygen vacancy is filled by the new-formed hydroxide ion while the proton is become lattice interstitial hydrogen attaching to a neighbouring lattice oxygen[112] (Eq. 31).

$$H_2O + V_O^{\bullet\bullet} + O_O^X \rightleftarrows 2OH_O^\bullet \quad (31)$$

Where $V_O^{\cdot\cdot}$ stands for oxygen vacancy with +2 oxidation state, O_O^X is a lattice oxygen, $2h^{\cdot}$ is an electron hole and $OH_O^{\cdot}$ is a hydroxyl ion that can be seen as an interstitial proton that is attached to the lattice oxygen. In both cases protons never occupy lattice position but are present as $OH_O^{\cdot}$ species, bonded to lattice oxygen. The relation between hydration, electronic conductivity and oxygen vacancies can be better understood by observing the equilibrium reactions between oxygen vacancies and oxygen partial pressure, that follow:

$$O_O^X \rightleftarrows \frac{1}{2}O_2(g) + V_O^{\bullet\bullet} + 2e^{\bullet} \quad (32)$$

$$V_O^{\bullet\bullet} + \frac{1}{2}O_2(g) \rightleftarrows O_O^X + 2h^{\bullet} \quad (33)$$

Depleted oxygen partial pressure ensures Eq. 32 relevance, producing an oxygen vacancy coupled with 2 electrons. Eq. 33 results more prevalent when higher oxygen partial pressure is present and oxygen dissolves in the lattice[113]. The electron is the charge carrier in the first scenario, whereas the electron hole is the charge carrier in the second scenario[113]. The charged defects move in specific directions under the electrochemical gradient when the mixed proton conducting membrane is exposed to gaseous hydrogen on one side and to oxygen on the other side at high temperatures (i.e., asymmetrical gas environment), as indicated in Figure 10.

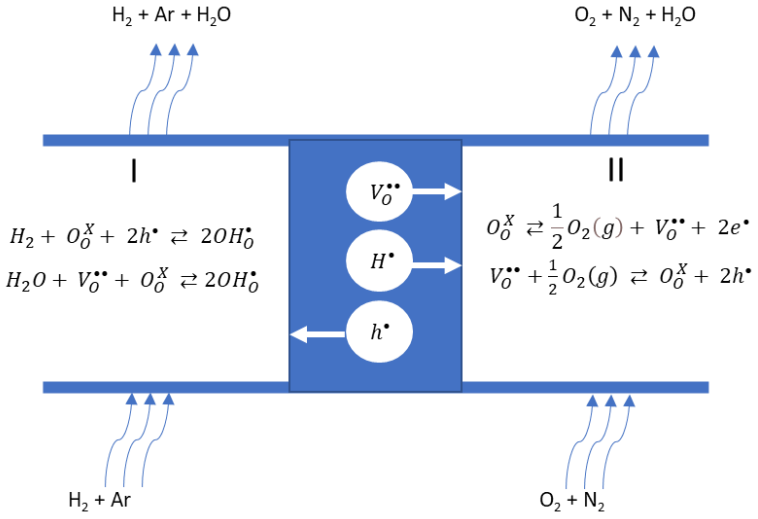

Figure 10 Transport diagram of ion permeation in mixed protonic electronic conducting membrane(adp.)[114]. $P_{H2}^{I} > P_{H2}^{II}$

As stated, the proton travelling across the membrane has to be considered residing on an oxygen ion in the lattice. The predominating transport mechanism for such proton is called "Grotthus mechanism" and provide free proton jump. The proton conduction happens by "hopping" between adjacent oxygen ions, namely the proton creates a weak O-H bond with one oxygen ion after adhering to the ceramic surface; this bound proton then spins and hops, creating a second weak O-H bond with the new neighbouring oxygen ion. Repeating this procedure until proton conduction is complete[115]. A schematic representation is reported in Figure 11.

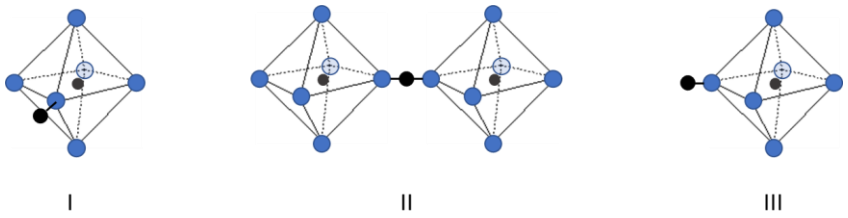

Figure 11 diagram of the Grotthuss mechanism for proton conduction in ceramic material(adp.)[115].

This mechanism is generally accepted to explain proton conductivity in MPEC[113]. In this instance, the distance between oxygen ions in the ceramic material's crystal lattice should have a substantial influence in proton conductivity—that is, as the vibration distance between the oxygen ions grows, so would the proton conductivity. This was discovered when the activation energy for proton conductivity was measured as a function of oxygen ion distance[116]. The amount of the oxygen ion distance in a crystal structure is significantly dependent on the materials and crystal structures involved. The most common material and structure for H_2 separation membranes, for example, is ABO_3 perovskite structure (see Perovskite structure). Doped $BaCeO_3$, $BaZrO_3$, $SrCeO_3$, and $SrZrO_3$ are the best perovskite candidates for high proton conductivities. Among these, the $BaCeO_3$-based oxides have the highest proton conductivity (i.e., ~102 S cm^{-1} at 700 °C). Nonetheless, in CO_2 and/or humid environments, they easily breakdown into barium carbonate and/or barium hydroxide[117]. Doping with cations with higher ionic radius than Ce increased proton conductivity (compared to the non-doped compound). Doping with more electronegative dopants improves structural stability[118]. Doped compounds with the formula $BaCe_{1-x}A_xO_{3-\delta}$ (A = Y^{3+}, In^{3+}, rare-earth such as Nd^{3+}, Sm^{3+}, Gd^{3+}, Eu^{3+}, Yb^{3+}) exhibit high proton conductivity[119]–[125]. As previously stated, protonic defects in perovskite due to dissociative adsorption of water in the presence of oxygen vacancies is primarily responsible for the rise in proton conductivity thanks to the doping[126]. In the instance of Y-doped $BaCeO_3$, the defect reaction results in the formation of oxygen vacancies, which may be represented in Kroger-Vink notation as:

$$2Ce_{Ce}^{X} + Y_2O_3 + O_O^X \rightarrow 2Y'_{Ce} + V_O^{\bullet\bullet} + 2CeO_2 \qquad (34)$$

Where Ce_{Ce}^{X} and O_O^X are lattice cerium ion and oxygen ion respectively. Y'_{Ce} stand for yttrium ion occupied at cerium ion site[126]. So far, in order to avoid decomposition of barium cerate in CO_2 and H_2O containing atmosphere as barium carbonate and cerium oxide at high temperature[127], [128], a popular approach is to prepare mixed barium cerate/barium zirconate solid solution. $BaZrO_3$ has much lower conductivity but is more chemically stable at elevated temperatures in CO_2 and humid atmospheres. Thanks to the possibility to form solid solution across wide composition range, a good balance between conductivity and chemical stability is achievable[129].

1.6.3 Mathematical models for Hydrogen Permeation

The circumstances or processes that exist at the membrane's opposing surfaces control the proton and electron conductions across it. The driving force for hydrogen separation is a concentration gradient, which is modelled by a Nernstian potential difference as follows:

$$E = -\frac{RT}{nF}\ln\left(\frac{P_{H_2}^{II}}{P_{H_2}^{I}}\right) \qquad (35)$$

Where R is the universal constant, T is the temperature, n is the electron number in the hydrogen association/dissociation reaction (i.e., equal to 2), F is the Faraday constant, $P_{H_2}^{II}$ is hydrogen partial pressure at the permeate side, $P_{H_2}^{I}$ is hydrogen partial pressure at the retentate side. By using the definition of total conductivity, $\sigma_{tot} = \sum_k \sigma_k$ and transport number $t_k = \sigma_k / \sigma_{tot}$ the mathematical model for proton flow can be expressed with the Wagner equation[81], [104], [130]:

$$J_{H_2} = \frac{1}{4L} \frac{RT}{F^2} \int_{P_{H_2}^{I}}^{P_{H_2}^{II}} \sigma_{tot} t_{H^+} (t_e + t_h) d\ln P_{H_2} \quad (36)$$

Where L is the thickness of the membrane. Eq. 36 is valid assuming negligible oxygen ion transport number, hydrogen dissociation rate at the surface of the membranes much higher than bulk diffusivity of charge carriers, negligible mass transfer.

1.7 Current Status

Research in the field of ceramic membrane for hydrogen separation are mainly oriented towards the improvement of hydrogen permeation, in order to reach 1 mL min^{-1} cm^{-2}, an arbitrary value selected during project drafting, that has been considered as an interesting goal for implementation in industrial applications, and membrane stability. Research effort can be dividend in a five-element array, namely single-phase perovskite, dual-phase perovskite, asymmetric structure, surface modification and hollow-fiber shaped membranes. To make data evaluation easier, hollow fiber shape has been considered a standalone category, due to less frequent papers with this shape, while disk shape is shared for all the other categories.

1.7.1 Single phase perovskite

$SrCeO_3$ and $BaCeO_3$ material have been studied thanks to the high protonic conductivity in hydrogen containing atmosphere. $BaCeO_3$-based perovskite oxide have been reported to show comparable oxygen ion and proton conductivity[131], limiting the application to oxygen free atmosphere. The majority of the membrane is composed of alkaline-earth metal-containing perovskite-type oxides, which are prone to composition instability due to CO_2 presence, due to the interaction of CO_2 with alkaline-earth ions (Ba^{2+}, Sr^{2+})[132]–[134]. For this reason, lanthanum tungstate oxide have been studied. The following table contains permeation performances of several single-phase disk-shaped membranes.

composition	J_{H2} (mL min^{-1} cm^{-2})	Feed/sweep atmospheres	T (°C)	thickness (cm)	shape	ref
$BaCe_{0.80}Y_{0.20}O_{3-d}$	0,01	50% H_2 + 50% He/N_2	950	1	Disk	[135]
$BaCe_{0.95}Nd_{0.05}O_{3-d}$	0,017	Dry 80% H_2 + 20% He/Dry 98%Ar + 2% Ne	925	0,7	Disk	[136]
$BaCe_{0.95}Nd_{0.05}O_{3-d}$	0,026	80%H_2 + 15%H2O+ 5%He/Dry 98%Ar + 2% Ne	925	0,7	Disk	[136]
$BaZr_{0.90}Fe_{0.10}O_{3-d}$	0,75	20% H_2 + 80% He/Ar	900	1,15	Disk	[137]
$BaZr_{0.80}Y_{0.15}Mn_{0.05}O_{3-d}$	0,03	Wet 50% H_2 + 50% He/Wet Ar	1000	0,9	Disk	[138]
$SrCe_{0.95}Eu_{0.05}O_{3-d}$	4,28 10^(-3)	Dry 100% H_2/He	850	1,72	Disk	[139]
$SrCe_{0.95}Eu_{0.05}O_{3-d}$	3,88 10^(-3)	Wet 100% H_2/He	850	1,72	Disk	[139]
$SrCe_{0.95}Sm_{0.05}O_{3-d}$	3,13 10^(-3)	Dry 100% H_2/He	850	1,72	Disk	[139]
$SrCe_{0.95}Sm_{0.05}O_{3-d}$	1,62 10^(-3)	Wet 100% H_2/He	850	1,72	Disk	[139]
$SrCe_{0.95}Tb_{0.05}O_{3-d}$	1,4 10^(-2)	20%H_2 + 80%He/0.001 atm CO+ Ar	900	1	Disk	[140]
$SrCe_{0.95}Tb_{0.05}O_{3-d}$	1,6 10^(-2)	20% H_2 + 80% He/0.1 atm CO + Ar	900	1	Disk	[140]
$SrCe_{0.95}Tm_{0.05}O_{3-d}$	0,04	10% H_2 + 90% He/Air	900	1,6	Disk	[141]
$SrCe_{0.95}Tm_{0.05}O_{3-d}$	4,25 10^(-2)	10% H_2 + 90% N_2/20% O_2 + 80% Ar	900	1,6	Disk	[142]
$SrCe_{0.95}Tm_{0.05}O_{3-d}$	9,54 10^(-3)	25% H_2 + 75% Ar/Ar	900	0,7	Disk	[143]
$SrCe_{0.95}Tm_{0.05}O_{3-d}$	0,022	H_2/Ar	900	0,7	disk	[143]
$SrCe_{0.95}Yb_{0.05}O_{3-d}$	9,14 10^(-3)	25% H_2 + 75% Ar/Ar	900	0,7	disk	[143]
$SrCe_{0.95}Yb_{0.05}O_{3-d}$	0,019	H_2/Ar	900	0,7	disk	[143]
$SrCe_{0.95}Zr_{0.10}Tm_{0.05}O_{3-d}$	1,50 10^(-2)	10% H_2 + 90% N_2/20% O_2 + 80% Ar	900	1,6	disk	[142]
$SrCe_{0.75}Zr_{0.2T}m0_{.05O}3$-d	0,042	40% H_2 + 60% He/Ar	900	1,2	disk	[144]
$SrCe_{0.95}Tm_{0.05}O_{3-d}$	0,054	50% H_2 + 50% He/Ar	900	1,2	disk	[145]
$SrCe_{0.85}In_{0.1}Tm_{0.05}O_{3-d}$	0,042	50% H_2 + 50% He/Ar	900	1,2	disk	[145]
$SrCe_{0.75}In_{0.2}Tm_{0.05}O_{3-d}$	0,033	50% H_2 + 50% He/Ar	900	1,2	disk	[145]
$La_{5.5}WO_{11.25-\delta}$	0,13	50% H_2/He, Ar	1000	0,09	disk	[146]
$La_{27}Mo_{1.5}W_{3.5}O_{55.5}$ (LWMo)	0,096	97% H_2/He, Ar	1026	0,13	disk	[147]
$La_{5.5}W_{0.45}Nb_{0.15}Mo_{0.4}O_{11.25-\delta}$	0,195	50% H_2/He, Ar	1000	0,5	disk	[148]
$La_{5.5}W_{0.8}Re_{0.2}O_{11.25-d}$	0,095	50% H_2/He, Ar	700	0,076	disk	[149]
$Nd_{5.5}W_{0.5}Mo_{0.5}O_{11.25-d}$	0,084	50% H_2/He, Ar	725	0,09	disk	[150]

Table 1 permeation performances of single-phase disk-shaped membranes

Apart from one single case[137], most of reported literature works show a maximum value of hydrogen permeation around 0.1 mL $min^{-1}cm^{-2}$, which is still far from values that can spark industrial interest . One main topic that can be noticed in few works[137], [140], [142] is the hydrogen permeation limited by the membrane electronic conductivity.

1.7.2 Dual-phase membranes

As explained in paragraph *1.1.6 Dense mixed ionic electronic conductive ceramic membranes*, high protonic and electronic transport is essential to exhibit desirable hydrogen flows. For this reason, an interesting, employed approach is the combination of two different materials, each one with high conductivity (electronic or protonic), producing membranes that are known as dual-phase membranes. Dual phase membranes are typically produced as composite of ceramic and metallic phases (CerMet) or two ceramic phases (named CerCer). For what concerns CerMet composite membrane, can be produced to combine (1) high hydrogen permeable metal with low hydrogen permeable ceramic phase, (2) vice versa, highly hydrogen permeable ceramic phase with low hydrogen permeable and lastly (3) combination of both highly hydrogen permeable ceramic phase and metal[151]. In Table 2 a summary of CerMet membrane is reported.

Materials	H_2 flux (mL cm^{-2} min^{-1})	Feed/sweep atmospheres	Temperature (C)	Thickness (mm)	Shape	Ref.
$Ni\text{-}BaCe_{0.85}Tb_{0.05}Zr_{0.10}O_{3-d}$ (50:50 wt%)	0,17	Dry 50% H_2 + 50% He/Ar	800	0,5	Disk	[152]
$Ni\text{-}BaCe_{0.90}Y_{0.10}O_{3-d}$ (40:60 vol%)	0,76	100%H_2/N_2 + H_2	800	0,23	Disk	[153]
$Ni\text{-}BaZr_{0.10}Ce_{0.70}Y_{0.20}O_{3-d}$ (40:60 vol%)	0,805	100% H_2/He	900	0,266	Disk	[154]
$Ni\text{-}BaZr_{0.10}Ce_{0.70}Y_{0.20}O_{3-d}$ (30:70 vol%)	3,36 x 10^{-2}	40% H_2 + 58.5% N_2 + 1.5% H_2O/Ar	700	0,5	Disk	[155]
$Ni\text{-}BaZr_{0.10}Ce_{0.70}Y_{0.10}$ $Yb_{0.10}O_{3-d}$ (40:60 vol%)	0,118	40% H_2 + 57% He + 3% H_2O/N_2	900	0,56	Disk	[156]
$Ni\text{-}Ba_{0.8}Zr_{0.50}Ce_{0.35}Tb_{0.15}O_{3-d}$ (40:60 vol%)	0,07	16.7% H_2 + 83.3% N_2/Ar	900	1,5	Disk	[157]
$Ni\text{-}BaZr_{0.70}Pr_{0.10}Y_{0.10}O_{3-d}$ (40:60 vol%)	1,62 x 10^{-2}	40% H_2 + 57% N_2 + 3% H_2O/Dry Ar	950	0,4	Disk	[158]
$Pd\text{-}CaZr_{0.90}Y_{0.10}O_{3-d}$ (50:50 vol%)	2,30	80% H_2 + 20% He/Dry N_2	900	0,55	Disk	[159]
$Pd\text{-}BaCe_{0.40}Zr_{0.40}$ $Gd_{0.10}Dy_{0.10}O_{3-d}$ (50:50 vol%)	2,77	100% H_2/Dry N_2	700	0,4	Disk	[160]
$Cu\text{-}BaZr_{0.90}Y_{0.10}O_{3-d}$ (60:40 vol%)	4,6 x 10^{-4}	100% H_2/Dry Ar	882	1,9	Disk	[161]

Table 2 permeation performances of double-phase CerMet membranes

Composite membrane of the first combination usually employ Palladium metal and exhibit highest permeation results[159], [160]. The high cost of palladium though, determines the need to find a viable alternative that is seen in Nickel. Usually, composite Nickel metal containing CerMet membranes are part of the second combination[154], and exhibit permeation performances superior to single phase membrane, thanks to enhanced electronic conductivity. Lastly, it is interesting to highlight also the employment of Copper as metal component, because Cu has been reported to be inert to coking[162]. Lastly, for what concerns the third combination, literature[153], [163] describes modest hydrogen permeation flow due to interfacial features between ceramic phase and metallic phase not accomplishing full potential, limiting ambipolar diffusion. The fundamental disadvantage of CerMet dual-phase membranes is their low thermal compatibility between ceramic and metal phases, as well as the likelihood of metal oxidation during the preparation process[164]. To circumvent these limitations, high electrical conductivity ceramics can be utilised as the second phase instead of metal to construct dual-phase (CerCer) membranes. In a ABO_3 perovskite the electronic conductivity is related the change in valence related to the B-site ion[129], [165]–[168]. A short summary of hydrogen permeation performances of several CerCer membranes is reported in Table 3. Hydrogen permeation performances of CerCer membrane are still inferior if compared with CerMet, for instance $Pd\text{-}CaZr_{0.90}Y_{0.10}O_{3-d}$ [159].

Materials	H_2 flux (mL cm^{-2} min^{-1})	Feed/sweep atmospheres	Temperature (°C)	Thickness (mm)	Note	Ref.
$BaCe_{0.20}Zr_{0.70}Y_{0.10}O_{3-d}$-$Sr_{0.95}Ti_{0.90}Nb_{0.10}O_{3-d}$ (50:50 vol%)	1,07 10^{-2}	Dry 4% H_2 + 96% He/Dry Ar	800	1	Disk	[165]
$BaCe_{0.80}Zr_{0.20}O_{3-d}$ -$Ce_{0.80}Y_{0.20}O_{2-d}$ (50:50 wt%)	7,44 10^{-2}	Wet 50% H_2 + He + Ar/Ar	900	1,44	Disk	[166]
$BaCe_{0.65}Zr_{0.20}Y_{0.15}O_{3-d}$-$Ce_{0.85}Gd_{0.15}O_{2-d}$ (50:50 vol%)	0,27	Wet 50% H_2 + 50% He/Wet Ar	755	0,65	Disk	[129]
$BaCe_{0.65}Zr_{0.20}Y_{0.15}O_{3-d}$-$Ce_{0.85}Gd_{0.15}O_{2-d}$ (60:40 vol%)	0,14	Wet 50% H_2 + 50% He/Wet Ar	755	0,66	Disk	[129]
$BaCe_{0.65}Zr_{0.20}Y_{0.15}O_{3-d}$-$Ce_{0.85}Y_{0.15}O_{2-d}$ (50:50 vol%)	0,12	Wet 50% H_2 + 50% He/Wet Ar	735	0,61	Disk	[129]
$SrCe_{0.95}Y_{0.05}O_{3-d}$-ZnO (90:10 wt%)	3,90 10^{-2}	21% H_2 + 79% He/N_2	900	1,09	Disk	[167]
$La_{5.5}WO_{11.25-d}$-$La_{0.87}Sr_{0.13}CrO_{3-d}$ (50:50 vol%)	0,15	Wet 50% H_2 + 50% He/Wet Ar	700	0,37	Disk	[168]

Table 3 permeation performances of double-phase CerCer membranes

Electrical conductivity studies of materials containing perovskite and similar structures are primarily published in the literature for Al, Ga, In, Sc, Cr, Mn, Fe, Co, Ti, Zr, Nb, Ta, V, Mo, Gd, Y, Zn or W as B-site cations[129], [165], [166], [168]–[175].

1.7.3 Asymmetric membrane

As expressed in Eq. 36, hydrogen permeation increases when the diffusion path is narrowed, thanks to the decrease of membrane thickness. For this reason, the creation of asymmetric structures made of a dense active layer with a thin profile and a thicker, more porous substrate may assist in improving hydrogen permeability and has caught the attention of many research groups[3]. Combining a porous substrate could overcome thickness limitation (linked to the dense active layer) while still producing a mechanical robust membrane. It is generally good practice to employ the same material for both the dense and the porous layer of the membrane to avoid some thermal expansion mismatch phenomena and to choose the proper porosity to ensure reactant supply to the dense active layer. Table 4 present several permeation performances of asymmetric membrane with single and double-phase.

Materials	H_2 flux (mL/cm²/ min)	Feed/sweep atmospheres	Temperature (°C)	Thickness (mm)	Porous layer	Ref.
$SrCe_{0.95}Tm_{0.05}O_{3-d}$	0,125	10% H_2 + 90% He/Air	900	0,15	$SrCe_{0.95}Tm_{0.05}O_{3-d}$	[176]
$SrCe_{0.95}Yb_{0.05}O_{3-d}$	0,013	H_2 + He (or N_2)/N_2 + O_2 + He	677	0,002	$SrZr_{0.95}Y_{0.05}O_{3-d}$	[177]
$Sr(Ce_{0.6}Zr_{0.4})_{0.85}Y_{0.15}O_{3-d}$	1,84 10-4	H_2/Ar	800	0,017	$Sr(Ce_{0.6}Zr_{0.4})_{0.85}Y_{0.15}O_{3-d}$	[178]
$BaCe_{0.90}Y_{0.10}O_{3-d}$	0,113	Dry 10% H_2 + 90% N_2/Ar	800	0,01	ZrO_2	[179]
$BaCe_{0.90}Y_{0.10}O_{3-d}$	0,17	Dry 10% H_2 + 90% N_2/Ar	800	0,01	ZrO_2	[179]
$BaCe_{0.85}Tb_{0.05}Zr_{0.1}O_{3-d}$	0,07	50% H_2 + 50% He/Ar	800	0,05	$BaCe_{0.85}Tb_{0.05}Zr_{0.1}O_{3-d}$	[180]
Ni-$BaCe_{0.95}Tb_{0.05}O_{3-d}$ (50:50 wt%)	0,914	50% H_2 + 50% N_2/He	850	0,09	Ni-$BaCe_{0.95}Tb_{0.05}O_{3-d}$	[181]
Ni-$BaZr_{0.10}Ce_{0.70}Y_{0.20}O_{3-d}$ (55:45 wt%)	0,32	80%H_2 + 17%He + 3%H_2O/Dry Ar	900	0,003	Ni-$BaCe_{0.70}Zr_{0.10}Y_{0.20}O_{3-d}$	[182]
Ni-$BaZr_{0.10}Ce_{0.70}Y_{0.10}Yb_{0.10}O_{3-d}$ (40:60 vol%)	0,49	Dry 100% H_2/He	700	0,044	Ni-$BaZr_{0.10}Ce_{0.70}Y_{0.10}$ $Yb_{0.10}O_{3-d}$	[183]
Ni-$BaZr_{0.10}Ce_{0.70}Y_{0.10}Yb_{0.10}O_{3-d}$ (40:60 vol%)	1,12	Dry 100% H_2/He	900	0,044	Ni-$BaZr_{0.10}Ce_{0.70}Y_{0.10}$ $Yb_{0.10}O_{3-d}$	[183]
$BaCe_{0.65}Zr_{0.20}Y_{0.15}O_{3-d}$-$Ce_{0.85}Gd_{0.15}O_{2-d}$	0,27	Wet 50% H_2 + He/wet Ar	750	0,02	$BaCe_{0.65}Zr_{0.20}Y_{0.15}O_{3-d}$-$Ce_{0.85}Gd_{0.15}O_{2-d}$	[3]

Table 4 permeation performances of asymmetric membranes.

1.7.4 Surface Modified Membrane

A particular approach that can be exploited in ceramic membrane field is to apply some form of surface modification to improve the hydrogen permeation. Two possible tactics are increasing surface area of the membrane through porous layer coating or enhancing surface exchange kinetics by employing a catalytic layer. Due to relevant correlation with this elaborate purpose, literature works reported will be briefly discussed highlighting key findings. A summary of several permeation performances of surface modified membrane is reported in Table 5.

Materials	Feed/sweep atmospheres	Temperature(°C)	Thickness (mm)	J_{H2} (mL cm 2 min 1)	type of catalytic activation	amount of catalyst	Ref.
$La_{0.87}Sr_{0.13}CrO_{3-d}$	10% H_2 + 2.5% H_2O + He/Ar	1000	0,55	10-4	Pt	Pt paste	[184]
$Sr_{0.97}Ce_{0.9}Yb_{0.1}O_{3-d}$	10% H_2 + 90% N_2/Ar	804	1,16	0,044	Pt	porous layer	[185]
Ni-$BaCe_{0.90}Y_{0.10}O_{3-d}$	Dry 4% H_2 + 96% He/H_2 + N_2	900	0,270	0,065	sputtered Pd	30 nm layer	[186]
$BaCe_{0.20}Zr_{0.70}Y_{0.10}O_{3-d}$-$Sr_{0.95}Ti_{0.90}Nb_{0.10}O_{3-d}$	Dry 4% H_2 + 96% He/Dry Ar 100mL/min	800	1	3,49 10-2	sputtered Pd	100 nm layer	[165]
$La_{5.5}WO_{11.25-\delta}$/ $La_{0.87}Sr_{0.13}CrO_{3-\delta}$ (LWO/LSC)	H_2/He 100 mL/min, Ar 150 mL/min both humidified	750	0,45 0,42 0,52 0,50 0,42 0,36	0,046 0,034 0,036 0,086 0,11 0,22	$La_{0.87}Sr_{0.13}CrO_{3-\delta}$ (LSC) $La_{0.75}Ce_{0.1}Sr_{0.15}CrO_{3-\delta}$ (LCeSC) $La0.75Ce_{0.1}Sr_{0.15}Cr_{0.95}Ru_{0.05}O_{3-\delta}$ (LCeSCR) $La_{0.85}Sr_{0.15}Cr_{0.8}Ni_{0.2}O_{3-\delta}$ (LSCN) $La_{0.75}Ce_{0.1}Sr_{0.15}CrO_{3-\delta}$ infiltrated with Ni Pt	20 um porous layer 20 um porous layer 20 um porous layer 20 um porous layer 20 um porous layer - Ni Pt ink	[187]
$La_{5.5}WO_{11.25-\delta}$	50% H_2+He 100 mL/min, Ar 150 mL/min	1000	0,9	0,13	Pt	20 um porous layer	[146]
$La_{27}Mo_{1.5}W_{3.5}O_{55.5}$ (LWMo)	97,2% H_2+He 25 mL/min, Ar 5-15 mL/min	1026	1,3	0,096	Pt	Pt paste	[147]
$La_{5.5}W_{0.8}Re_{0.2}O_{11.25-d}$	50% H_2+He 100 mL/min, Ar 150 mL/min	700	0,76	0,095	Pt	20 um layer (screen printed)	[149]
$BaCe_{0.8}Eu_{0.2}O_{3-\delta}$-$Ce_{0.8}Y_{0.2}O_{2-\delta}$	50% H_2+He 100 mL/min, Ar 150 mL/min	700	0,5	0,4	Pt	20 um layer	[188]
$Nd_{5.5}W_{0.5}Mo_{0.5}O_{11.25-d}$	50% H_2+He 100 mL/min, Ar 150 mL/min	725	0,9	0,084	Pt	20 um Pt layer (screen printed)	[150]
$BaCe_{0.65}Zr_{0.20}Y_{0.15}O_{3-d}$ - $Ce_{0.8}Gd_{0.2}O_{2-d}$	50% H_2+He 100 mL/min, Ar 150 mL/min	750	0,02 dense, 0,75 thick	0,47	Pt	20 um Pt layer (screen printed), PtNPs infiltration	[189]
$La_{5.5}WO_{11.25-\delta}$-$La_{0.87}Sr_{0.13}CrO_{3-\delta}$	50% H_2+He 100 mL/min, Ar 150 mL/min	750	0,36	Pt 0,22 Cu 0,15 Cu-Pd 0,15	10 um Pt (screen printed) Cu sputtered Pd-Cu sputtered	1.61 × 10−2 (Pt) Cu 1.21 × 10−3 (Cu) 1.21 × 10−3 (Cu) 8.00 × 10−5 (Pd)	[190]
$La_{5.5}WO_{11.25-d}$-$La_{0.87}Sr_{0.13}CrO_{3-d}$	50% H_2+He 100 mL/min, Ar 150 mL/min	700	0,37	0,15	Pt	20 um porous Pt	[168]
$BaCe_{0.65}Zr_{0.20}Y_{0.15}O_{3-d}$- $Ce_{0.85}Gd_{0.15}O_{2-d}$	50% H_2+He 100 mL/min, Ar 150 mL/min	700	1	0,27	Pt	20 um porous Pt	[129]

Table 5 Summary of permeation performance of surface modified membranes.

In Vigen *et al.*[184]. work, employing a Pt-coating significantly affected the permeation performance of a $La_{0.87}Sr_{0.13}CrO_{3-\delta}$ membrane in both dry and wet environment, indicating that surface kinetics may limits the overall flux. Pt coating was reported to increase both hydrogen surface exchange rate and hydrogen flux, further reinforcing the conclusion that surface kinetics limit hydrogen permeability. Similar finding was demonstrated by Mather *et al.*[185], which established the relevance of the catalytic layer, implying that interfacial mechanisms govern the rate of hydrogen penetration, at least to some extent. It is worth noticing that membrane performances were altered due to restructuring of Pt catalyst at high temperature [185]; this might led to further consideration addressed to the morphology of the Pt catalyst in order to improve permeation performances of ceramic membranes. A similar conclusion was drawn by Zhang *et al.*[186] who experienced a less dramatic increase of hydrogen permeation at high temperature, linked the sputtered Pd catalyst microstructural evolution at high temperature and the interfacial polarization resistance. Apart from employing pure metallic layer, Escolàstico *et al.*[187] determined effect of different ceramic porous catalytic layer on membrane hydrogen permeation: $La_{0.87}Sr_{0.13}CrO_{3-\delta}$ (LSC), $La_{0.75}Ce_{0.10}Sr_{0.15}CrO_{3-\delta}$ (LCeSC), $La_{0.75}Ce_{0.10}Sr_{0.15}Cr_{0.95}Ru_{0.05}O_{3-\delta}$ (LCeSCR), $La_{0.85}Sr_{0.15}Cr_{0.80}Ni_{0.2}O_{3-\delta}$ (LSCN) and $La_{0.75}Ce_{0.10}Sr_{0.15}CrO_{3-\delta}$ infiltrated with Ni (LCeSC-Ni). Because of the major catalytic activity of the Ni nanoparticles in H_2 dissociation, oxidation, and surface diffusion of H species, the highest flow was found utilising LCeSC-Ni coated membrane. Escolàstico *et al.*[190] tried to develop metallic layer for permeation membranes based on $La_{5.50}WO_{11.25-\delta}$/$La_{0.87}Sr_{0.13}CrO_{3-\delta}$ composites. Porous 10 um thick Pt layer was employed as reference, and sputtered layers of Cu and Cu-Pd were investigated. Authors also present the amount of metal per surface unit of the membrane, which is a generally lacking information when it comes to surface modified membranes. It can be said that, in addition to the inherent catalytic activity of each metal, the catalytic surface area plays an essential impact.

The catalytic surface area varies based on the coating technique and metal, in this particular case, with Cu particles being smaller than Pd particles, which made a smooth layer. Controlling the particle size generated might boost the catalytic activity of these layers even further[190]. Finally, multiple authors highlight the contribution from water splitting reaction, that contribute to increase permeated H_2, thanks to the presence of water vapour [147], [149], [150], [168], [188], [190]. A small schematic representation of hydrogen permeation is reported in Figure 12.

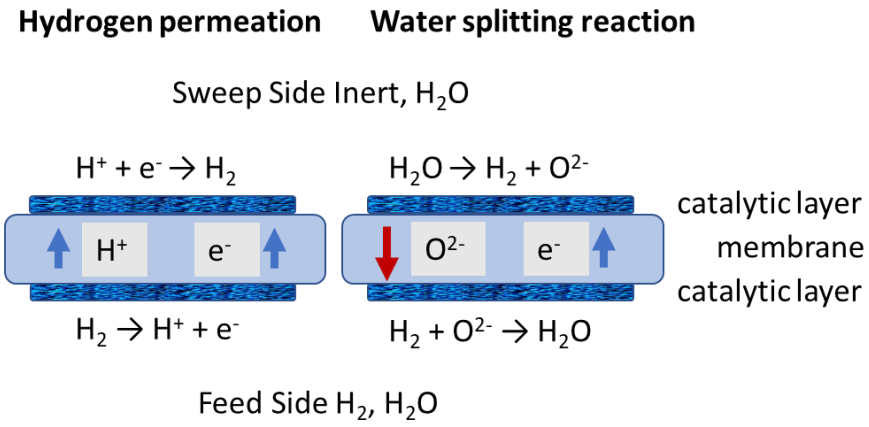

Figure 12 Schematic representation of hydrogen transport.

In conclusion, the catalytic layer bears not only responsibility to avoid adsorption kinetic limitations, but can also affect apparent hydrogen permeation, catalysing the water splitting reaction [188]. Often, in literature the role of morphology and characteristics of the metallic catalyst is not considered, even though it has been reported to affect overall apparent permeation.

2. Aim of the work

Hydrogen has the potential to provide an economically viable, socially beneficial, and energetically efficient solution, and it could be viewed as a pillar of the energy transition, a critical process to contrast global warming and other problems associated with traditional energy systems[10], [11]. The current hydrogen production is mainly composed by Fossil Fuel technologies without CCUS (ca. 82% Mt of H_2)[38]. Advanced membrane technology may enable recovery from poor purity or low-pressure hydrogen streams that would otherwise be uneconomical using PSA or cryogenic methods. [1], [61]. In the context of hydrogen separation using membranes, mixed Proton-Electron Conductor (MPEC) represents a potential low-cost hydrogen purification option with almost 100% selectivity and strong chemical and thermal stability[3].

In this thesis, ceramic membranes with composition $BaCe_{0.65}Zr_{0.20}Y_{0.15}O_{3-d}$-$Gd_{0.2}Ce_{0.8}O_{2-d}$ (BCZY-GDC) are employed as separating agent for H_2 streams. The membranes have asymmetric architecture and are composed of a dense active layer and a porous support layer with same chemical composition to avoid any thermal expansion mismatches. Porosity layer will be investigated, employing different porosity shaping methods to obtain randomised porosity or aligned, low-tortuous porosity with, respectively, Tape Casting and Freeze casting shaping methods. Different porosities have investigated to avoid mass transfer limitation previously experienced by researchers [3].

For what concerns metal catalyst topic, in literature, generally, to avoid surface adsorption kinetics, a metal catalyst is employed. In the majority of cases Pt is the preferred employed metal[129], [146], [147], [149], [150], [165], [168], [184], [186], [188], [189], and is deposited in both sides of the ceramic membrane. Some interesting piece of literature have been investigating more in deep the effect of the catalyst morphology on the hydrogen apparent permeation[185], [186] and the catalyst species [187], [190]. The goal of this thesis is to set a structured study on the catalyst deposition method in order to observe how modification can affect apparent hydrogen permeation, along with the effect of porous layer characteristics, with the goal of taking into account all of the factors that contribute to apparent hydrogen permeation.

3. Materials and methods

3.1 Membrane production

The following procedure was followed for membranes produced by Tape Casting porosity shaping method. The same procedure was employed for both symmetric and asymmetric membranes.

For the production of the porous substrate, BCZY ($BaCe_{0.65}Zr_{0.20}Y_{0.15}O_{3-\delta}$, Specific Surface Area (SSA) = 5.8 m^2g^{-1}), supplied by Marion Technology and GDC powders ($Gd_{0.2}Ce_{0.8}O_{2-\delta}$, SSA = 6.8 m^2g^{-1}, supplied by FuelCellMaterials in a ratio equal to 50:50 vol %, were used as starting material. Rice Starch (RS, Fluka, Germany), with average particle size of 5-6 µm was used as sacrificial pore forming agent. The amount of pore former was fixed at 40 vol.% of the BCZY powders. On the other hand, BCZY (SSA = 12.2 m^2g^{-1}, supplied by Marion Technology) and GDC powders in a ratio equal to 50/50 vol % were used for the production of the dense membrane. ZnO (Sigma Aldrich) was directly added into the tape casting suspension to promote the membrane densification. The total amount of the sintering aid was fixed at 1 wt %. The slurries were prepared by adding to the starting ceramic powders the desired amounts of solvent (azeotropic mixture of ethyl alcohol and methyl ethyl ketone (EtOH-MEK), Sigma–Aldrich), deflocculant (glycerinetrioleate (GTO), Fluka), binder (Butvar B98, Monsanto Co., St Louis, MO, USA) and plasticizer (Santicizer 160 Monsanto Co., St Louis, MO, USA). The ball-milled suspensions were deaerated under vacuum and cast on a moving Mylar carrier (v=6 mm s^{-1}) obtaining, after solvent evaporation, green tapes with the desired thickness. The BCZY-GDC green tapes were punched in discs of 24 mm in diameter. An uniaxial warm press was used to laminate the green tape layers to produce the asymmetrical BCZY/BCZY-GDC bilayers. Two porous and 1 dense discs were stacked between parallel steel plates and heated at 55 °C under 0.7 bar of pressure. Green asymmetric structures were finally debinded and sintered at 1500 °C for 4 h[3], [191]. For the production of symmetric membranes, the same slurry used for the production of the dense layer previously discussed was selected. A thick green tape of ≈ 200 µm was obtained by adjusting the height of the doctor blades and 4 discs of 24 mm in diameter were punched and stacked together by thermocompression and heat treated, using the same condition described above.

For what concerns membranes produced by Freeze Casting porosity shaping method, the procedure employed is reported hereafter. For the porous support, BCZY ($BaCe_{0.65}Zr_{0.20}Y_{0.15}O_{3-\delta}$, Marion Technologies, France) and GDC powders ($Gd_{0.2}Ce_{0.8}O_{2-\delta}$, FuelCellMaterials, USA) were mixed in 50:50 vol% with 1 wt% ZnO (Sigma Aldrich, Italy) as sintering aid. Distilled water was used as solvent, polyvinyl alcohol (PVA, Sigma Aldrich, Italy) as binder and Surfynol SE-F (Evonik Industries, Germany) as antifoaming agent. The powder/water ratio of the slurries was fixed at 20/80 vol% and the antifoaming amount set to 0.60 % in weight. The slurries were prepared at room temperature adding the deflocculant and the powder to the solvent. After 1 h of magnetic stirring, the surfactant and the binder were added to produce the final suspension. The as-prepared slurry was then poured into a circular crown silicon mould supported on metal plate and put in a freeze-drier (Lio 3000 PLT, 5 Pa, Italy) at -40 ◦C for 3 h with a freezing rate of 30°C h^{-1}. For the preparation of the dense layer, screen printing technique were considered. The inks were obtained by mixing BCZY ($BaCe_{0.65}Zr_{0.20}Y_{0.15}O_{3-\delta}$, Marion Technologies, France) with specific surface area (SSA) of 4.92 m^2g^{-1} (d50 = 0.97 µm and d90 = 1.73 µm), GDC ($Gd_{0.2}Ce_{0.8}O_{2-\delta}$, SSA: 5.6 m^2g^{-1}, d50 = 0.49 µm and d90 =

2.17 µm, FuelCellMaterials, USA) in 50:50 vol% and 1 wt% ZnO (Sigma Aldrich, Italy) ceramic powders, whith terpineol (Sigma Aldrich, Italy), glycerine trioleate and ethyl cellulose (EC, 15–25 mPa s, Sigma Aldrich, Italy) as the solvent, dispersing agent and binder respectively. The screen-printing inks were prepared at room temperature adding the deflocculant and powder to the solvent and mixing the suspension in a polyethylene jar with ZrO2- based grinding beads. After 24 h of ball milling, ethyl cellulose was added to the suspension and ball-milled for 3 h. The as-prepared inks were forced in a three-roll mill (Exakt 80E, Norderstedt, Germany) to obtain a more homogeneous and structured system. After demoulding, samples obtained by freeze casting were heat treated up to 1200 °C for 2h and then screen-printed using a 165-mesh screen and dried in IR furnace at 80 ◦C for 30 min. The deposited samples were finally sintered at 1600 °C for 4 h[192], [193].

3.2 Permeation testing

The membrane leak rate was determined using the same reactor that was used for H_2 permeation, as explained below. At room temperature, the leak rate was evaluated using a polymeric hand-carved o-ring, a commercial septum (CrossLab non-stick BTO inlet septa), a mixture of 50% H_2 in He (H_2%vol.) as feed stream, and Ar as sweep stream, while the quantity of leaked feed gas in the sweep current was measured. Preliminary experiments with non-permeable alumina discs revealed no leaked gas in order to establish a rigorous testing technique. The arbitrary parameter introduced to monitor the gas tightness of fresh membranes was calculate as follows:

$$He_{leaked\,\%} = \frac{C_{He,sweep}F_{sweep}}{C_{He,feed}F_{feed}} * 100 \qquad (37)$$

Where $C_{He,sweep}$ and $C_{He,feed}$ are the concentration of He in the sweep stream and feed stream respectively, while F_{sweep} and F_{feed} are the total flow of the sweep stream and feed stream. With levels of leaked He less than 0.5%, the gas tightness of the membranes was deemed satisfactory. This choice was experimentally assisted observing the He leak at room temperature of a membrane that appeared intact but showed microfractures, detected with SEM analysis. Abovementioned membrane revealed a He of 0.8%.

Before determining membrane permeation performances, both surfaces of the membrane were activated with Pt. Activation procedure is reported hereafter. Tetraammineplatinum(II) nitrate (Premion®, 99.99%) solution, with the suitable concentration, was deposited on the membrane surfaces and then dried in oven at 50°C for 1 h to obtain a total Pt (metal) amount on the dense and porous side reported in experimental section.

During the sealing phase and soon before the permeation testing, the Pt precursor was reduced to metal Pt directly in the reactor setup.

Permeation experiments on disk-shaped samples with a diameter of about 15 mm were performed to determine hydrogen permeation in a temperature range of 350 to 750 °C. The measuring setup consists of a handcrafted double chamber quartz reactor with independent feed and sweep portions. To obtain an acceptable level of leakage, the reactor is sealed with single-use silver alloy rings and kept at 750°C for 24 hours. The input gas was a combination of H_2 and He, whereas the

sweep gas was pure Ar. All gaseous currents were regulated by mass flow (MFC), with feed and sweep gas flow rates of 80 and 150 mL min^{-1}, respectively. At 28 °C, both streams were humidified to saturation. Hydrogen concentration in permeate gas was determined using an Agilent Technologies 490 Micro GC equipped with a Molsieve5A capillary module. An appropriate sealing was determined by monitoring He content at the permeate side, and results were considered acceptable when He leaked was below 5%, following calculation in Eq. 37.

Leaked hydrogen was subtracted form permeation results following the equation reported hereafter:

$$J_{H_2,corrected} = J_{H_2,sweep\ stream} - J_{H_2,leaked}$$

$$J_{H_2} = \frac{F}{A} C_{He,sweep} \frac{C_{H_2,feed}}{C_{He,feed}}$$

Data reported in the present study were recorded at a steady state after 30 minutes of stabilization. Temperature was monitored by a thermocouple close to the membrane. Each permeation point was the result of 15 analysis.

3.3 Set-up design

The set-up design is necessarily linked to the shape assumed by the ceramic membrane. This elaborate will employ disk shaped ceramic membranes, because available production technologies allow the preparation of this particular structure. It is worth noticing that, in literature, disk membranes have been widely employed for fundamental research studies and screening of new materials [151]. The use of disk-shaped membranes necessarily poses some challenges in reactor design, in terms of multiple concentric tubing for separate chambers and, mostly, correct sealing of different chambers, avoiding simple industrial screwing flange, as intense mechanical stress would crack the membrane. Some characteristics of the employed set up will be listed in the following section. Hereafter in **Error! Reference source not found.** the Process Flow Diagram (PFD) is reported.

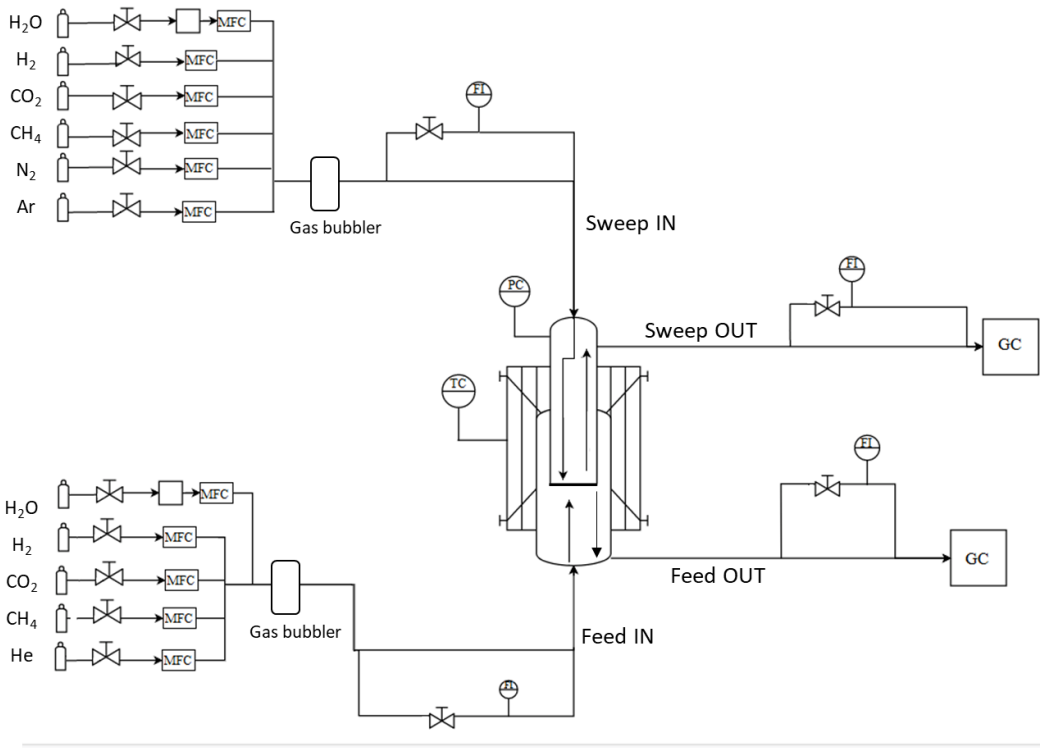

Figure 13 PFD of the permeation set-up

As previously explained in the Permeation testing section, the setup consists of a double chamber reactor with a handmade silver o-ring for membrane sealing. The two chambers are equipped with an inlet and an outlet and allow flowing separate gaseous streams, that in this elaborate will be named feed and sweep gas, currents or streams, as well as retentate and permeate respectively. A detailed visual representation of the sealing section of the reactor is reported in **Error! Reference source not found.**.

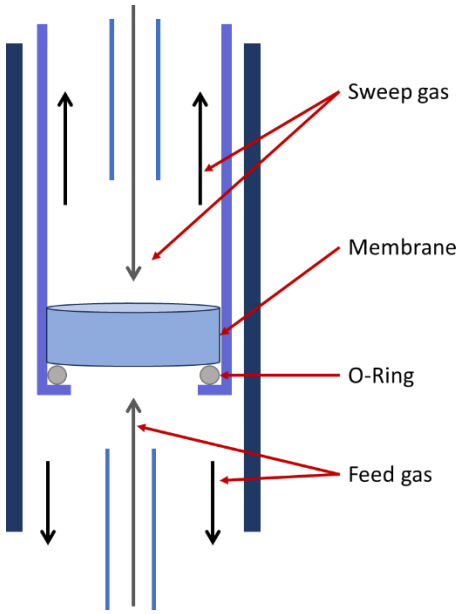

Figure 14 Detailed visual representation of sealing section of the reactor where feed section and sweep section meet.

The membrane is pressed and kept in place thanks to mechanically strain induced by a metallic spring, carefully selected to ensure acceptable sealing and avoid mechanical failure of the whole membrane-o-ring system. The membrane location is set between the two chambers, where feed and sweep current could potentially meet. This can allow the presence of hydrogen partial pressure difference, producing the necessary driving force to ensure permeation. Asymmetric membranes were positioned in the reactor so that sweep stream was in contact with porous layer and feed stream with dense layer respectively. A picture of the higher section of the rector is reported in Figure 15.

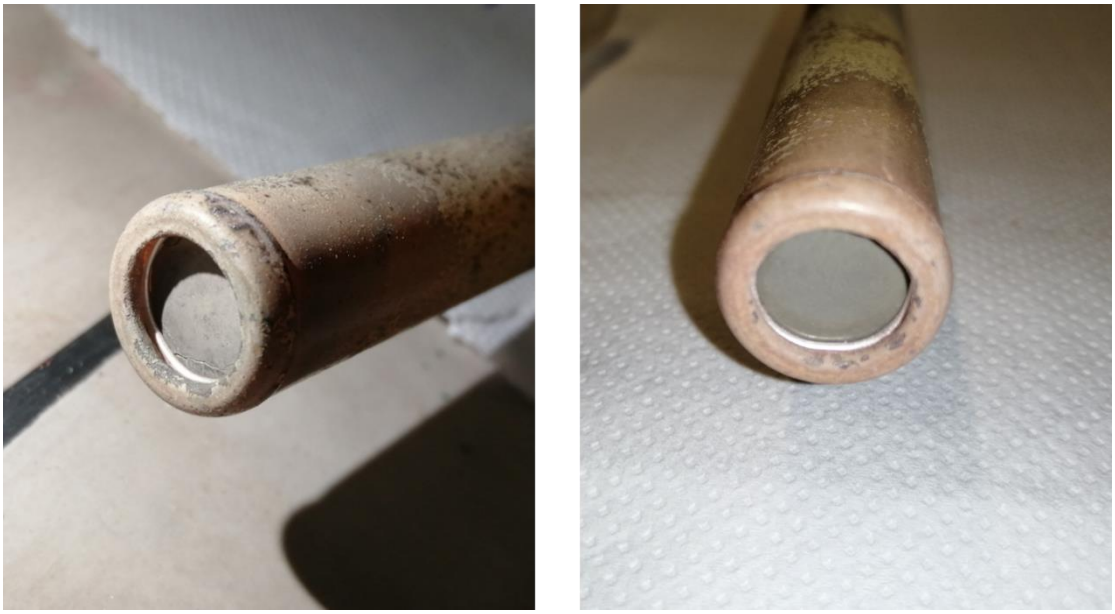

Figure 15 Pictures of higher section of reactor, with mounted membrane and handmade o-ring.

3.4 Sealing procedure.

Obtaining acceptable membrane sealing proved to be more challenging than initially anticipated. This puzzling occurrence is tied to the generally low performance of dense mixed protonic-electronic conducting ceramic membranes for H_2 separation. In literature works, a threshold is established for acceptable permeation measurement [3], [187], [188], [190]. Following this practice, it was determined that for this elaborate, to consider data acceptable, the amount of leaked He must be less than 5%. The initial attempts at sealing were pursued through the use of commercially available copper o-rings; however, these efforts were ultimately unsuccessful. The use of gold is also reported in literature [194], though the prohibitive cost couldn't be supported and made this approach unavailable, mainly due to reduced availability at the time of experimental data production and to single use of handmade o-rings, that one used were discarded. Subsequently, handmade commercial silver alloy was employed, and the results indicated that acceptable sealing could be achieved. In light of the natural variability in sealing conditions that arose as a result of the necessary temperature switching during experimental procedures, a routine leak gas analysis was implemented throughout the entirety of the analysis. This methodology was employed to monitor the amount of leaked He in the permeate stream, and to accurately determine the permeated H_2 value by making appropriate corrections based on the collected data. An empirical approach has

been identified experimentally in order to obtain adequate sealing. The temperature ramp used during the experiment is described further down (**Error! Reference source not found.**).

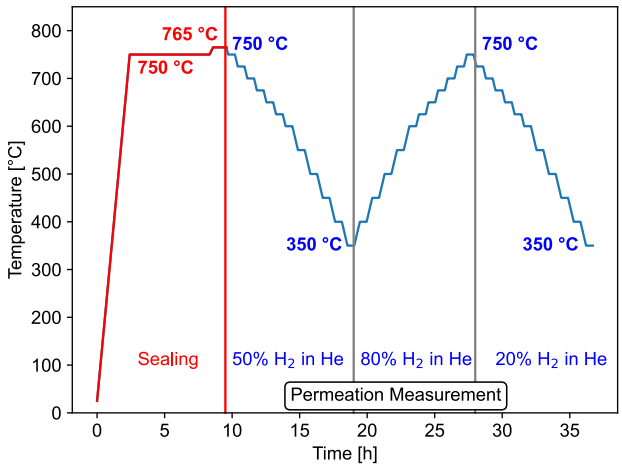

Figure 16 Temperature program of a typical permeation experiment. In red is reported the typical sealing routine, in blue is reported typical thermal steps routine for permeation performances measurements.

As shown in **Error! Reference source not found.**, to achieve acceptable sealing the membrane-silver ring system is kept at 750°C overnight and the next day reaches 765°C. At this point permeation if control parameter is acceptable (as usually happens) and measurements are carried with the following order: 50% H_2 in He (%H_2 in vol), 80% H_2 in He (%H_2 in vol), 20% H_2 in He (%H_2 in vol). Ramps and temperature steps are the same for each composition. The empirical procedure was determined keeping a balance between the following objectives:

- Price of the handmade o-ring
- Sintering behaviour of metal catalyst
- Acceptability of sealing.

The o-ring is obtained from a 1 mm commercial silver thread, with composition ~90% Ag and 10%Cu. The use of pure silver could have facilitated the sealing process, but the cost savings and the availability at the time of experimental data production, justified the choice. This also sets the maximum operating temperature, which is required to maintain the mechanical stability of the handcrafted o-ring. In **Error! Reference source not found.** is reported Au-Cu phase diagram, where the composition of the commercial thread is highlighted. To avoid presence of liquid phase in the o-ring and thus cause unacceptable leak, the temperature must be kept below 779°C.

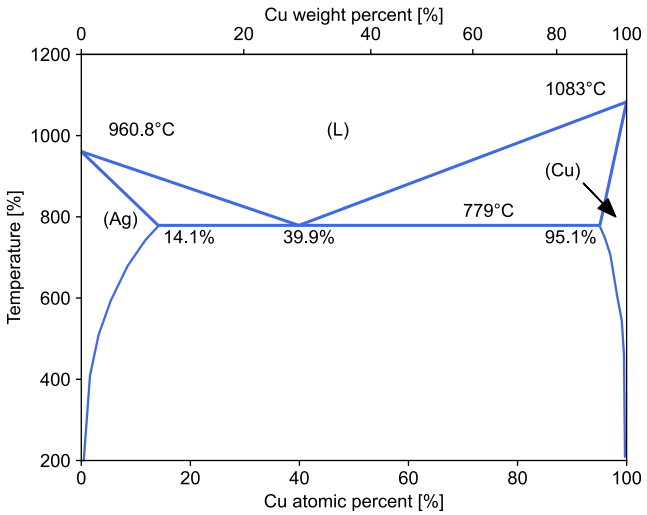

Figure 17 Ag-Cu phase diagram[adapt.][195].

To minimise undesirable thermal sintering of metallic catalyst particles during permeation, which might impact results when monitoring membrane performances, the last step at 765°C is required before data collection begins. Implementation of this step in the procedure can actually improve dramatically data evaluation, as different phenomena concur to apparent permeation and data assessment has previously been found to be hampered by sintering [186]. Metal particles are notoriously subject to thermal sintering at temperatures below the melting point of the bulk metal [196]. Heterogeneous metal catalysts are commonly utilized in the form of dispersed particles in order to optimize their efficiency, as this leads to an increase in the catalytically active surface area. Simultaneously, the greater surface area promotes the thermodynamically favourable process of agglomeration, resulting in the formation of fewer, larger particles. This phenomenon, known as sintering, plays a significant role in determining the long-term performance of practical catalysts [197]. In order to avoid any form of data misjudgement, the temperature during the sealing is raised above the maximum temperature of permeation testing.

Finally, to ensure data reliability, Ar and He were chosen as sweep and co-feed gases. The use of two separate gases for permeation characterization is required to detect consistent leaks in the setup, and the decision of co-feeding He is due to fugacity similarities with H_2. A series of pictures of fresh and spent membrane and handmade o-ring are reported in Figure 18.

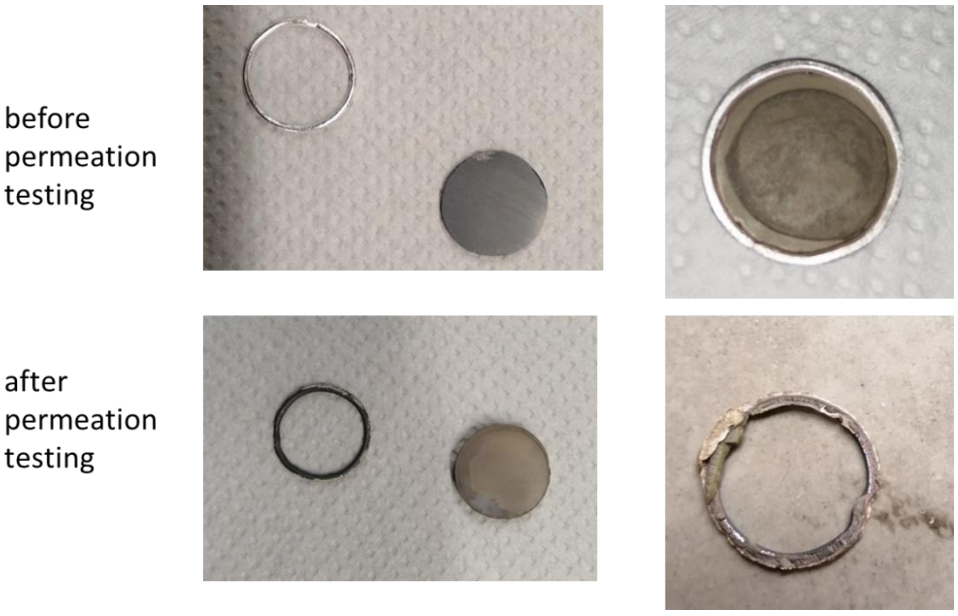

Figure 18 Picture reporting the appeareance of membranes and o-rings before and after permeation.

3.5 Characterization

3.5.1 Scanning Electron Microscopy – Energy Dispersive X-Ray Spectroscopy (SEM-EDS)

Scanning Electron Microscopy analysis were carried out on a E-SEM Zeiss EVO 50 Series (Carl Zeiss, SpA) equipped with microanalysis system INCA Energy 350 EDS (Oxford Instrument Analysis). Voltage was set to 20KV and time for spectra collection was 60 seconds.

SEM pictures were acquired on both sides of the membranes before and after permeation testing. Pt particle measurements were carried out employing ImageJ software.

Equation employed for particle dimension lognormal fitting is:

$$y = y_0 + \frac{A}{\sqrt{2\pi}wx} e^{\frac{-\left[ln\frac{x}{xc}\right]^2}{2w^2}}$$

3.5.2 X-Ray Diffraction Analysis (XRD)

To characterize membranes phases in terms of composition and crystalline structure X-Ray Diffraction analysis were carried out on a Philips PW1050/81 equipped with graphite monochromator and controlled by a PW1710 (Cu Kα, λ = 0.15418 nm) unit. Investigated angles °2θ are in a range from 20° to 80° with a scanning velocity of 40°/h.

3.5.3 Thermo-Gravimetric Analysis – Differential Scanning Calorimetry - Mass Spectrum (TGA-DSC-MS)

Sintering behaviour of BCZY and GDC precursor powders was studied through TG measurements. The setup is composed of a TGA/DSC unit (Netzsch STA 449C Jupiter TGA/DSC) couple with Mass Spectrum (Netzsch Aërlos QMS 403C MS). The temperature program is composed of a ramp of

5°C/min from 25°C to 1000°C with an isothermal step of 30 min followed by rapid cooling. Mass Spectrum were recorded for signal of Ar, CO_2 and H_2O. The aforementioned analysis was carried out in the Department of Chemical Engineering, Faculty of Natural Sciences, Norwegian University of Science and Technology.

3.5.4 Solvent Contact Angle Measurement

Contact angle of different solution was evaluated employing dense pellets of BCZY-GDC and the single phases BCZY and GDC, obtained by pressing. All the sample were polished before contact angle measurements. The apparatus employed for contact angle measurement was an Optical System Drop Shape Analyzer DSA 30S (Krüss GmbH).

4. Results and discussion

The primary and inaugural segment of this elaborate shall primarily address the matter of identifying a sturdy and resilient routine for characterizing the hydrogen permeation performance of ceramic membranes under high-temperature conditions. In order to accomplish this initial objective, it is imperative to establish a suitable configuration that permits the manipulation of various hydrogen partial pressures, temperature intervals spanning from 350°C to 750°C, and an array of gas mixtures.

4.1 Precursor characterization

To characterize membrane precursor powders sintering behaviour Thermogravimetric analysis coupled with Mass Detector of evolved gaseous species has been employed. Results are reported in Figure 19.

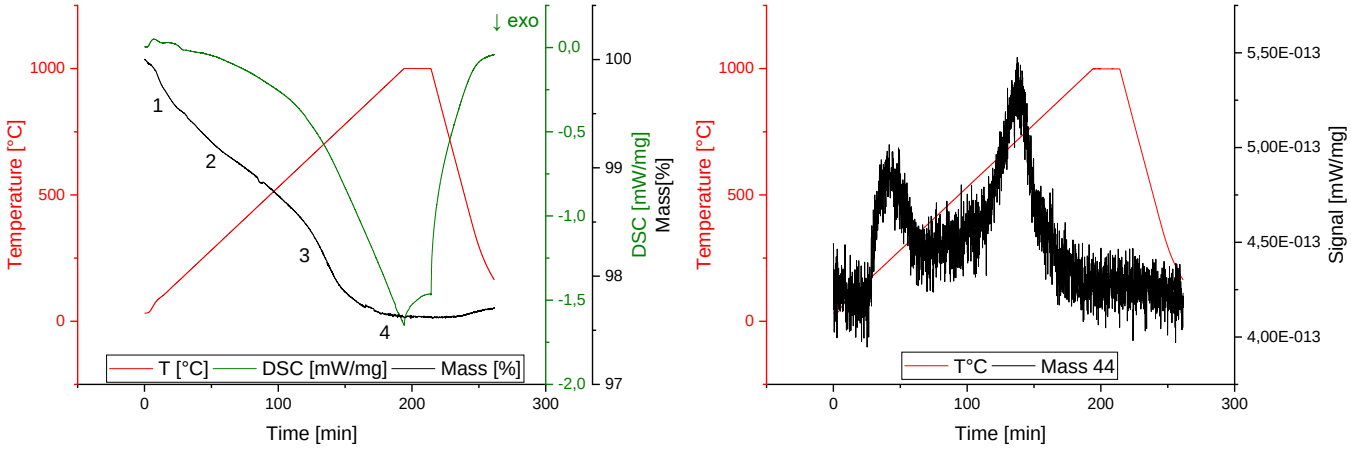

Figure 19 TGA-MS analysis of membrane precursor powders. Precursor

TGA results can be divided in 4 regions, reported on the figure. First region (2-25 min) the temperature varies from 30 to 150 °C and there is mass loss of ~0.10%, corresponding to an endothermic peak in DSC analysis, and attributed to residual water loss due to brief contact with atmosphere while charging the sample. Region 2 (40-100 min) corresponds to a loss of ~0.60% mass, when temperature varies between 200 and 500°C. This was attributed to decomposition of residual carbonate compounds present in the mixture. Region 3 (115-160 min) corresponding to temperature change between 600 to 830 °C, present a weight loss of ~0.84%. This region is also attributed to decomposition of residual carbonate compounds. Region 3 (170-230 min) corresponds loosely to the isothermal step of the temperature program, and for what concerns weight loss there's no evident signal in the TGA measurements. DSC measurement highlight an exothermic peak that has maximum during isothermal step a 1000°C, probably due to sintering of particles[191]. Analysis of evolved gas from thermal treatment of sample are reported in Figure 19 (right). It is possible to observe presence of two different peaks in Region 2 and Region 3 that were registered with mass 44, corresponding to CO_2 gas evolution over the sample. No other significant MS signals were observed during the investigation.

4.2 Pt particle deposition

In section 1.7.4 the role and effect of metal catalyst is broadly discussed. Published works are mostly characterized by thick-porous layer of Pt catalyst deposited on both sides of membranes, typically through screen printing method [149], [150], [184], [185], [187]–[189]. One of the negative aspects associated with the aforementioned approach pertains to the insufficiency of information concerning the quantity of Pt that has been deposited as well as the morphology of the Pt catalyst. Consequently, in order to provide a more comprehensive analysis, it was deemed scientifically valuable to differentiate our approach from the contemporary literature and test an alternative method of Pt deposition. Initial exploration of the Pt deposition technique was conducted on the surface of a dense membrane, and subsequently analysed through the use of SEM analysis to determine the optimal particle morphology output. The ensuing table outlines the preliminary conditions for the deposition of the precursor.

Deposition solvent (% vol)	Drying temperature (°C)	results
100% H_2O	50	Figure 20a)
50% H_2O – Acetone	50	Figure 20b)
100% H_2O	70	Figure 20c)
50% H_2O - Acetone	70	Figure 20d)

Table 6 Preliminary deposition condition for metal precursor

Preliminary deposition tests were conducted by leveraging the utilization of water and a mixture of water and acetone. To investigate the impact of temperature on the precursor distribution, two distinct temperatures were employed, namely 50°C and 70°C. It is noteworthy to mention that the deposited precursor exhibited a sensitivity towards X-Ray irradiation. Owing to this sensitivity, SEM pictures were collected only after deposition to avoid the loss of metal precursor on the membrane's surface subsequent to the first experiment. Figure 20 reports results obtained from the listed experiments.

a)

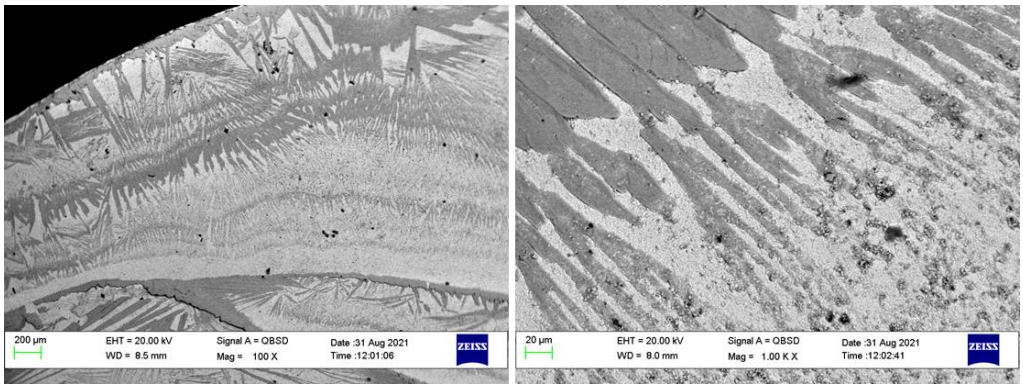

b)

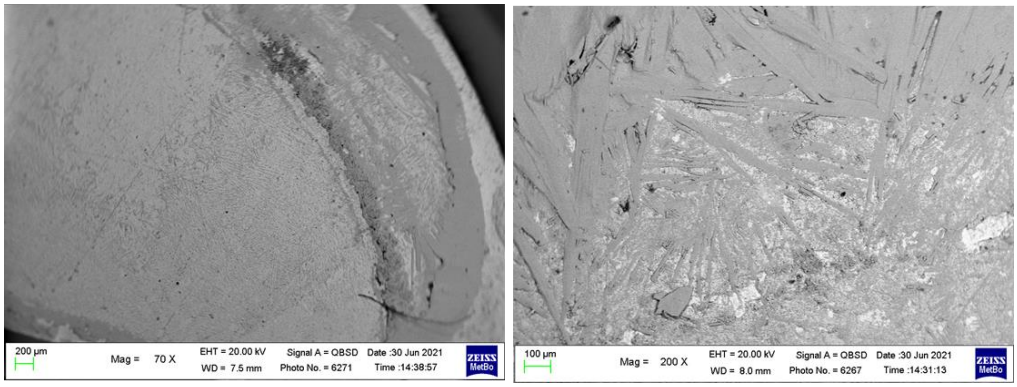

c)

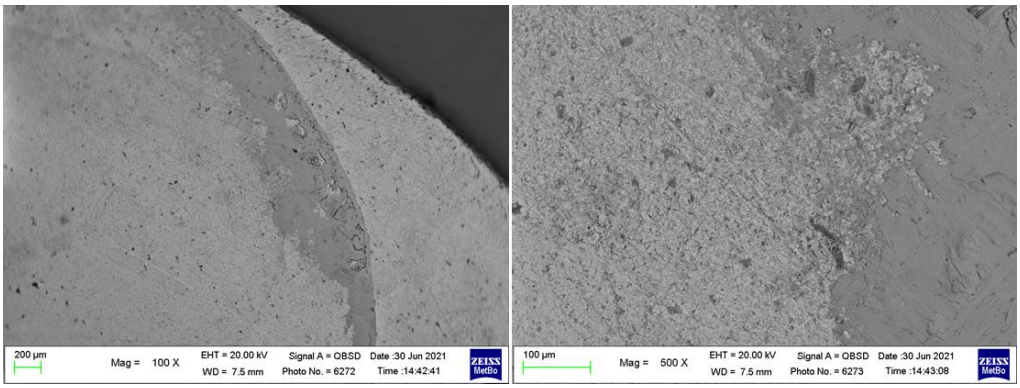

d)

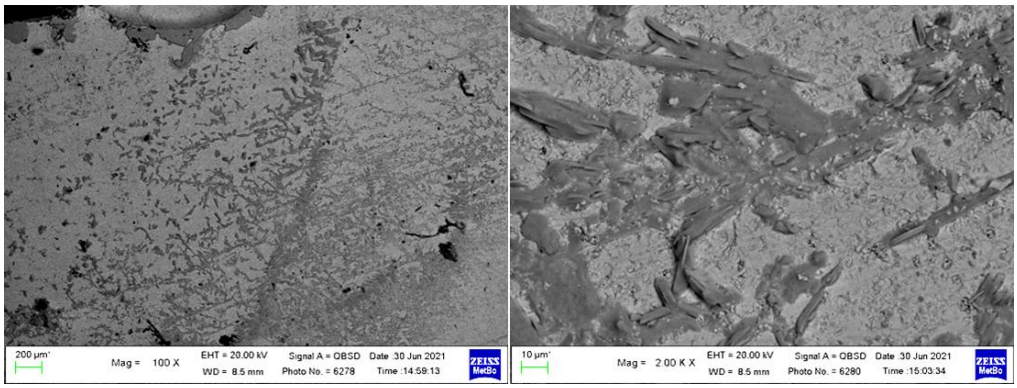

Figure 20 SEM acquisition of preliminary metal deposition results. a) H_2O, 50°C; b) H_2O: C_3H_6O, 50°C; c) H_2O, 70°C; d) H_2O: C_3H_6O, 70°C.

Brief discussion of experimental results of preliminary metal deposition is reported hereafter. Observing Figure 20a) it is possible to observe the metal precursor with black profiles on top of the membrane. The obtained morphology resembles strips, that seem to be distributed on the whole

membrane surface, even though some sections seem to present higher amount of the precursor. Similar conclusion can be drawn from Figure 20b) to some extents. Strips are still the preferential distribution arrangement, though a higher degree of inhomogeneity is clearly visible, resulting in section of the surface with significant absence of precursor. A temperature increase from 50 to 70°C in the drying step revealed itself as deleterious for water dispersion (Figure 20c)), resulting in fewer strips on the surface and big conglomeration of precursor. For what concerns H_2O:C_3H_6O mixture dried at 70°C (Figure 20d)), the SEM acquisitions show the presence of some precursor build up areas. After these preliminary results, aqueous solution dried at 50°C was deemed appropriate for deposition on dense side of the membrane with a coverage of *ca.* 0.15 Pt mg cm^{-2}. A simplified scheme for Pt metal catalyst deposition is reported hereafter to illustrate the different steps.

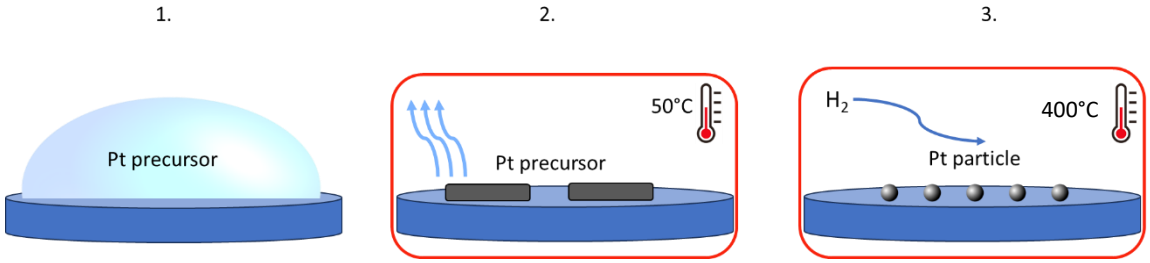

Figure 21 Simplified scheme for Pt catalyst deposition procedure.

It is worth reporting that the reducing step for Pt catalyst happens, conveniently, at the same time of the sealing procedure, reported in red in Figure 21.

4.5 Dense ceramic BCZY-GDC membranes

The first exploration focused on dense symmetric membranes testing. The sample investigate was named BCZY-GDC-D and was produced by Tape casting shaping method. Further pieces of information are reported on Table 7.

Membrane	Composition	Thickness (µm)	Pt amount	architecture
BCZY-GDC_D	$BaCe_{0.65}Zr_{0.20}Y_{0.15}O_{3-d}$-$Ce_{0.85}Gd_{0.15}O_{2-d}$	670	0.15 Pt mg cm^{-2}	Dense

Table 7 Structural information of ceramic membrane BCZY-GDC-D.

Permeation performances were carefully investigated by exploring the effect of: (1.) temperature and (2.) hydrogen partial pressure in the feed stream. Results are reported on Figure 22. The temperature range investigated was between 550°C and 750°C while inspected hydrogen partial pressure were 50% and 80% H_2 in He, %vol.

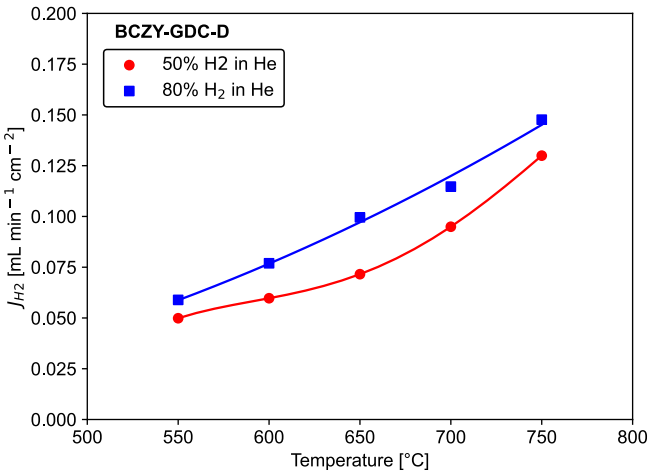

Figure 22 J_{H2} flux (mL min^{-1} cm^{-2}) of membrane BCZY-GDC-D as a function of temperature and feed composition (50% and 80% H_2 in He, H_2 vol%). Both current are humified at 28°C.

Permeation results of membrane BCZY-GDC-D reveal that H_2 flows are positively affected by temperature increase, independently from the investigate feed composition. For what concerns the effect of H_2 partial pressure, permeation values benefit from the shift from 50% to 80% H_2 in He. These two observations are in good agreement with Wagner equation (Eq. 35).

4.6 System reliability testing

Upon conducting empirical investigations and determining the most optimal permeation setup and conditions, it became apparent that the entire process necessitated validation through comparison with the results obtained from the existing literature. In order to achieve this goal a dense membrane with composition BCZY-GDC was employed and confronted with published data from Rebollo et al.[129], who used analogous membrane systems. In Table 8 it is possible to observe necessary information on the membrane considered in this section.

Membrane	Composition	Thickness (µm)	Pt amount	architecture
BCZY-GDC_D	$BaCe_{0.65}Zr_{0.20}Y_{0.15}O_{3-d}$-$Ce_{0.85}Gd_{0.15}O_{2-d}$	670	0.15 Pt mg cm^{-2}	Dense
Ref.*	$BaCe_{0.65}Zr_{0.20}Y_{0.15}O_{3-d}$-$Ce_{0.85}Gd_{0.15}O_{2-d}$*	700*	20 µm Pt porous layer*	Dense*

*Table 8 Information summary for tested dense membrane. *=[129]*

Figure 23 plots the H_2 flows for dense membranes with identical composition, one from literature and one from results reproduced in the laboratories facility with the permeation set-up build in this project. Hydrogen flows are plotted as a function of temperature and hydrogen partial pressure in the feed current. Permeation measurements were recorded employing water saturated streams at room temperature (28°C).

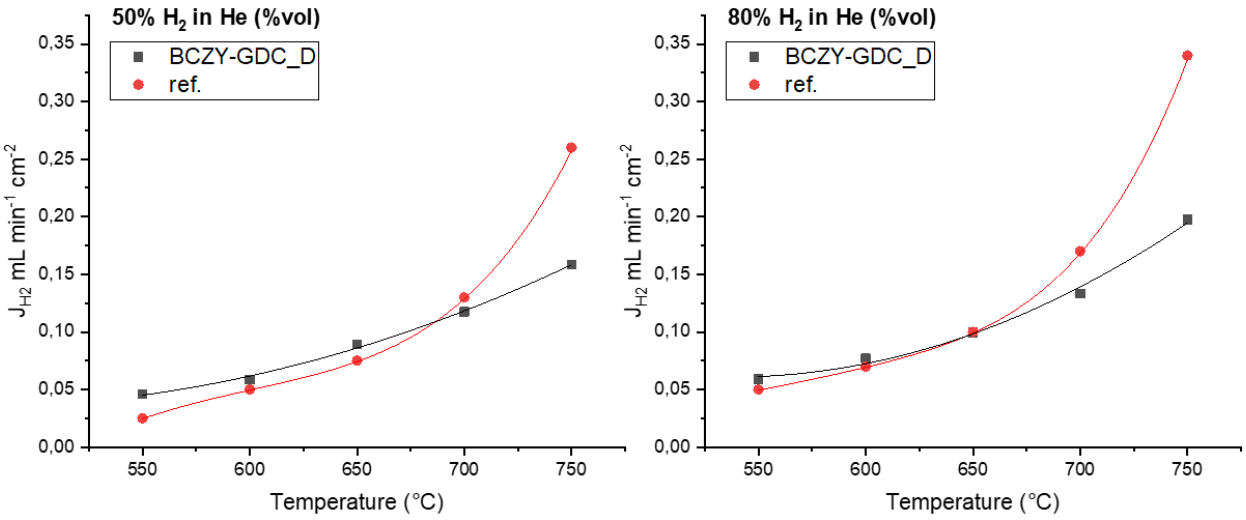

Figure 23 H_2 flux (mL min^{-1} cm^{-2}) as a function of temperature and different feed composition (80%, 50% and 20% H_2 in He, H_2 %vol). Both feed and sweep streams are humidified to saturation at 28 °C

The condition employed in the permeation measurement should be reasonably similar between the two membranes, and thus results in similar H_2 flows. It is clearly visible an increasing trend in H_2 flows when the temperature is increased from 550°C 750°C, as expected from Wagner equation [81], [104], [130] that regulates permeation in mixed protonic-electronic ceramic conductor. An increase in H_2 partial pressure also resulted in an increase in permeation in both membranes, due to increased driving force. When results at temperatures <700°C are confronted between the two membranes, there is an indication that the performances are comparable and in a narrow range, symptom of a reliable set-up and characterization routine. Membrane BCZY-GDC_D shows a slightly higher permeation flows, due to the thinner layer, that shortens diffusion paths and thus increase H_2 flow, as expected. The main difference is appreciable at temperature ≥700 °C, where the membrane reported in literature show a sharp increasing slope, while membrane BCZY-GDC_D doesn't exhibit the same dramatic increase in permeation. As reported in Surface Modified Membranes introduction section, the water splitting reaction plays an important role in ceramic membranes permeation. To better understand the contributions of the (i) hydrogen permeation and (ii) water splitting reaction to the permeation, the activation energies were calculated from permeation curves obtained with 50% H_2 in He (%vol) with both streams humidified. Activation Energy is calculated by the Arrhenius equation [140]:

$$J_{H_2} = J_0 exp\left(\frac{-Ea}{RT}\right) \quad (37)$$

By plotting ln(J_{H2}) as a function of 1/T, and using the slope to obtain the activation energy. Results are reported in Table 9.

Membrane	Temperature (°C)	Activation Energy (eV)
Ref.	<650	0.88
	>650	1.04
BCZY-GDC_D	<650	0.165
	>650	0.44

Table 9 Activation energies obtained from the H_2 permeation measurements feeding 50% H_2, 50% He.

Activation Energies for the two membranes present similar trends, namely larger value at higher temperatures (>650°C) and lower values at lower temperatures (<650°C). This trend was explained considering the prevailing contribution of water splitting reaction at high temperature [129], while at low temperature the decrease in activation energy is a consequence of the higher contribution of proton transport. Consequently, the significant H_2 flow recorded with the membranes at T> 650°C might be attributed to the increased H_2 generation via water splitting due to the greater oxygen ionic conductivity of the GDC phase. After these considerations a tentative explanation of the permeation behaviour might be the following: when the prevailing contribution to the H_2 permeation is the proton transport (T< 650°C) the effect of layer thickness is evident, and membrane BCZY-GDC_D has slighter increased permeation performances, when the predominant contribution to H_2 permeation is water splitting (T> 650°C), the permeation performances are affected by the amount of Pt that is employed to avoid adsorption kinetics limitation, thus favouring membrane from literature, that is reported to employ a 20 µm thick porous layer of screen printed Pt. In conclusion it can be said that reliability of the set-up was tested and that the set-up and analysis routines positively responded to consistency testing. The SEM characterization of BCZY-GDC_D membrane after permeation testing is reported hereafter.

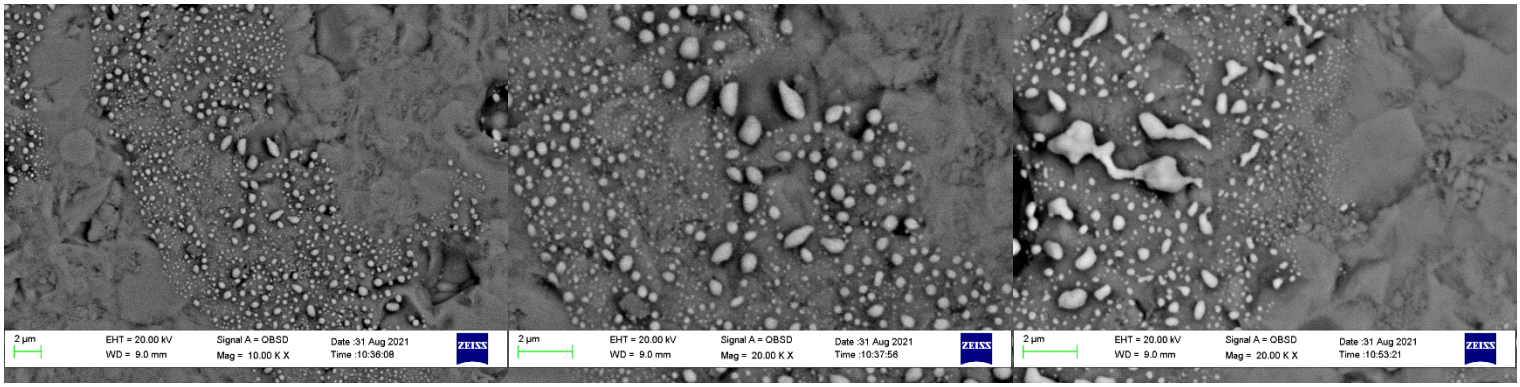

Figure 24 SEM characterization of membrane BCZY-GDC_D after permeation.

From SEM acquisition of tested membrane BCZY-GDC_D (Figure 24) it is possible to observe the shapes of Pt metal on top of the dense surface of the membrane. The precursor's black strips previously observed on Figure 20 coalesce in metal particle with spheroidal shape and variable radius. To better describe Pt catalysts, particle radius was collected assuming perfectly spherical particle and frequency distribution of particle radius is reported hereafter (Figure 25).

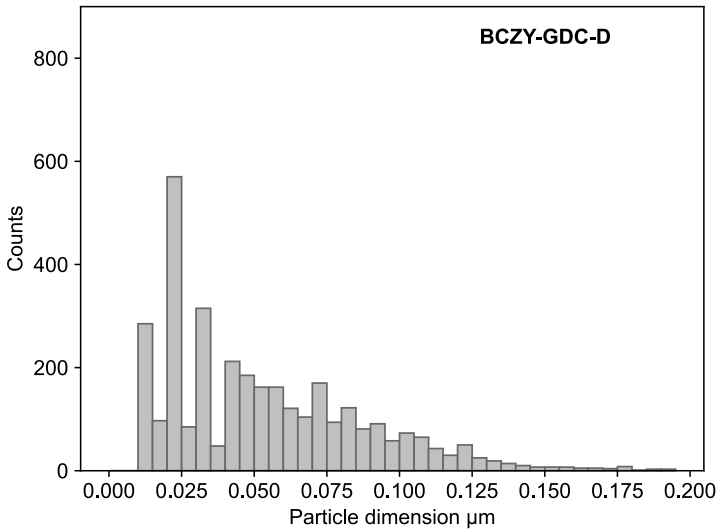

Figure 25 Platinum particle frequency distribution for membrane BCZY-GDC-D.

From SEM pictures acquisition, the average radius of Pt particles is ~0.025 µm. These preliminary results sparked discussion concerning the role of Pt deposited on the sweep side of the membrane (Figure 12), and how the deposition and amount of catalyst could positively affect the reaction of water splitting and, in the end, enhance apparent H_2 permeation.

4.7 Preliminary studies conclusions

This first section of the elaborate focused on producing reliable set-up and analysis routine for ceramic membrane for hydrogen permeation. The first step was to design a reactor suitable for separation and was produced in quartz with two separate chambers for current with different compositions. The sealing of the reactor revealed itself quite irksome but was achieved employing handmade commercial silver alloy o-rings. Empirical tests led to achieve the correct temperature ramps and values to obtain acceptable sealing conditions, measuring leaked He content in permeate current.

An experimental endeavour to establish a fresh technique for Pt deposition was implemented with the assistance of SEM-EDS examination, with emphasis on the morphology of the Pt catalyst. The identified particle's typical dimension was roughly 0.025 µm, exhibiting a spheroidal shape. The sealing process successfully achieved a satisfactory reduction of the Pt precursor. Lastly, the reliability of the whole set-up and routines was tested, employing a dense membrane with composition BCZY-GDC, whose results were already reported in literature. Results showed narrow similarities at temperature below 700°C, linked to similar permeation performances, as expected. At higher temperature (above 700°C), the effect of catalyst amount affected greatly hydrogen flow, due to main WS reaction contribution to permeated hydrogen. This sparked curiosity and led to the next investigation on Pt catalyst amount.

4.8 Tape Casting membranes

As reported in section 1.7.3 Asymmetric membrane, employing a thinned active dense layer would increase the hydrogen permeation, reducing the diffusion paths. This is clear if Eq.36 is observed, where membrane thickness is expressed by the term *L*.

$$J_{H_2} = \frac{1}{4L}\frac{RT}{F^2}\int_{P_{H_2}^{I}}^{P_{H_2}^{II}} \sigma_{tot} t_{H^+}(t_e + t_h) d\ln P_{H_2} \qquad \text{(Eq. 36)}$$

The employment of thin brittle ceramic membranes poses, nevertheless, some technical challenges, in particular the appropriate set-up for such delicate materials. One possible solution might be seen in employing a supporting layer to ensure mechanical stability and avoiding membrane failure. Further complications might arise from compatibility of the two layers, but an interesting approach is to employ the same composition for dense layer and supporting layer [3]. It was deemed appropriate then, to shift the architecture of the membrane toward asymmetric structural design. The concept behind the new design was implemented considering two factors:(i) obtaining thin permeation-active layer, (ii) preserving membrane mechanical stability, especially due to temperature expansion mismatch between layers. The optimal solution was to employ the same material composition $BaCe_{0.65}Zr_{0.20}Y_{0.15}O_{3-d}$-$Gd_{0.2}Ce_{0.8}O_{2-d}$ for both the porous layer and the dense layer, employing tape casting process [191]. This section describes the hydrogen permeation performance of $BaCe_{0.65}Zr_{0.20}Y_{0.15}O_{3-d}$-$Gd_{0.2}Ce_{0.8}O_{2-d}$ (BCZY-GDC) composite planar membranes with asymmetrical architecture, with a particular emphasis on the effect of Pt catalyst amount on permeation, with the goal of maximising the ratio of permeated hydrogen to metal amount. Layer Cer-Cer membranes with a 20 µm thick active dense layer and a 600 µm thick porous BCZY-GDC support were produced by tape casting and impregnated with varying concentrations of platinum to achieve this goal. Membrane production is described in Material and Methods section, further discussion on this topic is beyond the scope of the manuscript. The next figure (Figure 26) presents the diffractogram acquired on a sample 'as sintered', before permeation performance evaluation.

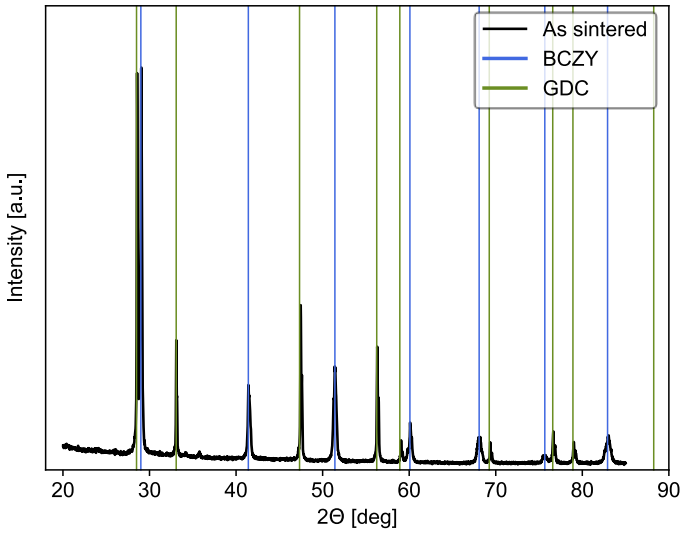

Figure 26 XRD diffractogram of a sample produced by Tape casting porosity shaping method.

The reference patterns of the two phases BCZY and GDC have been reported in Figure 26. The following table lists the sample tested. To simplify comprehension of Table 10, a schematic graphical representation of conventions is reported in Figure 27.

Membrane	Type	Thickness (um)	Diameter(mm)	Deposition	Additional Info
BCZY-GDC-D	Symm.	670		A 0,15 mg cm^{-2} B 0,15 mg cm^{-2}	Side A dense Side B dense
BCZY-GDC-A-1	asymm.	680	14,8	A 0,15 mg cm^{-2} B 0,15 mg cm^{-2}	Side A dense Side B porous
BCZY-GDC-A-2	asymm.	780	14,81	A 0,15 mg cm^{-2} B 1,5 mg cm^{-2}	Side A dense Side B porous
BCZY-GDC-A-3	asymm.	763	14,90	A 0,15 mg cm^{-2} B 4,5 mg cm^{-2}	Side A dense Side B porous

Table 10 Structural information on different membrane and catalyst deposition. For clarity, Side A is in contact with feed stream, while Side B is in contact with sweep stream.

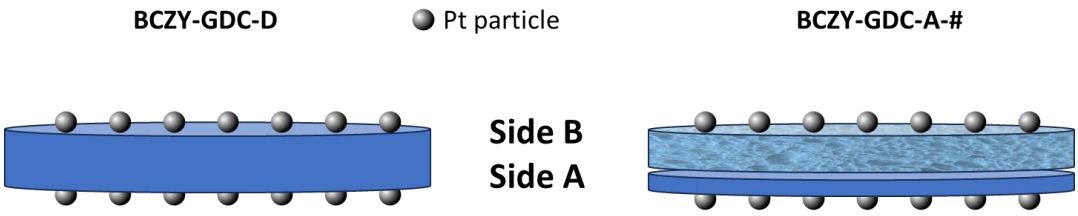

Figure 27 Schematic representation of conventions employed in Table 10.

4 membranes were selected to carry investigations on: one dense symmetric membrane to compare the effect of the thickness of the active layer and 3 supported asymmetric membranes with comparable structure but progressively increasing amount of Pt catalyst, to investigate the effect on the permeation. The variation of Pt amount was relative to the porous side of the membrane, where water splitting reaction happens due to reactor setting and streams configuration (sweep stream is in contact with porous layer of the membrane). The effect of the BCZY-GDC membrane architecture was initially examined by comparing a symmetric dense pellet membrane (sample BCZY-GDC-D) to an asymmetric dense-porous membrane (BCZY-GDC-A-1) made of a thin dense layer supported atop a porous layer. The latter was required to give the thin dense layer mechanical stability. On both sides of the membranes, 0.15 Pt mg cm^{-2} was deposited. The permeability of the membrane was tested at various hydrogen feed concentrations and temperatures. Results of permeation performances are reported in Figure 28.

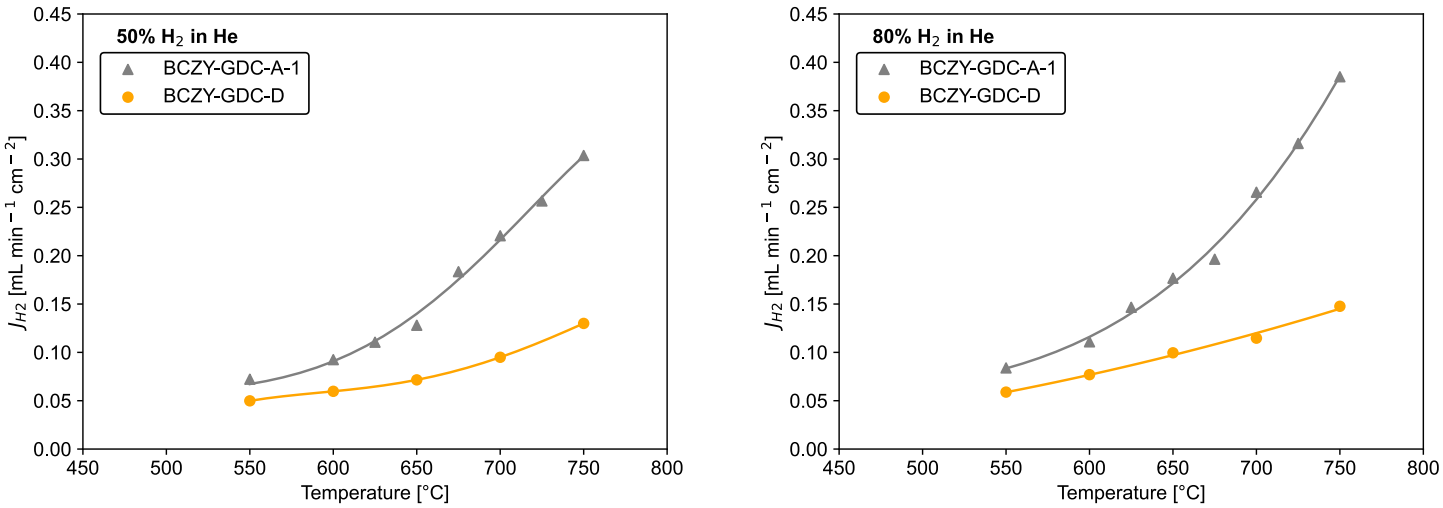

Figure 28 H_2 flux (mL min^{-1} cm^{-2}) as a function of temperature and feed composition (80%, 50% and 20% H_2 in He, H_2 %vol) for membranes BCZY-GDC-D and BCZY-GDC-A-1. Both feed and sweep streams are humidified to saturation at 28 °C.

Each graph displays permeation performance data obtained with a different feed gas composition (80%, 50%, and 20% H_2 in He, % vol.) and presents permeation values as a function of temperature. In every instance, the hydrogen flow increases as the temperature rises and the hydrogen content of the feed current increases. When the two membranes are compared, sample BCZY-GDC-A-1 shows higher hydrogen flow at every investigated temperature and hydrogen composition, and this is ascribed to the asymmetric architecture of the membrane. The aforementioned water splitting reaction is particularly favoured from the asymmetric architecture thanks to two factors: thinner layer, that reduce oxygen ion retro-diffusion path and the asymmetric membrane system's porous section that has greater Pt dispersion than the symmetric membrane's flat dense layer, as expected due to major volume where Pt precursor is distributed. To better confirm this assumption, SEM-EDS images of the surface in contact with sweep gas (water splitting reaction side) were gained after permeation measurement on tested membranes. The results are reported in Figure 29.

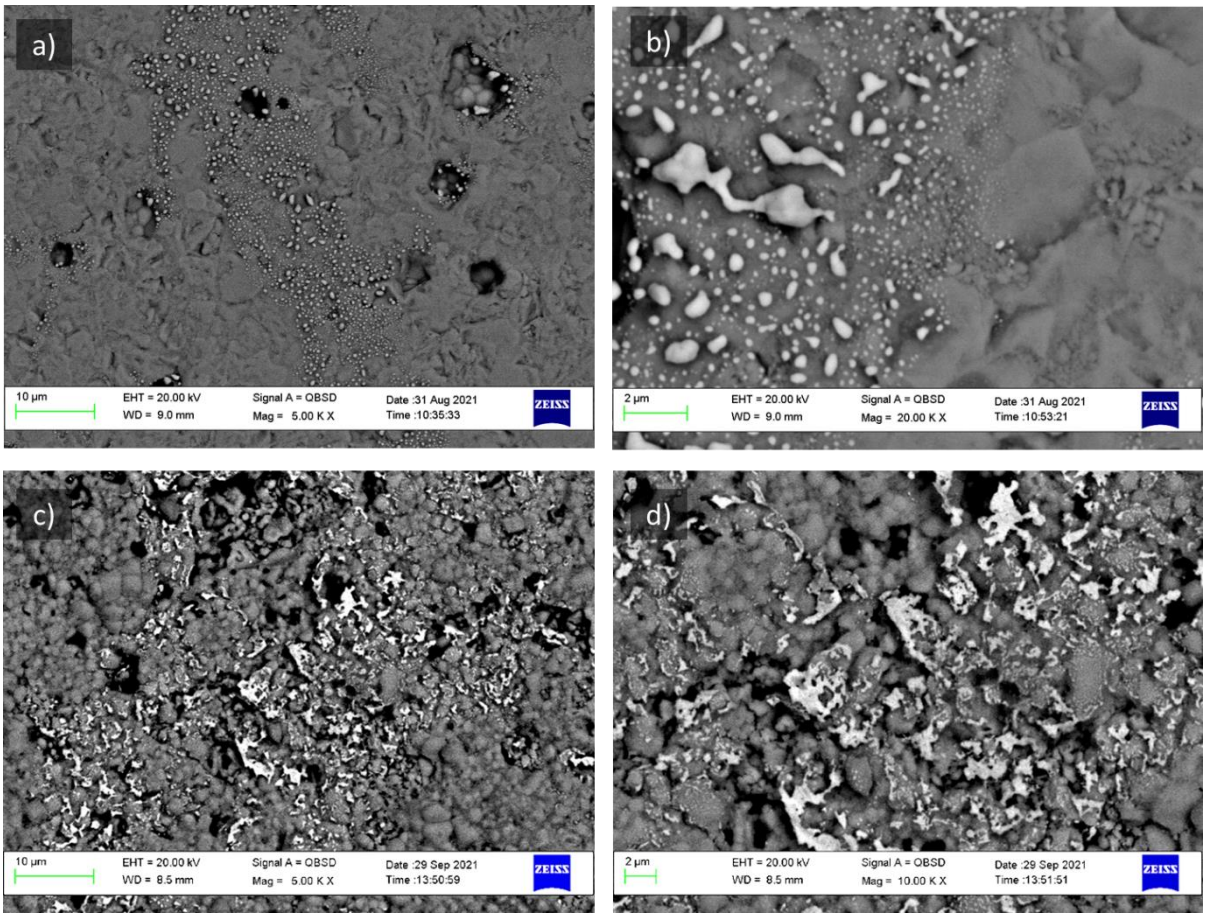

Figure 29 SEM picture of membranes BCZY-GDC-D a), b) and membrane BCZY-GDC-A-1 c), d).

SEM acquisition of Figure 29 are in good agreement with what previously reported in the former section. Particles have overall spheroidal shape, with some degree of difference for membrane BCZY-GDC-A-1 due to reshaping of particle linked to presence of CO and CO_2 gas in the stream, as some following experiments were carried out on the membrane after permeation performances were recorded. Better understanding on the nature of Pt catalyst was attempted by fitting distribution of particle dimension, assuming perfect spherical shape and recording data for approximately 3000 particle per membrane. results are reported hereafter in Figure 30, with associated lognormal distribution fitting.

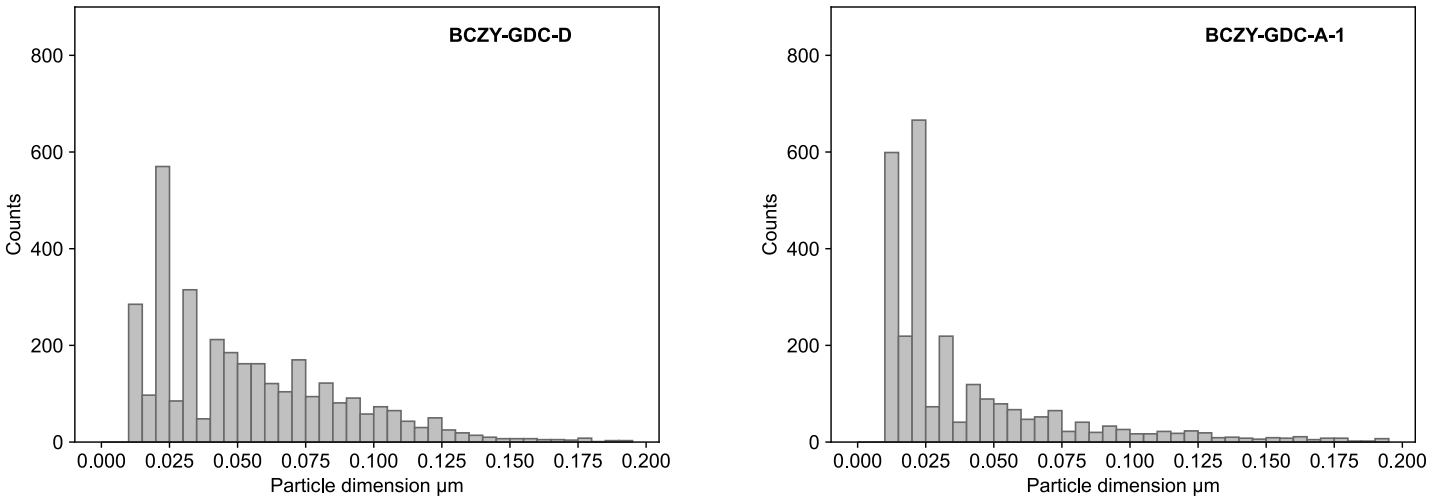

Figure 30 Distribution of Pt particle dimension for membranes BCZY-GDC-D (left) and BCZY-GDC-A-1 (right).

Employing the fitted curves, it was possible to calculate the average weighted value for particle radius, resulting in 0.025 µm for membrane BCZY-GDC-D and 0.035 µm from membrane BCZY-GDC-A-1. From curve parameters is possible to extract the standard deviation of the variable natural logarithm, that results in 0.87 for membrane BCZY-GDC-D and 0.70 for membrane BCZY-GDC-A-1. In summary, the presence of the porous support led to the presence of slightly different particles with more uniform particle radii. This investigation, confirmed to a certain degree, the hypothesis concerning a better dispersion of Pt in a porous network when compared to a flat surface. Overall, dense layer thickness and better Pt dispersion concur positively towards hydrogen permeation performances, favouring membrane BCZY-GDC-A-1.

The investigation, then, focused on the influence of the quantity of Pt on the porous side of the membrane. This was due to the observed enhancement of hydrogen flux at elevated temperatures, attributed to the distribution and quantity of Pt. Asymmetric membranes, which display superior hydrogen permeability, were therefore selected as the suitable choice for examining the concentration of Pt. During the separation experiments, the porous matrix that was put at the permeate side had Pt concentrations that were raised from 0.15 to 1.5 and 4.5 mg cm^{-2} (see Table 10). The WS reaction is believed to have a role in the hydrogen contribution that has permeated on the sweep side of the membrane. Thus, the focus of the investigation was solely on the increase of Pt in that particular area. Further information on sample employed for this investigation are reported in Table 10. Results of permeation performances are reported in the following figure.

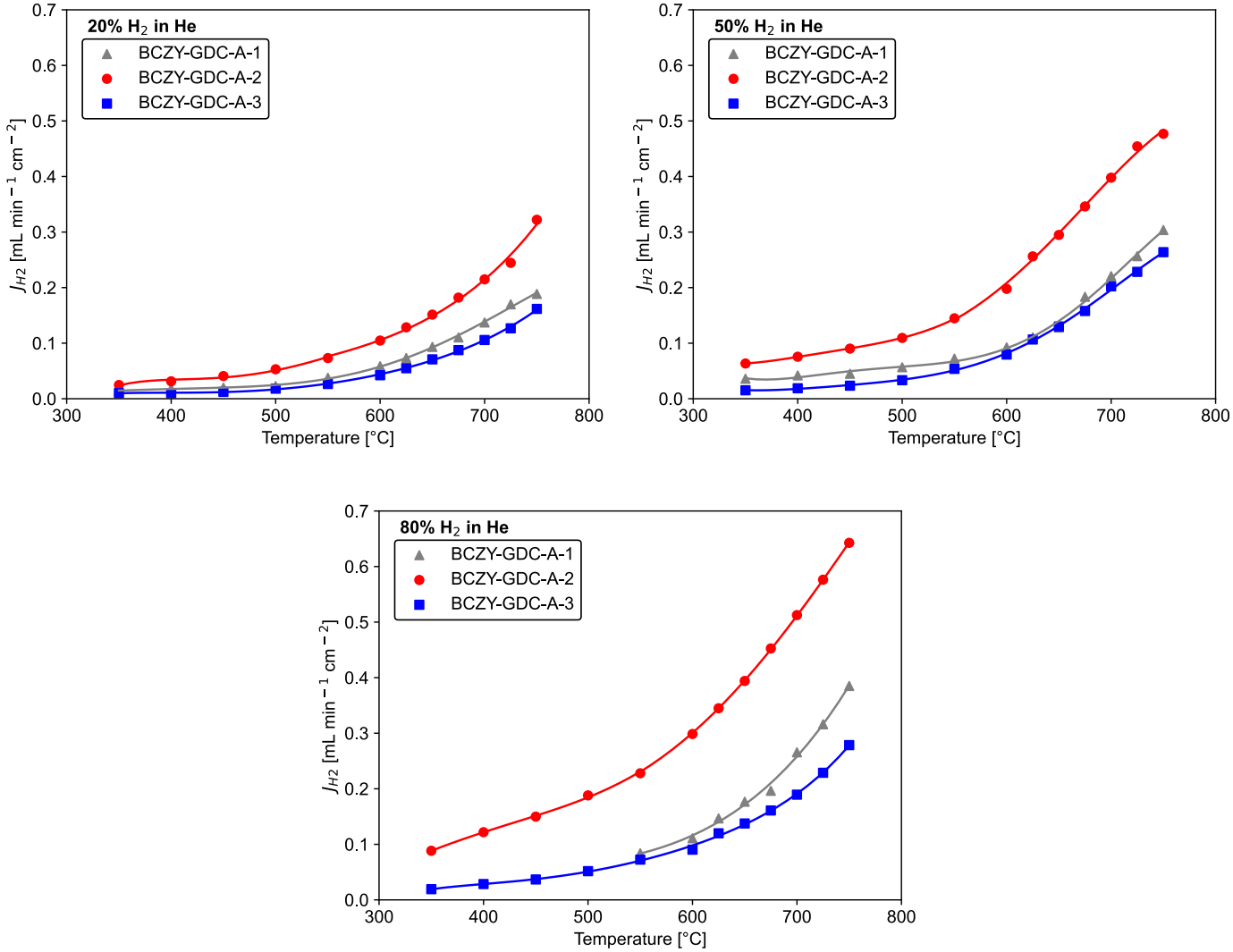

Figure 31 H_2 flow (mL min^{-1} cm^{-2}) of membrane BCZY-GDC-A-1 (grey), BCZY-GDC-A-2 (red) and BCZY-GDC-A-3 (blue) as a function of temperature and feed composition (80%, 50% and 20% H_2 in He, H_2 %vol). Both feed and sweep streams are humidified to saturation at 28 °C.

Figure 31 plots Hydrogen permeation as a function of temperature and feed composition for membranes BCZY-GDC-A-1, BCZY-GDC-A-2 and BCZY-GDC-A-3 which were coated with 0.15, 1.5 and 4.5 mg Pt cm^{-2} respectively. Generally, hydrogen flows, in ceramic dense membranes, are described by Wagner equation, as reported in Eq. 36.

$$J_{H_2} = \frac{1}{4L}\frac{RT}{F^2}\int_{P_{H_2}^{I}}^{P_{H_2}^{II}} \sigma_{tot} t_{H^+}(t_e + t_h) d\ln P_{H_2} \qquad \text{Eq.36}$$

In principle, it can be posited that the BCZY-GDC-A-1, BCZY-GDC-A-2, and BCZY-GDC-A-3 membranes can be regarded as fairly comparable specimens, as their characteristics outlined in Eq. 36 are indistinguishable due to their shared composition, preparation methodology, and data acquisition settings (temperature range, hydrogen partial pressure in feed current, streams mass flow rate). It

is logical to assume that the disparities in overall conductivity and transport numbers among these three samples would be insignificant. Thus, for practical purposes, the sole parameter that was varied for each sample was the quantity of Pt deposited on the porous side of the membrane. One important concept that arises from literature regarding surface modified membranes is that the main role of metal catalyst is relegated to the prevention of adsorption kinetics limitations, most of the times overlooking considerations about morphology and distribution of the catalyst [184]–[186]. In this section the deposition procedure was kept constant for every sample, but the amount of deposited Pt is varied, in order to observe if an effect on permeation performances is present. Observation of Figure 31 gives a clear trend of the data set. In the first instance the effect of temperature is common for all samples, namely an increase in temperature corresponds to an increase in H_2 permeation for all the sample for each of the feed composition. The effect of the composition is also common for the three samples, namely an increase from 20% to 50% and 80% of H_2 in He (%vol) results in an increase of hydrogen permeation (mL min^{-1} cm^{-2}). In Figure 31 the effect of the amount of Pt catalyst is also appreciable. For each temperature and feed composition increasing the amount of Pt from 0.15 mg cm^{-2} to 1.5 mg cm^{-2} shows a net increase of permeation, reaching 0.476 mL min^{-1} cm^{-2}, for membrane BCZY-GDC-A-2, at 750°C with 50% H_2 in He as feed stream composition. Highest permeation value recorded is recorded a 750°C with a composition of 80% of H_2 in He and membrane BCZY-GDC-A-2, reaching 0.642 mL min^{-1} cm^{-2}. It was expected that a further increase of Pt on membrane BCZY-GDC-A-3 would lead to further improvement of H_2 flow but results actually show a slight worsening of permeation performances, reaching 0.263 mL min^{-1} cm^{-2} at 750°C with 50% H_2 in He feed composition. It is possible to see that for each composition and each temperature the hydrogen permeation of membrane BCZY-GDC-A-3 are marginally inferior to the starting sample BCZY-GDC-A-1. In order to better understand results shown in Figure 31 the difference in permeation between BCZY-GDC-A-2, BCZY-GDC-A-3 and BCZY-GDC-A-1 have been calculated and reported in Table 11.

Feed composition (% H_2 in He)	**Temperature (°C)**	**Δ|BCZYGDCA2-BCZYGDCA1| (mL min^{-1} cm^{-2})**	**Δ|BCZYGDCA3-BCZYGDCA1| (mL min^{-1} cm^{-2})**
80	>625	0.248	0.069
	≤625	0.177	0.020
50	>625	0.175	0.023
	≤625	0.069	0.018
20	>625	0.083	0.030
	≤625	0.030	0.010

Table 11 Permeation difference of membrane BCZY-GDC-A-2, BCZY-GDC-A-3 relative to membrane BCZY-GDC-A-1 for different temperature range (T>625°C and T≤625°C) and feed composition ().

Results in the table can grasp a trend linked to water splitting reaction and temperature. It is possible to observe that the results of the calculated value Δ|BCZYGDCA***n***-BCZYGDCA1| tend to be higher at temperature > 625°C for all feed composition and lower at temperature ≤625°C. This is ascribed to the contribute of Pt-catalysed water splitting reaction, that is reported to be more prominent at higher temperature [3], [129], [191], [193], further reinforcing the relevance of the water splitting reaction in hydrogen permeation. The average value Δ|BCZYGDCA2-BCZYGDCA1| at T> 625°C is 0.169 mL min^{-1} cm^{-2} and at T≤ 625°C is 0.091 mL min^{-1} cm^{-2} and for Δ|BCZYGDCA3-BCZYGDCA1| at T> 625°C is 0.040 mL min^{-1} cm^{-2} and at T≤ 625°C is 0.016 mL min^{-1} cm^{-2}. This pattern appears to

indicate that the influence of Pt catalyst on apparent permeation is more pronounced in process involving water splitting and oxygen ion retro-diffusion. It is also worth noticing that the calculated value Δ|BCZYGDCA***n***-BCZYGDCA1| progressively increases when feed composition is enriched in hydrogen, due to increased partial pressure of H_2 gas and consequently increased driving force for proton transport and oxygen ion retro-diffusion and consumption. Further insight on the three membranes behaviour can be acquired observing the percent increase in permeation between hydrogen flow registered at 500°C (where there is reasonably negligible water splitting) and at 750°C. Calculation are carried on results obtained with 50% H_2 in He as a feed stream.

BCZY-GDC-A-1 $\Delta\% = \frac{J_{H_2,750°C} - J_{H_2,500°C}}{J_{H_2,750°C}} = 76\%$

BCZY-GDC-A-2 $\Delta\% = \frac{J_{H_2,750°C} - J_{H_2,500°C}}{J_{H_2,750°C}} = 70\%$

BCZY-GDC-A-3 $\Delta\% = \frac{J_{H_2,750°C} - J_{H_2,500°C}}{J_{H_2,750°C}} = 79\%$

The Δ% values obtained in the current study demonstrate a high level of concordance with the findings reported in previous literature, which are duly noted for the sake of completeness in the present work (Table 12).

Δ%	**Ref.**
77	[184]
27	[186]
76	[187]
54	[187]
51	[190]
63	[190]

Table 12 percent increase in permeation between hydrogen flow registered at low temperature (where there is reasonably negligible water splitting) and at high temperature.

Overall, the value Δ% for the three membrane falls between 70-80% and might indicate the presence of similar processes involved for apparent hydrogen permeation in all the samples, confirming, to a certain extent, membranes homogeneity concerning structure and conductivity properties. The effect of increased deposition of Pt (from 0.15 to 1.5 mg cm^{-2}) affects positively the permeation performances of asymmetric membranes BCZY-GDC produced by Tape Casting. The Pt acts, not only to avoid surface adsorption kinetic limitation, but also as a catalyst for the reaction of WS at high temperature. So far, no significant explanation on why an increase of Pt catalyst from 1.5 to 4.5 mg cm^{-2} would lead to decreased hydrogen permeation performances has been revealed. In order to understand the unexpected behaviour of membrane BCZY-GDC-A-3, then, SEM pictures of membranes surface were acquired, and some illustrative pictures are reported in Figure 32.

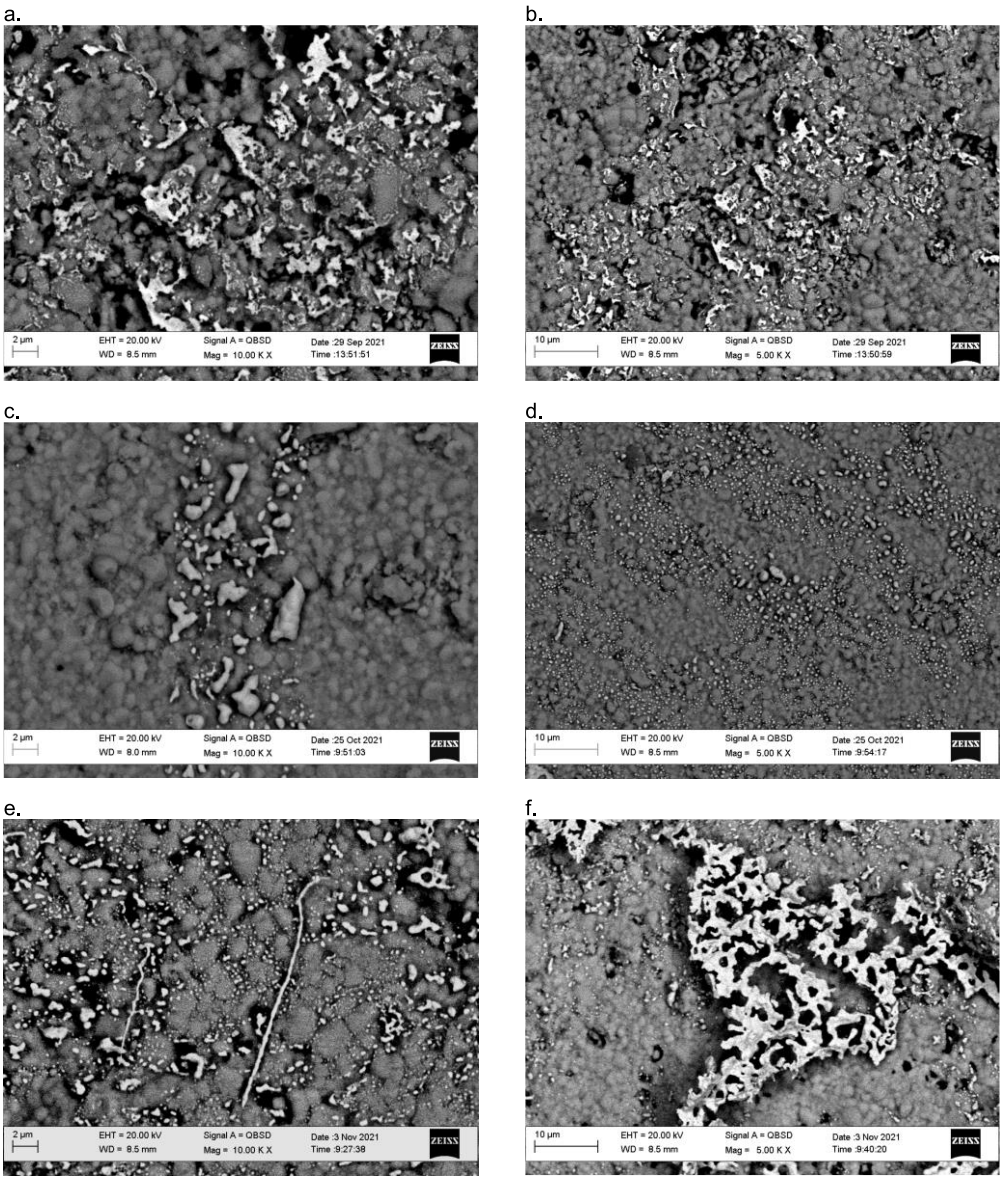

Figure 32 SEM picture of porous side of membranes BCZY-GDC-A-1 (a, b), BCZY-GDC-A-2 (c, d), BCZY-GDC-A-3 (e, f) after permeation measurements.

Figure 32 shows presence of Pt particle on the surface of all membranes, with some degree of difference between the three samples. Overall, the shape of the particles resembles spheres, except for some peculiar cases, that assume irregular structures. This tendency is shared for all samples, with different degree of relevance. To better describe the appearance of Pt particle, an attempt was carried on by fitting distribution of particle dimension, assuming perfect spherical shape and recording data for approximately 3000 particle per membrane. The results are reported in Figure 33.

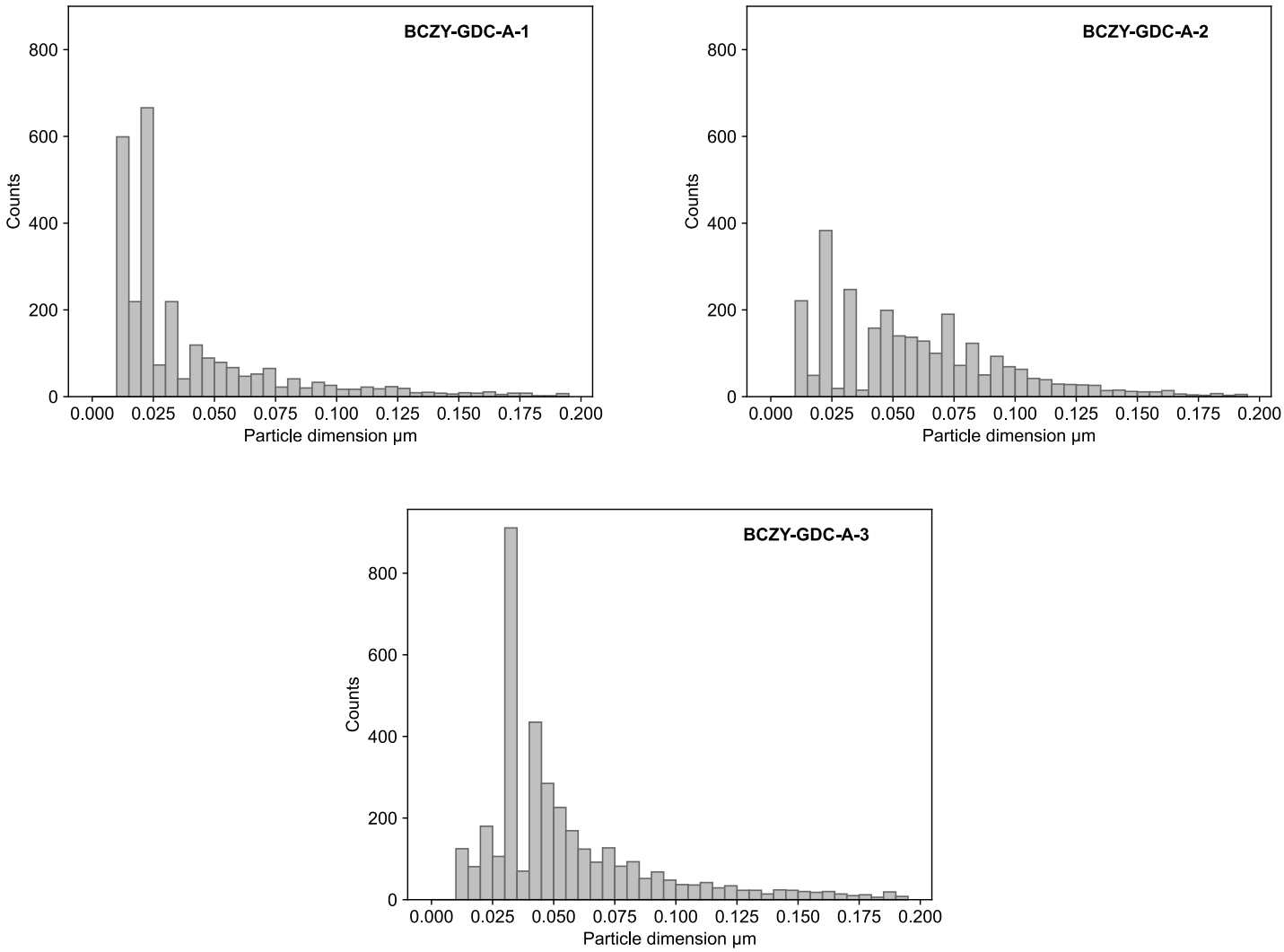

Figure 33 Particle dimension distribution for membrane BCZY-GDC-A1 (left), BCZY-GDC-A-2 (centre), BCZY-GDC-A-3 (right).

Employing fitted curves, it was possible to calculate the weighted average dimension for the three membranes as well as the standard deviation of particle dimension. To facilitate reading, results were reported in the following table.

Membrane	Weighted average (µm)	Standard deviation	Pt amount (mg cm^{-2})
BCZY-GDC-A-1	0.035	0.70	0.15
BCZY-GDC-A-2	0.059	0.60	1.5
BCZY-GDC-A-3	0.050	0.60	4.5

Table 13 Results of distribution fitting for membranes BCZY-GDC-A-1, BCZY-GDC-A-2 and BCZY-GDC-A-3.

Observing Table 13, It is possible to appreciate the effect of the increased concentration of Pt precursor on the particle radius when the deposition method is varied, namely a slight increase in dimensions, not coupled though, with a broadening of the distribution. This might be linked to the increased concentration of the precursor salt in the deposition solution (see Figure 21) [198]. The same hypothesis applies for the explanation of large Pt agglomerate present on membrane BCZY-

GDC-A-3 (Figure 32 e, f), that have not been observed on membranes BCZY-GDC-A-1 and BCZYGDC-A-2 (Figure 32 a, b; c, d). The presence of large agglomerate might be also correlated to the unexpected permeation performances of membrane BCZY-GDC-A-3. For instance, the presence of large agglomerate might lead to large amount of Pt that is not efficiently involved in hydrogen permeation processes, thus resulting in worsened performances. To further characterize Pt particle involved in the membrane porous layer an attempt of distribution fitting on particle locate inside the porosity was attempted employing cross section picture acquired by SEM-FEG technique assuming perfect spherical shape and recording data for approximately 300 particle per membrane. Some representative acquisitions are reported in Figure 34.

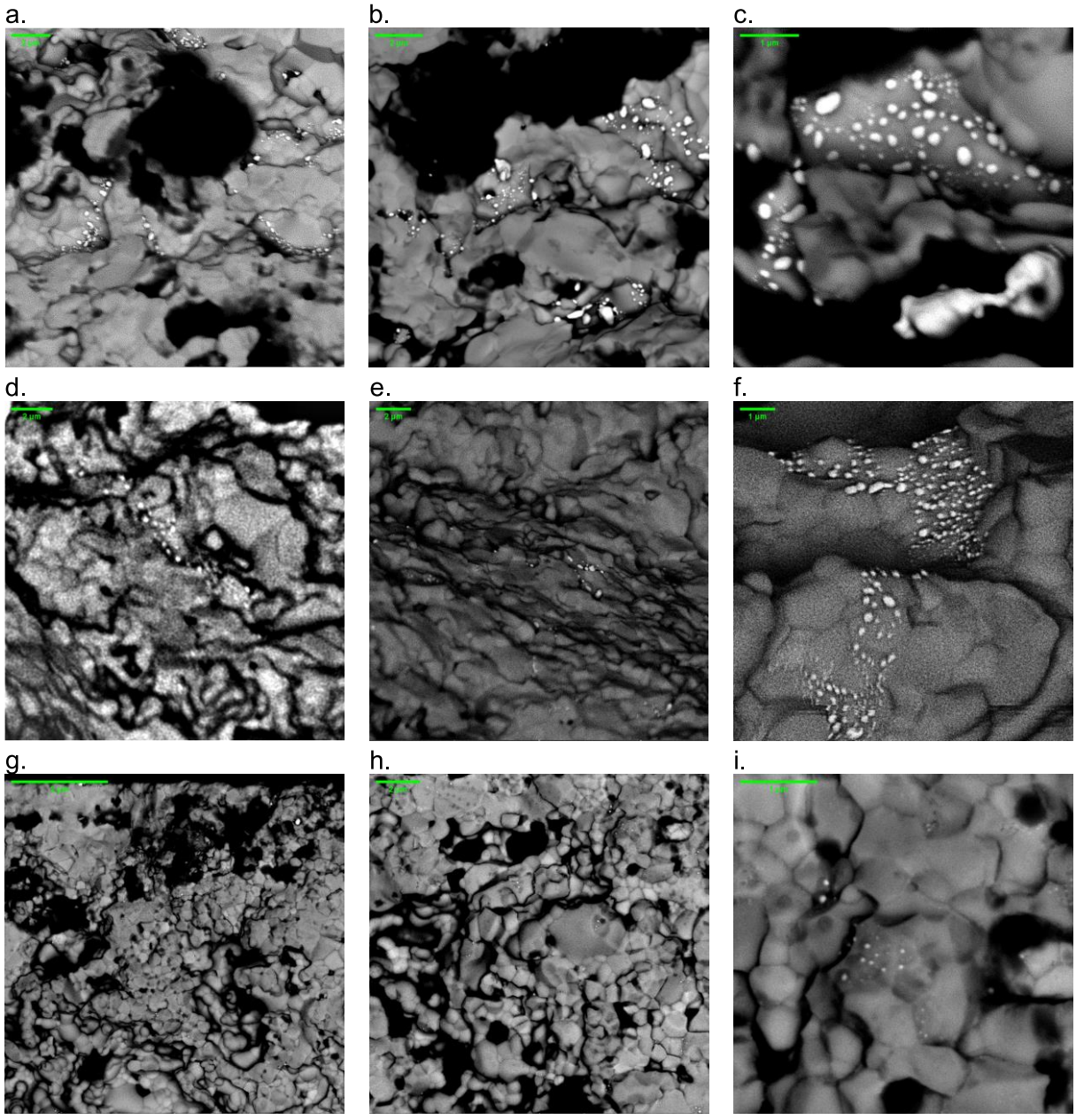

Figure 34 SEM picture of cross section of porous side of membranes BCZY-GDC-A-1 (a, b, c), BCZY-GDC-A-2 (d, e, f), BCZY-GDC-A-3 (g, h, i) after permeation measurements.

As previously shown, particle dimensions were acquired from SEM pictures and reported in Figure 35.

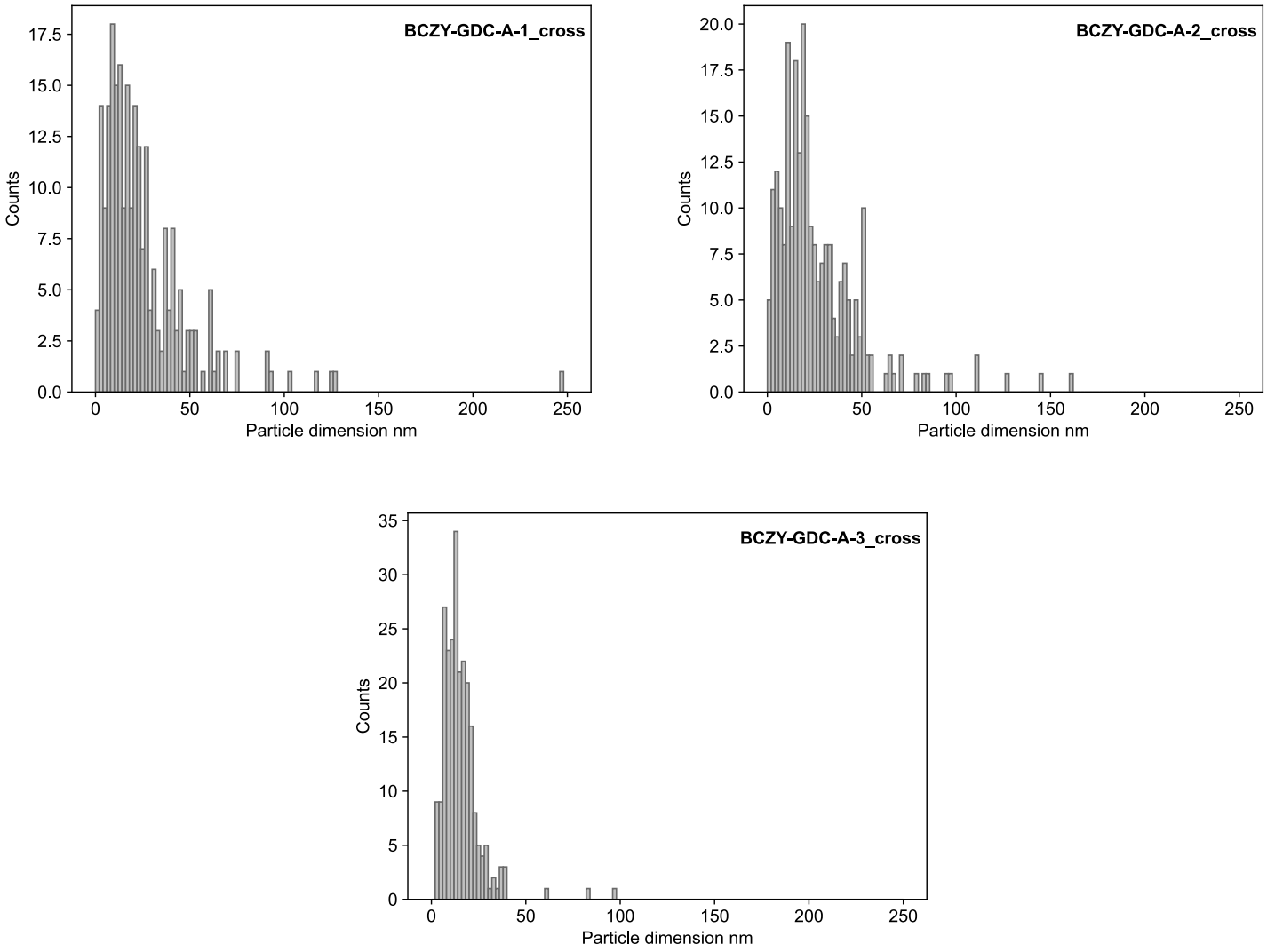

Figure 35 Particle dimension distribution in cross section for membrane BCZY-GDC-A1 (left), BCZY-GDC-A-2 (centre), BCZY-GDC-A-3 (right).

To ease up data evaluation, results of distribution fitting are reported in the following table.

Membrane	Weighted average (µm)	Standard deviation	Pt amount (mg cm^{-2})
BCZY-GDC-A-1	0.017	1.05	0.15
BCZY-GDC-A-2	0.018	0.75	1.5
BCZY-GDC-A-3	0.013	0.6	4.5

Table 14 Results of distribution fitting for cross section of membranes BCZY-GDC-A-1, BCZY-GDC-A-2, BCZY-GDC-A-3.

The evaluation of particles inside the porous layer of three membrane shows comparable results between the samples. It is worth noticing the reduced number of analysed particle due to randomic distribution in tri-dimensional framework, and thus less probable possibility to find particles in a defined section. Weighted particle dimension averaged value stands around 0.02 µm. If compared with surface particles, cross section average is smaller, probably due to hindrance dictated by

porosity of the layer and the increased volume in which happens the precursor deposition. Overall, it can be said that for what concerns cross section deposition, the effect on samples can be considered comparable. In conclusion, it could be stated that employing a drop casting-based deposition methods allowed to better define the amount of Pt catalyst deposited and to obtain dispersed particle on the surface and through the porous layer of the membranes. Nevertheless, high metal catalyst precursor concentration can negatively affect the Pt deposition on the porous layer surface of the membrane, producing some Pt agglomerate that negatively affect the permeation performances, due to decreased or less uniform availability of Pt particles on membrane surface. The overall permeation performance of membranes becomes, then, affected by the distribution of the metal and less by the amount of deposited metal. This is particularly true when permeation is carried on at higher temperatures (≥650 °C) where water splitting rection contribution is prevalent and it is affected by Pt catalyst characteristics.

To further understand the contribution of proton transport and water splitting reaction mediated by oxygen ion transport, the apparent activation energies of the H_2 flow (mL min^{-1} cm^{-2}) were derived and compared with previous research papers. The activation energies of membranes BCZY-GDC-A-1, BCZY-GDC-A-2 and BCZY-GDC-A-3 were calculated under the following experimental conditions: upstream 50% H_2 in He, 80 mL min^{-1}, downstream 100% Ar 150 mL min^{-1}, both current humidified to saturation at 28°C. Experimental data of hydrogen permeation can be employed in a Arrhenius-type equation to calculate activation energy by plotting $\ln(J_{H2})$ against the multiplicative inverse of temperature (expressed in Kelvin), as reported in Eq. 37.

$$J_{H2} = J_0 e^{\left(\frac{-Ea}{RT}\right)} \qquad \text{(Eq. 37)}$$

Results for the Arrhenius plots reported in Figure 36.

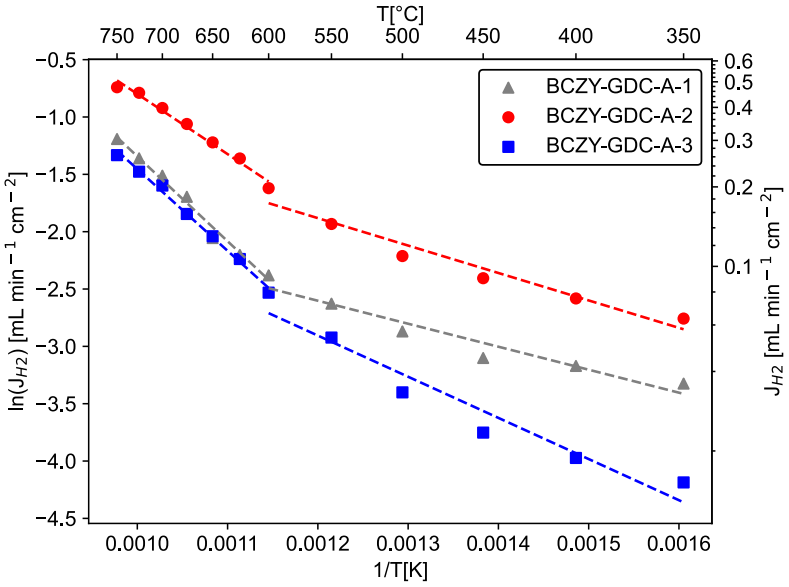

Figure 36 Arrhenius plot of permeation performances (mL min^{-1} cm^{-2}) for membranes BCZY-GDC-A-1, BCZY-GDC-A-2 and BCZY-GDC-A-3 with feed composition of 50% H_2 in He, H_2 %vol. Both feed and sweep streams are humidified to saturation at 28 °C.

A linear fitting has been employed to calculate apparent activation energies for the three membranes. The temperature ranges (T< 600°C and T> 600°C) have been selected according to what previously used in literature [3], [129]. Results are reported in the following table.

Membrane	Temperature (°C)	Activation Energy (eV)
BCZY-GDC-A-1	<600	0.173
	>600	0.640
BCZY-GDC_A-2	<600	0.207
	>600	0.454
BCZY-GDC_A-3	<600	0.310
	>600	0.616

Table 15 Activation energy for Membrane BCZY-GDC-A-1, BCZY-GDC_A2 and BCZY-GDC-A-3 obtained with 50% H_2 in He and humidified streams.

Data shown in Table 15 report a definite trend. Apparent activation energies measured at lower temperature (T< 600°C) for all the three membrane results in a smaller value if compared with the high temperature counterpart (0.21 eV, 0.25 eV and 0.36 eV for membranes BCZY-GDC-A-1, BCZY-GDC-A-2, BCZY-GDC-A-3) due to prevalent proton transport, while activation energy measure at higher temperature (T> 600°C) are related to the prevalent water splitting reaction and retro-diffusion of oxygen ion, as previously reported in literature [3], [129], and results in higher values (0.667 eV, 0.414 eV and 0.589 eV for membranes BCZY-GDC-A-1, BCZY-GDC-A-2, BCZY-GDC-A-3 respectively). It is worth reporting that the activation energy measurement should describe the factual proton transport energy barrier thanks to the presence of Pt catalyst that avoids surface adsorption kinetics limitations. At higher temperatures (T > 600°C) the reaction of WS becomes increasingly more dominant, thus the measured energy barrier refers predominantly to the reaction of water splitting and retro-oxygen ion transport [3], [129]. When it comes to apparent activation energies at T<600°C. Results are comparable with those of other dense ceramic membranes present in literature (Table 16).

System	Architecture	Configuration	Activation Energy (eV) low T	Activation Energy (eV) high T	Ref
Mbr0.85 - $BaCe_{0.65}Zr_{0.20}Y_{0.15}O_{3-\delta}$ (BCZY)–$Gd_{0.2}Ce_{0.8}O_{2-\delta}$ (GDC)	Disk	Dual-phase – asymmetric	0.24	0.54	[192]
Mbr2.00 - $BaCe_{0.65}Zr_{0.20}Y_{0.15}O_{3-\delta}$ (BCZY)–$Gd_{0.2}Ce_{0.8}O_{2-\delta}$ (GDC)	Disk	Dual-phase – asymmetric	0.20	0.35	[192]
$SrCe_{0.7}Zr_{0.2}Eu_{0.1}O_{3-\delta}$ – NiO–$SrCe_{0.8}Zr_{0.2}O_{3-\delta}$	tubular	Single-phase – asymmetric	not reported	0.84	[199]
$Sr(Ce_{0.6}Zr_{0.4})_{0.85}Y_{0.15}O_{3-\delta}$ (SCZY)–SCZY-NiO	Disk	Single-phase – asymmetric	0.32	0.50	[178]
$BaCe_{0.65}Zr_{0.2}Y_{0.15}O_{3-\delta}$ (BCZ20Y15) –$Ce_{0.85}Gd_{0.15}O_{2-\delta}$ (GDC15)	Disk	Dual-phase – asymmetric	0.82	1.04	[129]
$SrCe_{0.95}Tm_{0.05}O_{3-\delta}$ (SCTm) – SCTm	Disk	Single-phase – asymmetric	1.35	0.182	[176]
$SrCe_{0.95}Y_{0.05}O_{3-\delta}$ (SCY) – SCY	Disk	Single-phase – asymmetric	not reported	1.11	[200]
$La_{0.5}Ce_{0.5}O_{2-\delta}$ (LDC) – LDC	disk	Single-phase – asymmetric	not reported	1.219	[201]

Table 16 Reported apparent activation energies from published literature papers.

Low temperature activation energies of membrane BCZY-GDC-A-1 and BCZY-GDC-A-2 (0.173 and 0.207 eV respectively) are reasonably similar, while membrane BCZY-GDC-A-3 result in a slightly increased value (0.310 eV). On the contrary, when high temperature activation energies are confronted membrane BCZY-GDC-A-2 shows a smaller value (0.414 eV) when compared with membranes BCZY-GDC-A-1 and BCZY-GDC-A-3 (0.640 and 0.616 eV respectively). The differences in activation energies for a specific molecule (in this case H_2) are generally related to the capacity of a membrane to separate said molecule with enhanced and faster separation [202].

Finally, the composition of the membranes was validated using X-Ray diffraction analysis (XRD) to ensure phase preservation following permeation tests. Results are reported in Figure 37. Analysis were carried on both sides of the membranes after permeation measurements and are both reported in Figure 37.

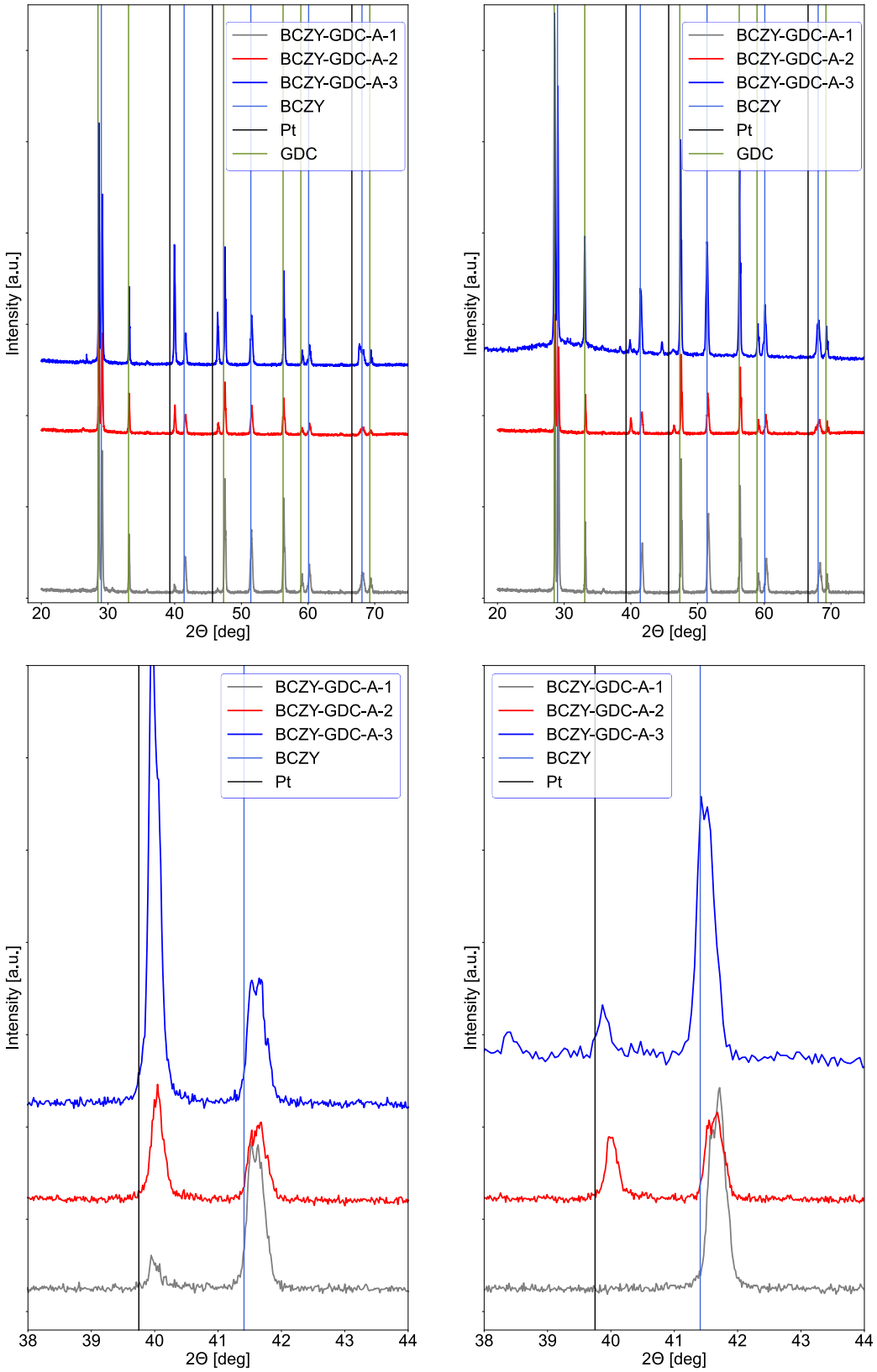

Figure 37 XRD analysis results for membranes BCZY-GDC-A-1, BCZY-GDC-A-2, BCZY-GDC-A-3 (porous side on the left, dense side on the right). Pattern for the different ceramic phases are reported[191]. Reference patterns for Pt and Cu metal are also reported. Zoom of region 2ϑ=[35:45] is reported under complete XRD survey.

Both the oxide phases, BCZY and GDC, can be detected on the two sides of the membranes. It is noteworthy that the presence of Platinum (Pt) is also evident on all samples and on both sides of each membrane. The relative intensities of Pt reflexes are found to be increasing with the theoretical deposited catalyst amount for Pt effect investigations on permeation performances. It should also be noted that a slight right shift of XRD reflexes is observed in all samples when compared with reference patterns. This is due to the Philips PW1050/81 diffractometer available sample holder. This was not particularly suitable for membrane and did not allow the operator to set personalised alignment of the sample. This led to data shifting due to departure from the calibrated position of the sample. Lastly, it is worth mentioning that the broadening of Pt reflex in the diffraction patterns was employed to calculate the size of Platinum crystallites, using Scherrer equation:

$$B = \frac{0.9\,\lambda}{t\cos\theta} \tag{38}$$

where B is the full width at half maximum (FWHM) of the expanded diffraction line on the scale (radians) and t is the crystallites' diameter. Results are reporter in the following table:

Membrane	Pt crystallite Size (nm) porous side	Pt crystallite size (nm) dense side
BCZY-GDC-A-1	44.3	-
BCZY-GDC-A-2	49.8	48.5
BCZY-GDC-A-3	70.5	59.7

Table 17 Platinum crystallite size measurement, from XRD analysis of membranes BCZY-GDC-A-1, BCZY-GDC-A-2, BCZY-GDC-A-3.

From Table 17 it is possible to observe that for what concerns the crystallite size on the dense side, dimensions are quite similar, although, because of penetration of X-Ray, it is impossible to discard the hypothesis of porous Pt particle contribution, thus determination of Pt peaks in membrane BCZY-GDC-A-1 on dense side results difficult. Anyhow, the determination gets progressively easier when the amount of Pt on the porous side increases. This also explains why crystallite size on the dense size increases in membrane BCZY-GDC-A-3. As just said, the contribution of particles on the porous side might affect the average dimension of crystallites. When porous side is confronted, Pt crystallites are found to be bigger in membrane BCZY-GDC-A-3, as was previously seen from SEM pictures (Figure 32). The correlation between crystallite and particles dimensions could be complex and dependent from various factors [203]. High amount of Pt precursor may lead to the formation of bigger crystallites that then would proceed to agglomerate, forming bigger particle of Pt composed of several crystallites.

Additionally, information on Pt active surface area could definitely help with the discussion of results of permeability. One possible approach could involve CO chemisorption experiments, employing spent membranes. The experiment should be carried out with CO as adsorbate gas in order to avoid spillover effect on ceramic support and characterize only Pt active surface area[233]. In literature, the commonly used adsorbate gas are N_2, CO and O_2. Due to the nature of the membrane, H_2 and O_2 could have competing adsorption between Pt and membrane oxide, thus the choice falls on carbon monoxide[233], [234]. Sadly, at the time of production of this elaborate the optimization procedure for the chemisorption analysis revealed itself challenging and no significant results were obtained with available membrane samples. It is worth reporting that for future experiments

information on Pt active surface area should be reported and employed for the interpretation of data.

4.9 Tape casting membranes - conclusions

The hydrogen permeability of asymmetric Cer-Cer composite planar membranes comprising $BaCe_{0.65}Zr_{0.20}Y_{0.15}O_{3-\delta}$(BCZY) – $Gd_{0.2}Ce_{0.8}O_{2-\delta}$ (GDC) composition was investigated in terms of temperature, feed side composition and catalyst amount using humidified streams, saturated at 28°C. To this end, three feed compositions, namely 20%, 50% and 80% H_2 in He (H_2 %vol), were examined within the temperature range of 350 °C to 750 °C. In particular, the dense side of the membranes was charged with 0.15 mg cm^{-2} of Pt, while 3 distinct amounts of Pt were probed to enhance the water splitting reaction on the sweep side, namely 0.15, 1.5 and 4.5 mg cm^{-2}. The reason behind this mismatch in Pt amount is linked to the contribution of permeated hydrogen. The most optimal performance was attained when 1.5 mg cm^{-2} of Pt was deposited on the porous layer, resulting in a 0.642 mL $min^{-1}cm^{-2}$ flux when 80% H_2 in He was employed as the feed. Pt deposition method is influenced by the concentration of the Pt precursor, that results in different morphology of the catalyst. In particular, high precursor concentration causes formation of Pt agglomerates, that in the end cause less effective Pt catalyst particles for WS reaction at high temperatures.

The presence of agglomerated particle is to be ascribed to the so-called “coffee ring effect”, result of the drop casting method for Pt deposition. When sessile droplets containing suspended particles evaporate under ambient circumstances, they frequently produce a ring-like pattern that is macroscopic in size and discernible by eye after drying. Deegan *et al.* [204] observed, highlighted, and interpreted this phenomenon in coffee stains, where the periphery of the ring was seen to be concentrated with non-volatile solute particles in contrast to the centre of the stain: this phenomenon has been dubbed the "coffee ring effect" (CRE). The physical prerequisites for observing a ring pattern stem from surface tension forces 'pinning' the contact line at the droplet's edge. Contact line pinning prevents any further spreading of the solvent, and a radial outward capillary flow of the solvent from the centre towards the contact line is observed, driven by evaporation because evaporation is greatest at the edge of the drop, which is more 'ventilated' than the centre [205]. This is owing to the increased free space near the droplet's edge, which causes more solvent molecules to evaporate than in the middle. Because the evaporation flow at the perimeter of the droplet is larger than at the core, there is more solvent loss along the contact line. A flow of solvent from the centre, coupled with non-volatile solute particles, compensates for the loss. As a result, the rate of local evaporation is a primary factor determining the solution's radial outward flow. The size of the evaporation flux is determined by the radius of the droplet $\boldsymbol{r}$, the height of the droplet $\boldsymbol{h}$ above the centre, and the contact angle $\boldsymbol{\vartheta r}$ with the velocity of the particles, which reflects the spatial heterogeneity of the evaporative flux [198].

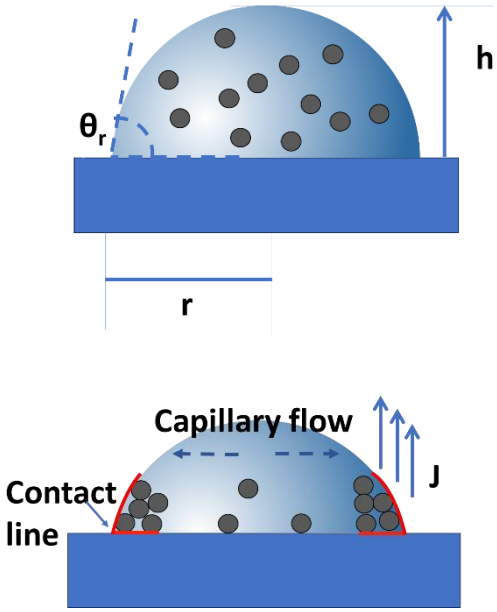

Figure 38 A diagram illustrating (up) a droplet with particles on a solid substrate and (down) capillary flow from the centre to the edge while maintaining the contact line stationary during evaporation. Capillary flow causes particles in the droplet to travel to the edge. h = droplet height; Θr = contact angle; r = droplet radius; J = evaporation flow [adapt.][198].

Remarkably, this study revealed that the metallic catalyst, which is typically employed in the literature to circumvent surface kinetic limitations, is directly implicated in the permeation performance of membranes. Furthermore, additional improvements could potentially augment permeation results and offer a promising avenue towards technological advancement.

4.10 Deposition solvent modification.

In the preceding section, it was noted that the presence of Pt catalyst on the sweep side had a positive impact. To gain a comprehensive understanding of the efficacy of the Pt catalyst quantity implicated in the permeation performances, calculations of H_2 flows have been plotted, taking into account the apparent permeated flow ratio per amount of Pt catalyst (mL $min^{-1}cm^{-2}mg^{-1}$). The ensuing outcomes are expounded in detail in the following sections.

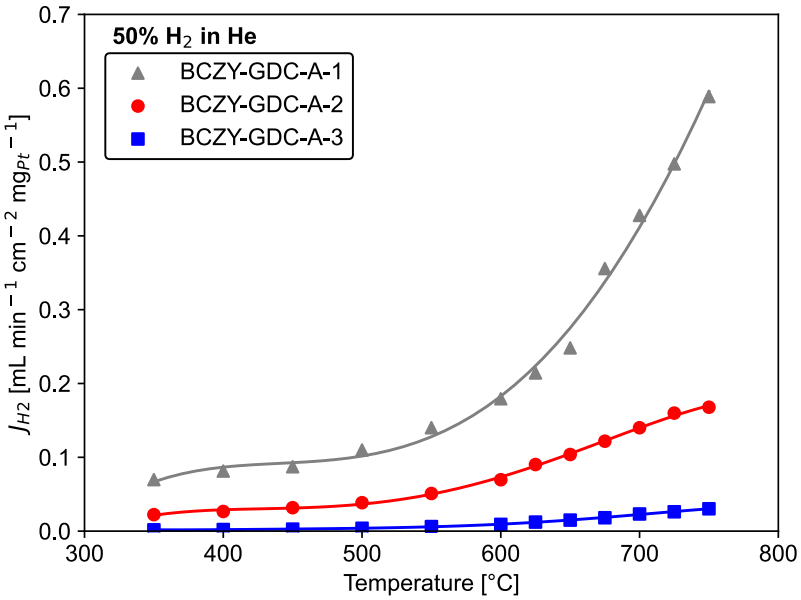

Figure 39 Hydrogen flow per mg of Pt as a function of temperature for membranes BCZY-GDC-A-1, BCZY-GDC-A-2, BCZY-GDC-A-3 with a feed composition of 50% H_2 in He (H_2 %vol). Both feed and sweep streams are humidified to saturation at 28 °C.

From Figure 39 there's a clear comprehension of the reducing effectiveness of Pt catalyst. If Figure 31 and Figure 39 are confronted it appears that an increased amount of Pt, in particular from 0.15 mg cm^{-2} (membrane BCZY-GDC-A-1) to 1.5 mg cm^{-2} (BCZY-GDC-A-2), results in an increased hydrogen permeation performance, at the expenses of Pt catalyst effectiveness. From previous results it was observed the presence of agglomerated particles linked to increased concentration of Pt precursor in the drop casting deposition solvent. It was deemed interesting investigating if a better suitable solvent would effectively increase Pt dispersion and improve morphology of particle.

The previously cited coffee-ring phenomena necessitates not only a pinned contact line, particles that stick to the substrate, and a high evaporation rate towards the droplet's edge, but also the suppression of the convective flow inside the droplets (Marangoni effect) caused by latent heat of evaporation [206]. Some methods to suppress CRE have been reported but are characterized by impracticality for membrane separation purposes [198], [207]–[209]. The most practical strategy to take is to utilise and empirically investigate a range of various solvents in conjunction with microscopic imaging of surfaces in order to find an appropriate solvent in which Marangoni effects best reduce coffee ring effects [210], [211]. A prior investigation concerning the right solvent mixture was carried out observing the contact angle of different solutions on top of polished dense pellets. The contact angle is an indicator of the affinity between fluid and the solid medium [212]. The employment of lower contact angles, which reflects the spatial heterogeneity of the evaporative flux [198], could improve the distribution of Pt catalyst particles, suppressing the CRE in the first place. Results of measurement are reported below (Table 18).

phase	Contact angle (°)					
	Water	Methanol	Methanol/Water	Acetone	Acetone/Water	n-Hexadecane
GDC20	95.59 ± 2.99	24.7 ± 3.36	59.55 ± 0.27	20.96 ± 2.08	67.26 ± 3.34	20.68 ± 4.51
BCZY	96.20 ± 3.06	30.2 ± 3.6	65.63 ± 3.13	30.1 ± 5.57	67.01 ± 2.1	8.51 ± 1.74
BCZY-GDC	95.28 ± 3.76	25.8 ± 4.26	60.92 ± 2.62	21.88 ± 2.41	66.79 ± 2.68	17.81 ± 5.37

Table 18 Contact angle measurements on dense pellets of ceramic phases GDC, BCZY-GDC and BCZY with different solutions.

To better understand the interactions of solvent with the membrane the following figure (Figure 40) is reported, which report solvent properties [213], [214] coupled with measured contact angles.

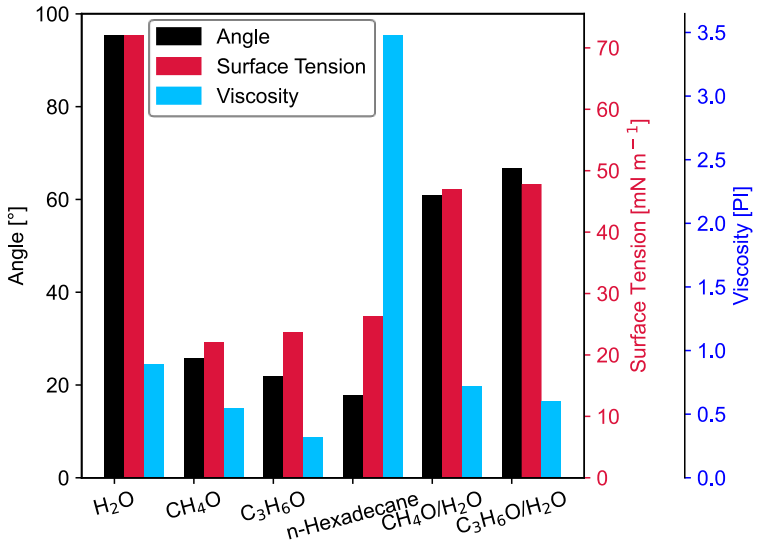

Figure 40 Solvent properties and measured contact angle.

In this elaborate the aforementioned approach led to the employment of a different solvent mixture, shifting from 100% H_2O, previously used, to a mixture of 50% H_2O in Acetone (%vol), due to solubility limits of metal precursor and after careful consideration of data reported in Figure 40. Ideally, following what stated in 4.9 Tape Casting membranes – conclusions, the best suitable solvent candidate would present small contact angle and lower viscosity. Due to solubility limits of Pt precursor employment of solvent mixture with water was deemed necessary. Acetone-Water and Methanol-Water presented almost similar properties, but the lower viscosity of the mixture Acetone-Water coupled with the large solubility span of the metal precursor determined this as the most promising initial candidate. Nevertheless, further investigation with different ratio and also Methanol-Water mixture should be taken into consideration for future works.

To understand the effect of the new deposition method a membrane produced by tape casting shaping method was investigated. In Table 19 it is possible to observe necessary information on the membrane considered in this section.

Membrane	Type	Thickness (um)	Diameter(mm)	Deposition, solvent	Additional Info
BCZY-GDC-A-ace	asymm.	640	15	A 0,15 mg cm^{-2}, H_2O B 1,5 mg cm^{-2}, H_2O/ace	Side A dense Side B porous
BCZY-GDC-A-2	asymm.	780	14,81	A 0,15 mg cm^{-2}, H_2O B 1,5 mg cm^{-2}, H_2O	Side A dense Side B porous

Table 19 Structural information on different membrane and catalyst deposition. ace = Acetone

Membrane BCZY-GDC-ace hydrogen permeation performances have been thoroughly investigated, observing H_2 flows (mL $min^{-1}cm^{-2}$) as a function of temperature and hydrogen partial pressure in the feed stream. Results of membrane BCZY-GDC-ace performances are reported in Figure 41.

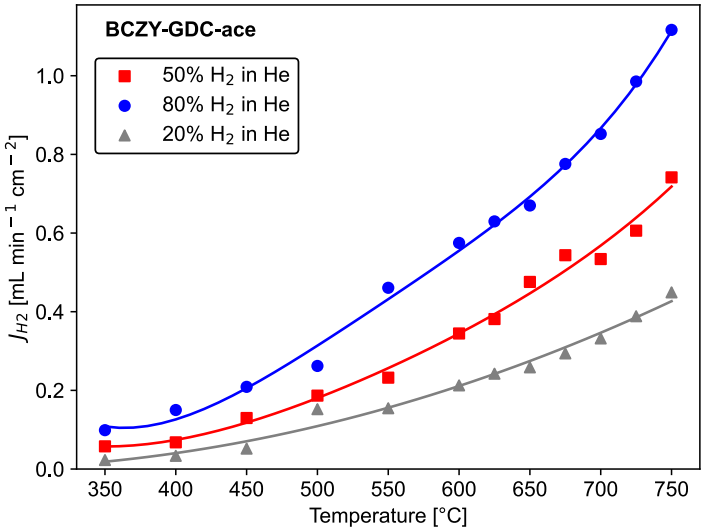

Figure 41 H_2 flows (mL min^{-1} cm^{-2}) of membrane BCZY-GDC-ace as a function of temperature and feed stream composition (80%, 50% and 20% H_2 in He, H_2 %vol). Both feed and sweep streams are humidified to saturation at 28 °C.

From Figure 41 it is possible to appreciate membrane BCZY-GDC-ace behaviour when related to temperature and feed stream variations. With each permeation curve, a rise in temperature yields a proportional increase in hydrogen apparent permeation, in accordance with the expectations derived from Wagner equation (Eq. 36). As for the feed composition, transitioning from 20% to 50% and 80% H_2 in He (H_2 %vol) leads to a boost in apparent hydrogen permeation. The comprehensive behaviour of the BCZY-GDC-ace membrane's permeation is in alignment with the findings of prior studies on other membranes that were produced by the tape casting porosity shaping method. At 750°C with 50% H_2 in He (%vol) membrane BCZY-GDC-ace presented 0.74 mL $min^{-1}cm^{-2}$ as hydrogen flow with both current humidified at 28°C.

In principle, the same conditions were employed for testing membrane BCZY-GDC-ace and the series BCZY-GDC-A-1, BCZY-GDC-A-2, BCZY-GDC-A-3. These membranes can be reasonably considered comparable and thus, the only effect on apparent hydrogen permeation could be practically linked to the modification of the Pt catalyst. Platinum deposition was investigated by altering the drop casting solvent while maintaining the same quantity of metal per membrane surface, respectively to dense and porous side surface. Membrane BCZY-GDC-A-2 has the same amount of Pt deposited on the membrane, respectively 0.15 mg cm^{-2} for dese side and 1.5 mg cm^{-2} for porous side. To

further understand the influence of the deposition solvent, the results of comparation of permeation measurements are provided in the figure below (Figure 42).

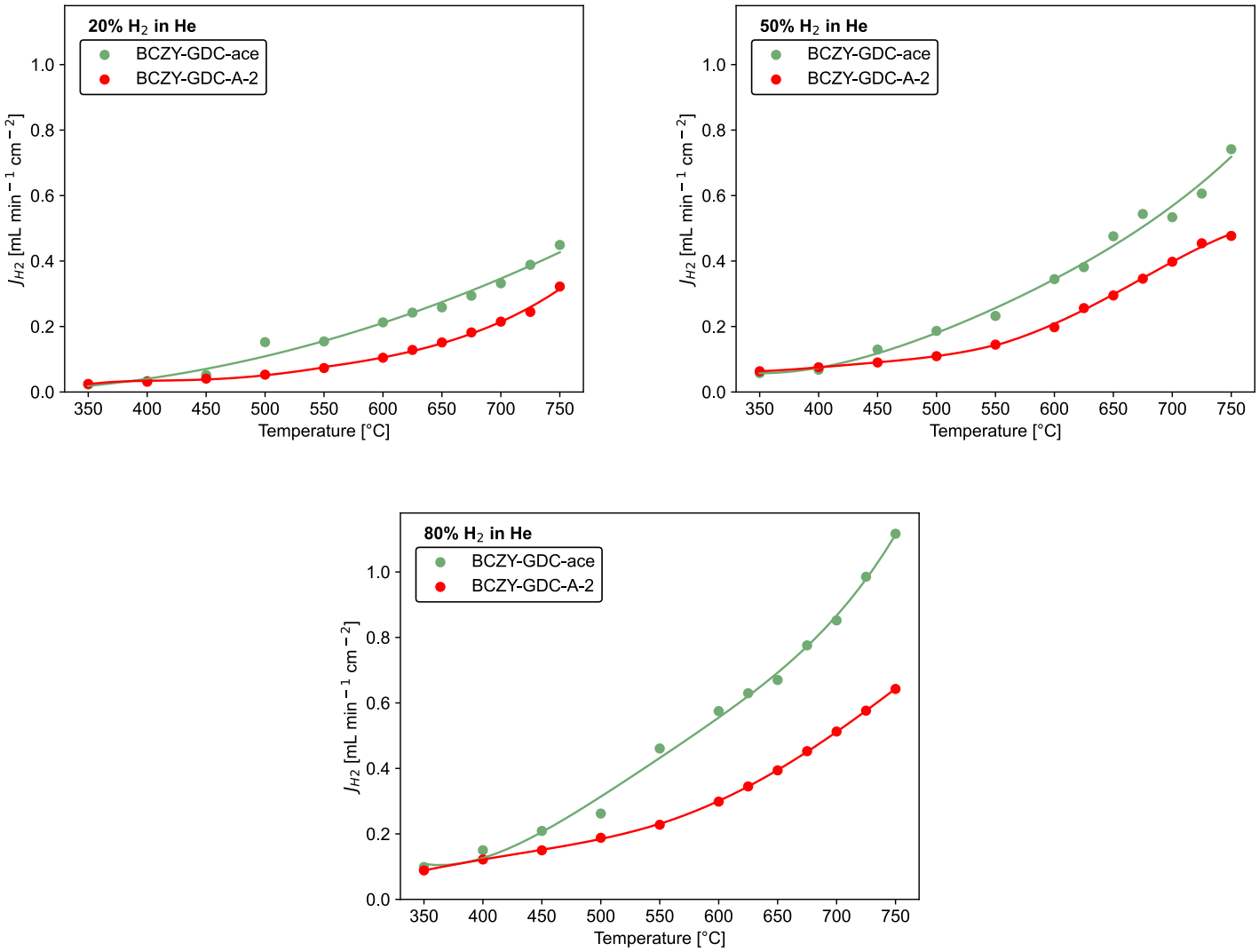

Figure 42 H_2 flow (mL min^{-1} cm^{-2}) of membrane BCZY-GDC-A-2 (red) and BCZY-GDC-A-ace (green) as a function of temperature and feed composition (80%, 50% and 20% H_2 in He, H_2 %vol). Both feed and sweep streams are humidified to saturation at 28 °C.

Figure 42 plots apparent hydrogen permeation (mL min^{-1} cm^{-2}) as a function of temperature and feed stream composition (80%, 50% and 20% H_2 in He, H_2 %vol). The main remark highlighted from Figure 42 is the increased H_2 flow observed in membrane BCZY-GDC-ace, especially at higher temperature. There is no appreciable difference in H_2 flow at temperatures below 450°C. The reason lies, again, within the hydrogen permeation mechanism (Figure 12). To better visualize this concept the value ΔJ_{H2} was calculated as follows:

$$\Delta J_{H2} = \frac{J_{H2,T=i,H2\%,BCZY-GDC-ace} - J_{H2,T=i,BCZY-GDC-A-2}}{avg(J_{H2,BCZY-GDC-A-2})}$$

And was calculated for each temperature and plotted in the following figure.

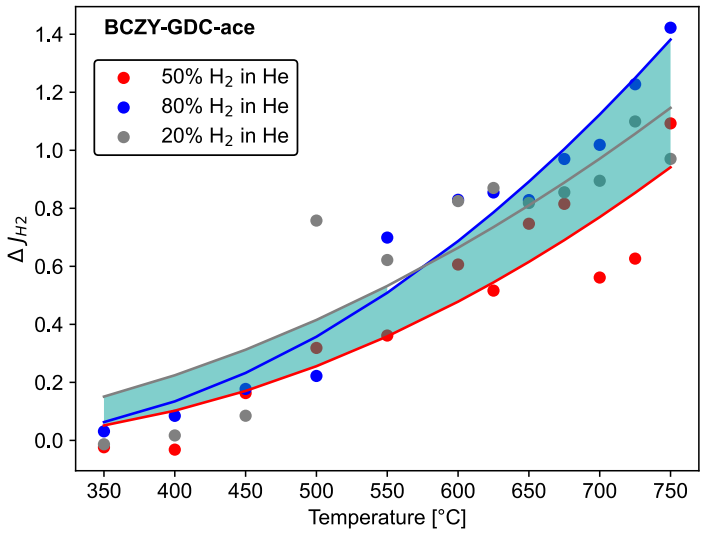

Figure 43 Relative flow difference between membranes BCZY-GDC-ace and BCZY-GDC-A-2, as a function of temperature and feed stream composition (80%, 50% and 20% H_2 in He, H_2 %vol). For clarity, range between points have been highlighted in light blue.

It is possible to appreciate (Figure 43) the increasing ΔJ_{H2} value when temperature increases, and this is true for each feed stream composition curve. This trend is ascribed once again to the different permeation process contribution, linked to Pt catalyst role. When temperature is low (T< 600°C) main contribution is proton transport, while when permeation measurements are conducted at high temperature (T> 600°C), the effect linked to Pt catalyst morphology becomes increasingly relevant, and thus the value ΔJ_{H2} grows steadily. When different composition curves are confronted, it is possible to observe that curves for 20% and 80% H_2 in He (H_2 %vol) have consistently similar ΔJ_{H2} values, while curve for 50% H_2 in He (H_2 %vol) has slightly smaller ΔJ_{H2} that remains similar for each temperature. This might be ascribed to expectable analysis fluctuations. Once again results tend to point to morphological and structural properties of Pt catalyst as relevant features involved in ceramic membranes separation processes.

SEM-EDS characterization of membrane BCZY-GDC-ace was carried out after permeation measurement and is reported hereafter.

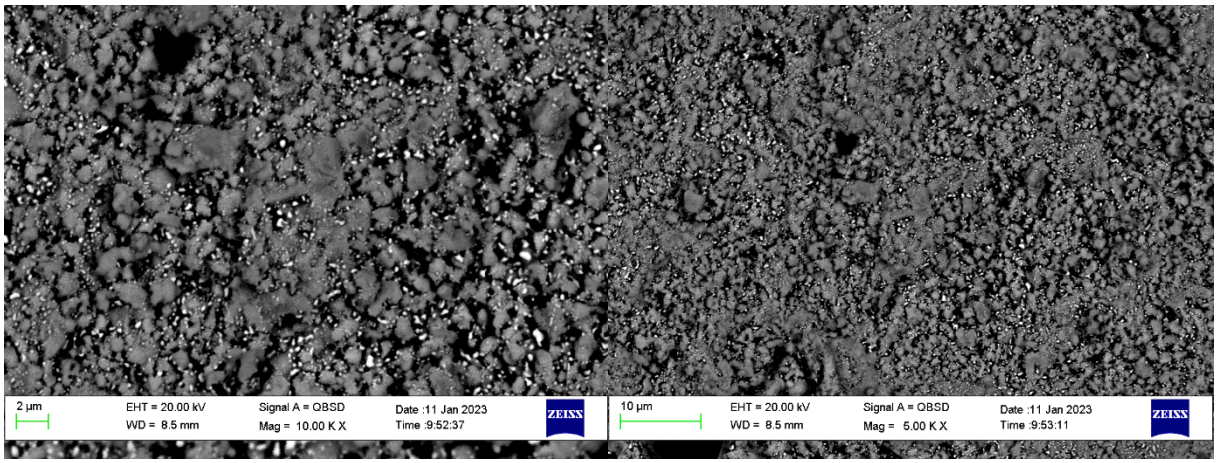

Figure 44 SEM picture of top surface of porous layer of membrane BCZY-GDC-ace

Figure 44 shows a typical appearance of a membrane produced by Tape Casting porosity shaping method, with no unusual features, if confronted with previous membrane BCZY-GDC-A-2 (Figure 32). Dimensions of Pt particles acquired from SEM picture is reported hereafter. Coherent magnification, scale and acquisition method has been employed, in order to correctly confront membrane BCZY-GDC-A and BCZY-GDC-ace. It is worth reporting that particle dimensions got from SEM acquisition is not comprehensive of whole surface and coupling with other analysis methods might led to more reliable results.

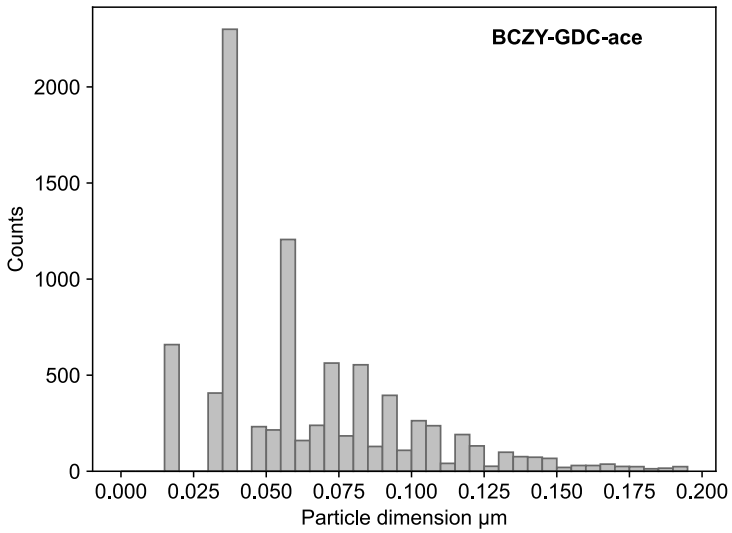

Figure 45 particle dimension of porous surface layer of membrane BCZY-GDC-ace.

Once again particle dimension results are similar to what previously observed with the same characterization on membranes BCZY-GDC-A-1, BCZY-GDC-A-2 and BCZY-GDC-A-3. It is worth reporting, though, absence of Pt agglomerate on top surface, that characterized the border section of membrane BCZY-GDC-A-3, that was reported in the previous paragraph. Apart from confirming the reliability of the drop casting deposition method, the effect of CRE suppression can explain the enhanced permeation performances. Less frequently Pt catalyst agglomerates mean more available Pt particles employed in hydrogen separation processes. Interestingly, when activation energies are

calculated, values are in good agreement with results reported in literature (Table 16) but slightly varies from results obtained previously for membranes BCZY-GDC-A. Results are reported hereafter.

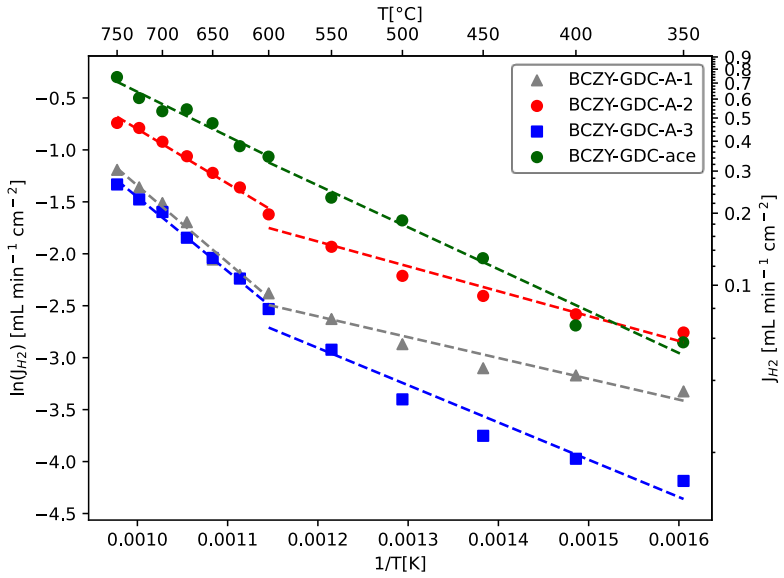

Figure 46 Arrhenius plot for activation energy calculations for membrane BCZY-GDC-A-1 (grey triangles), BCZY-GDC-A-2 (red circles), BCZY-GDC-A-3 (blue squares) and BCZY-GDC-ace (green circles).

Calculated results are reported in the following table (Table 20).

Membrane	Temperature (°C)	Activation Energy (eV)
BCZY-GDC-A-1	<600	0.173
	>600	0.640
BCZY-GDC_A-2	<600	0.207
	>600	0.454
BCZY-GDC_A-3	<600	0.310
	>600	0.616
BCZY-GDC-ace	<600	0.349
	>600	0.369

Table 20 Summary of activation energy calculation for tested membranes.

Membrane BCZY-GDC-ace present 0.349 eV for activation energy at low temperatures (<600°C) and 0.369 eV at high temperatures (>600 °C). Both values are still reasonably in the same range as the previous membranes (BCZY-GDC-A, reported in the table). For membrane BCZY-GDC-ace there is still a difference (0.02 eV) between the two calculated activation energies, but it significantly differs from previous result, respectively 0.476 eV for BCZY-GDC-A-1, 0.247 eV BCZY-GDC-A-2 and 0.306 eV for BCZY-GDC-A-3. This might lead to assume a more coherent contribution of the two hydrogen separation processes, but some specific experiments involving deuterium isotopes are required to correctly determine contribution relevancies. As remarked countless time in this elaborate, the determination of different activation energy in high temperature (T>600°C) and low temperature (T<600°C) range is due to different contribution to J_{H2} flow. This trend can be rationalized considering the prevailing contribution of water splitting reaction at high temperature [129], while at low temperature the decrease in activation energy is a consequence of the higher contribution of proton transport. Membrane BCZY-GDC-ace present more coherent results of activation energy

in the investigated temperature ranges. This might be attributed to the absence of a net distinction of permeated hydrogen contribution, namely, proton transport and WS are actively participating in the permeation of hydrogen for the whole investigated temperature range. In any case, it is worth reporting plotted H_2 flows considering the apparent permeated flow per mg of Pt catalyst (Figure 47).

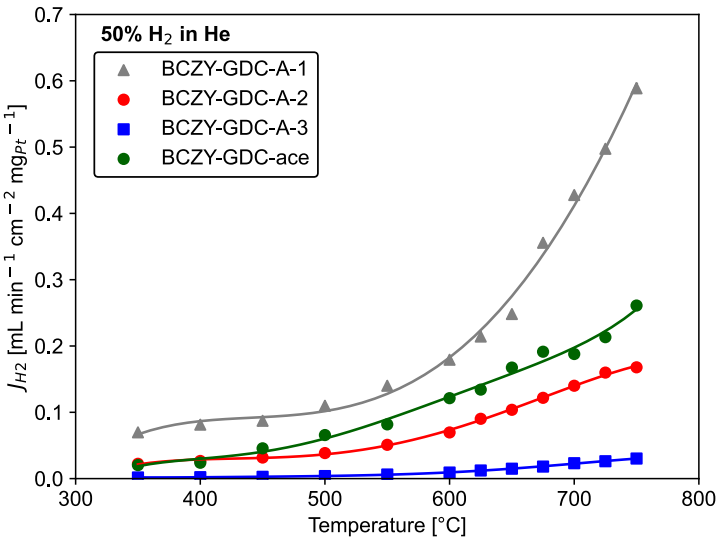

Figure 47 H_2 flows (mL min^{-1} cm^{-2} $mgPt^{-1}$) as a function of temperature for membrane BCZY-GDC-A-1, BCZY-GDC-A-2, BCZY-GDC-A-3 and BCZY-GDC-ace.

Observing results in Figure 47, It can be said that modification of Pt catalyst drop casting deposition method on porous layer led to increased H_2 flows per mg of Pt catalyst. This results more evident when temperatures are above 450 °C, where water splitting contribution to hydrogen permeation is more relevant.

4.11 Streams configurations.

Characterization of hydrogen performance was also tested by modifying stream current configurations. The first varied parameter was humidification degree of the feed and sweep current. As reported in section 1.7.4 Surface Modified Membrane, H_2 can be created by two mechanisms: WSR, which is primarily caused by oxide ion conduction, or H_2 permeation, which is driven by ambipolar proton and electron diffusion. Three distinct hydration configurations were used to discover which transport mechanism mostly contributes to H_2 production: (A) Only the feed side was humidified; (B) both sides were humidified; and (C) only the sweep side was humidified. Membrane BCZY-GDC-A-1, after permeation measurement, still presented suitable control parameter, and was employed to test different configuration at different temperatures, namely 750°C and 500°C, in order to better discriminate WSR contribution. Results are reported in the following figure (Figure 48).

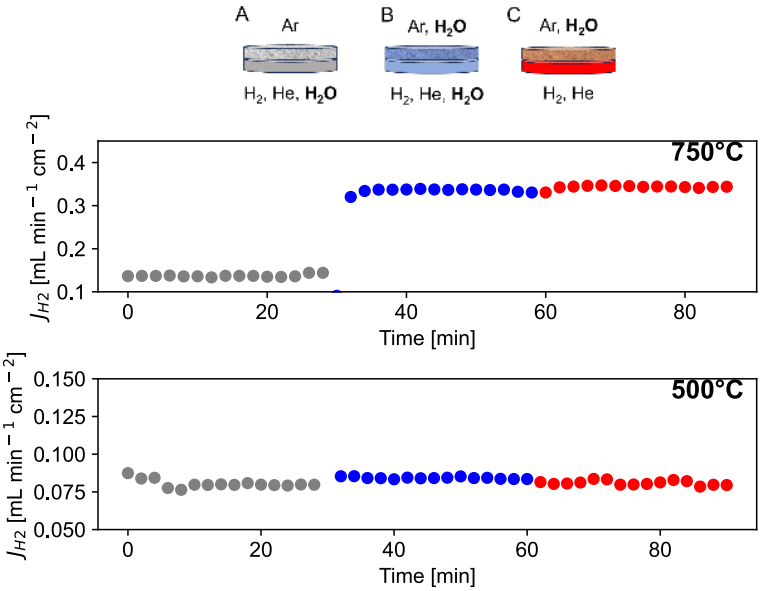

Figure 48 H_2 fluxes (mL min^{-1} cm^{-2}) as a function of temperature and humidification conditions: configuration (A) (only the feed side humidified), (B) (both sides humidified) and (C) (only the sweep side humidified), for membrane BCZY-GDC-A-1. Measurements were performed by feeding the dense layer with 50% H_2 in He at 750 °C. The insets show schematics of the membrane test configurations.

configuration	T = 500°C	T = 750°C	Increment [%]
A	0.0710	0.134	47.1
B	0.0842	0.319	73.6
C	0.0808	0.326	75.2

Table 21 Comparison between H_2 fluxes (J_{H2}) obtained at different temperature.

Switching from condition (A) to condition (B), namely adding steam in the feed, results in an increment in J_{H2} flow for both temperatures, with different magnitude for 500°C from 0.071 to 0.084 mL min^{-1} cm^{-2}, for 750°C from 0.134 to 0.319 mL min^{-1} cm^{-2}. When the J_{H2} value at different temperature are compared, the contribution of WSR is more relevant, as previously explained, at higher temperatures. The increment from 500°C to 750°C for condition (A) is 47.1% and is mainly due to higher molecular vibrations thanks to higher temperature, while for condition (B) is 73.6%, and is due to both increased temperature and WSR, contribution. This is in good agreement with oxygen ion retro-diffusion mechanism, described previously (see Figure 12). When oxygen partial pressure increases (configuration (B)), WSR is favoured, and overall hydrogen flows increases, with different magnitude, due to more relevant WSR kinetics at higher temperatures. Shifting from configuration (B) to configuration (C) should, theoretically, results in higher oxygen partial pressure and thus further increase J_{H2} flow thanks to the WSR contribution. This was not empirically true for temperature 500°C. there is a slight decrease in permeation. This might be also linked to analysis setup sensitivity limitation, due to very low hydrogen flows at 500°C. For 750°C, the increase in J_{H2} is present but in small increase, contrary to what expected. These results are in good agreement with what previously reported in literature [3], [129]. Reported variables employed to explain a possible cause to this unexpected behaviour are poor catalytical activation of the support layer and possible presence of mass transfer resistance [3], [129]. One further explanation might be linked to the drying stage of all pipes in the equipment is part of the testing experimental setup and also the hydration of dense layer of the membrane. Proton that are employed in permeation can originate

from H_2 gas molecule, but also H_2O (Figure 10) [114], and this might counter balance permeated H_2 coming from WSR contribution. To assess the potential contribution of mass transfer resistance to the porous support, the sweep and feed compositions were switched so that hydrogen was fed into the porous layer of the membrane. membrane BCZY-GDC-ace was employed for these test and results are reported hereafter (Figure 49). In the following section, the abbreviation F.S. is used to refer to the standard flow configuration (sweep gas on the porous side and feed gas on the dense side of the membrane) and F.I. refers to reverse flow configuration (sweep gas on the dense side and feed gas on the porous side of the membrane).

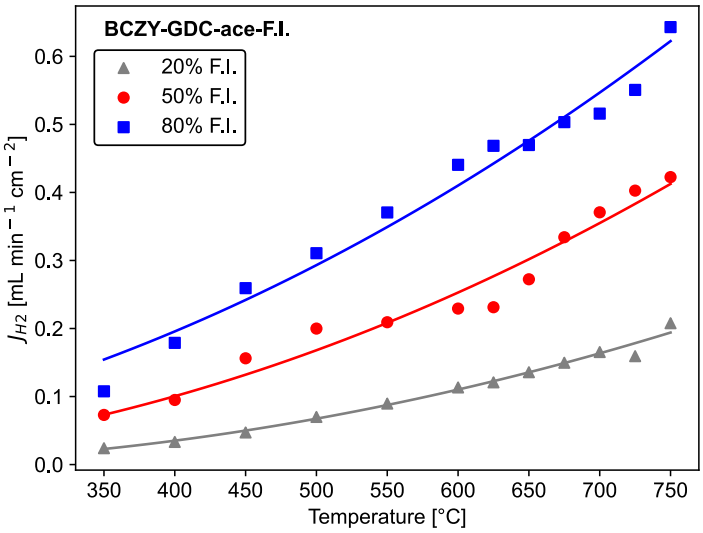

Figure 49 H_2 (mL min^{-1} cm^{-2}) flows as a function of temperature and feed composition for membrane BCZY-GDC-ace with inversed streams configuration (F.I.).

Figure 49 plots H_2 (mL min^{-1} cm^{-2}) flows as a function of temperature and feed composition for membrane BCZY-GDC-ace with inversed streams configuration (F.I.). Curves shows an increase in permeation performances when temperature and feed composition increases. Relevant information is obtained when flows configuration effect is observed. In Figure 50 hydrogen flows are plotted as a function of temperature, feed composition and flows configuration.

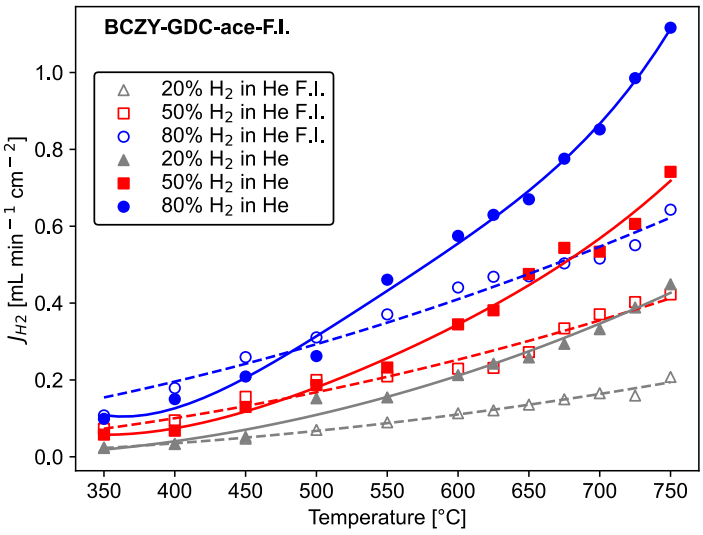

Figure 50 H_2 (mL min^{-1} cm^{-2}) flows as a function of temperature, feed composition (% H_2 in He) and streams configuration for membrane BCZY-GDC-ace. If not specifically stated, streams configuration is to be considered with standard flows configurations (FS).

Results can be observed focusing on two different temperature ranges, from 350°C to 450°C and from 500°C to 750°C. In the first temperature range results of flows inversion do not results in relevant difference in hydrogen permeation. This is ostensibly true for all composition, even though some points are unaligned, due to analysis setup sensitivity issues with low hydrogen flows. This can be ascribed mainly to proton transport mechanism, which should not be affected by flows inversion, unless porous layer mass transfer arises. When second temperature range is observed, there's a common behaviour for all inversed streams flows permeation curves, which is characterized by a definite diminished increase in hydrogen permeation. It is reasonable to assume that WSR is kinetically more relevant at higher temperature also during flows inversion, and thus a robust explanation of the diminished increase in hydrogen permeation lies in Pt catalyst amount per side. When WSR site is shifted from porous side to dense side, the amount of Pt catalyst is 10 times less, due to preparation and previous investigation. The decreased amount of Pt results in diminished increase in hydrogen permeation. Previously in literature, Montaleone *et. al* [3], observed the same results and pointed to mass transfer of porous support as limitation, not considering catalyst role. Lack of information on catalyst amount per side and morphology might lead to misinterpretation of involved phenomena, and overall, the description of results presented in this elaborate seems reasonably valid. For comparison, the same experiment has been conducted on membrane BCZY-GDC-A-2, to exclude the effect of Pt morphology from streams configuration (Figure 51). Mass transfer limitation might still be an occurring phenomena, though [192], but the effect of the Pt catalyst can still be appreciated in the previous investigation.

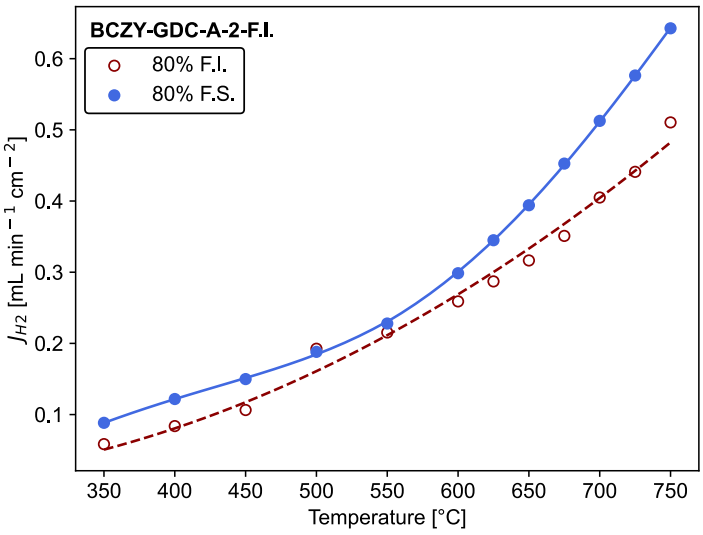

Figure 51 H_2 (mL min-1 cm-2) flows as a function of temperature and streams configuration for membrane BCZY-GDC-A-2.

No significant difference from membrane BCZY-GDC-ace's behaviour has been observed. Shifting from standard configuration to inverse configuration results in a decreased permeated hydrogen flow, due to reduced amount of Pt catalyst involved in WSR. A final confront between stream configuration inversion for membrane BCZY-GDC-ace and BCZY-GDC-A-2 is reported in Figure 52.

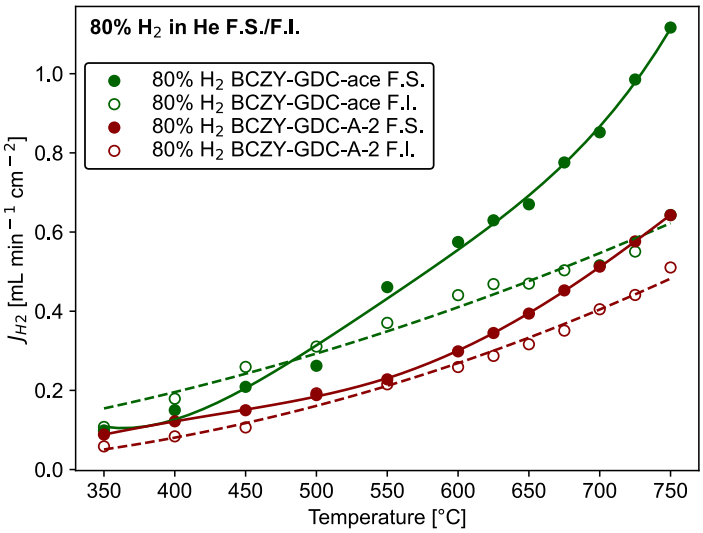

Figure 52 H_2 flows (mL min^{-1} cm^{-2}) as a function of membrane (BCZY-GDC-ace and BCZY-GDC-A-2) and stream configurations.

Percent different between standard flows and inverse flows are reported in the following table (Table 22).

T [°C]	BCZY-GDC-ace [%]	BCZY-GDC-A-2 [%]
750	73.64	25.90
725	78.92	30.68
700	65.16	26.59
675	54.12	28.95
650	42.65	24.50
625	34.40	20.15
600	30.49	15.29
Average	*50.47*	*22.24*

Table 22 Percent difference between standard flows and inverse flows for membrane BCZY-GDC-ace and BCZY-GDC-A-2, followed by averaged value.

Overall, membrane BCZY-GDC-ace has greater difference in hydrogen flows than membrane BCZY-GDC-A-2, with an average value of 50.47% respect to 22.24%. This performance is linked to the different distribution of Pt catalyst, which favours membrane BCZY-GDC-ace. When inverse flows hydrogen permeation of the two membranes are compared, it was expected negligible difference between the two membranes. Experimental data show similar shape of F.I. hydrogen permeation performances for the two membranes but membrane BCZY-GDC-ace has higher J_{H2} values. This discrepancy might be linked to the actual thickness of the dense layer of the membranes, which could explain an offset between the two curves (Eq. 36). Further investigation of membrane microstructure is necessary to correctly describe hydrogen permeation performance.

4.12 Deposition solvent modification - conclusions

The hydrogen penetrability of an asymmetric Cer-Cer composite planar membrane with the chemical composition $BaCe_{0.65}Zr_{0.20}Y_{0.15}O_{3-\delta}$(BCZY) – $Gd_{0.2}Ce_{0.8}O_{2-\delta}$ (GDC) was scrutinized in relation to temperature, feed side constitution, and catalyst quantity, utilizing moistened currents saturated at 28°C. To this aim, three feed constitutions, specifically 20%, 50%, and 80% H_2 in He (H_2 %vol), were assessed within the temperature range of 350°C to 750°C. The membrane was modified with 0.15 and 1.5 mg cm^{-2} on dense side and porous side respectively, but the deposition method has been modified in such a way to suppress coffee ring effect (CRE). In the previous section, the presence of CRE, favoured from higher Pt precursor, resulted in low hydrogen permeation performances. The use of a mixture of acetone and water as drop casting solvent revealed as a winning combination to produce Pt catalyst particle with absence of Pt agglomerates. Membrane obtained with this modification (BCZY-GDC-ace) was confronted with a similar one that was treated only with water as a drop casting solvent (BCZY-GDC-A-2). Pt catalyst particle have been studied with SEM analysis, revealing comparable dimensions of Pt particles with what obtained previously with 100% H_2O as a drop casting solvent, even though the incidence of Pt agglomerate was not revealed by SEM analysis. For what concerns permeation performances, the results showed a definite enhancement of J_{H2} values for membrane BCZY-GDC-ace, in particular at higher temperatures (T > 450°C). This experimental data was ascribed to prevalent effect of Pt morphology on water splitting reaction, which is more prevalent at higher temperatures [3]. It is worth noticing that the use of modified drop casting method provided higher Pt catalyst efficiency, in terms of hydrogen permeation per gram of Pt catalyst.

Once again, for the sake of repetition, it is of great importance highlighting the critical findings determined in this elaborate. The metallic catalyst, frequently employed in literature to surmount

constraints in surface kinetics [129], [146], [147], [149], [150], [165], [168], [184], [186], [188], [189], undeniably plays a definitive role in the permeation efficacy of membranes. In the previous section (Tape Casting Membranes) the effect of different amount of catalyst firstly highlighted the relationship between permeated hydrogen and the processes involved (proton transport and WS). Not only catalyst amount can positively affect the permeation performances of consistently similar membranes, but also the catalyst morphology is essential for ensuring optimal Pt availability, and thus activity, in the overall process of hydrogen separation. The unveiling of this revelation is of great importance as it provides fresh insights into the intricate interplay between catalysts and membranes. The consequences of this discovery extend widely, as it has the capacity to transform the prevailing comprehension of membrane technology and its various applications. Moreover, this research emphasizes the requirement for a more comprehensive understanding of the fundamental mechanisms that govern the interaction between catalysts and membranes.

4.13 Freeze Casting membranes

Membrane BCZY-GDC-ace hydrogen performances showed interesting hydrogen permeation. Nevertheless, to spark industrial interest, permeated hydrogen must reach values higher than 1 mL min^{-1} cm^{-2}, in plausible condition, namely 750°C and 50% H_2 in He (%vol) [191]. Aside from decreasing the active thick layer, microstructure engineering of the porous support is a major technique for lowering its mass transfer resistance and permitting operation at high flow streams, which would allow it to attain industrial targets [215], [216]. In fact, systems with hierarchically organised porosity, low pore tortuosity, and appropriate mechanical qualities are becoming more and more popular for use in gas separation applications [216]. In comparison to traditional dense and supported membranes, Dong *et al* [215], [217] reported greater oxygen fluxes (3.4 and 3.63 mL min^{-1} cm^{-2}) in the air-oxygen separation for microchannel $La_{0.6}Sr_{0.4}Co_{0.2}Fe_{0.8}O_{3-d}$-based structures generated by phase-inversion technique. It is shown that the higher permeability is connected to the straight channels' quick pathway for oxygen diffusion. Cheng *et al.* [218] demonstrated how to develop a dual-phase LSM-YSZ composite membrane with large, ring-shaped finger-like holes that dramatically increase oxygen permeability. Serra *et al.* [219] detailed the creation of dual-phase oxygen-permeable asymmetric membranes using a freeze-casting and screen-printing combination. This membrane demonstrated an encouraging oxygen permeability value of 6.8 mL min^{-1} cm^{-2} at 1000°C, highlighting the need of reducing the pressure drop of the porous support to improve the membrane performances [220]. The ice-templating process was used to create porous BCZY-GDC ceramics for the first time, resulting in membrane supports with well-organized and aligned porosity for hydrogen separation performance testing, that were characterized in this elaborate. To appreciate the porous layer morphology difference obtained with tape casting and freeze casting porosity shaping methods, the following picture is reported (Figure 53).

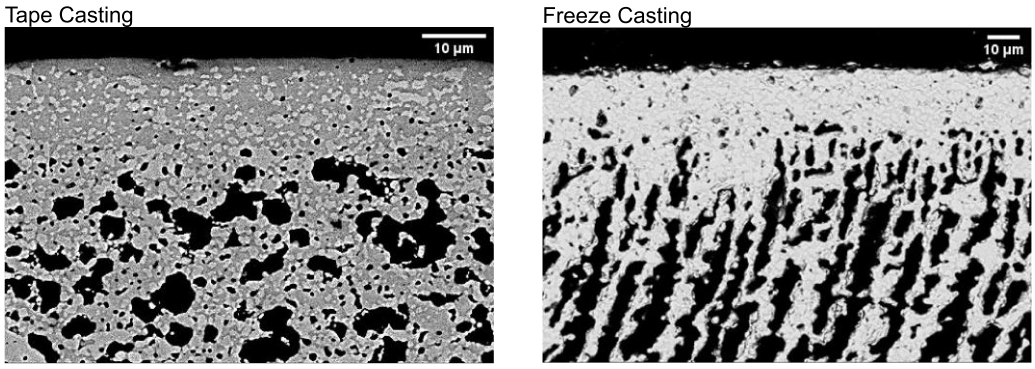

Figure 53 SEM micrograph of the cross section of Freeze Casting shaped membrane and Tape Casting shaped membrane (adp.)[3].

Main characteristics of tested membranes are reported in Table 23.

Membrane	Type	Thickness (um)	Diameter (mm)	Deposition	Additional Info
Mbr2.00w	Asym.	1990	15.05	Side B 1.5 mg cm^{-2}, H_2O Side A 0.15 mg cm^{-2}, H_2O	Side B porous Side A dense
Mbr2.00	Asym.	2000	14.94	Side B 1.5 mg cm^{-2}, H_2O/ace Side A 0.15 mg cm^{-2}, H_2O	Side B porous Side A dense
Mbr0.85	Asym.	850	15.65	Side B 1.5 mg cm^{-2}, H_2O/ace Side A 0.15 mg cm^{-2}, H_2O	Side B porous Side A dense

Table 23 Characteristics of the hierarchically-structured BCZY-GDC membranes considered. ace = acetone.

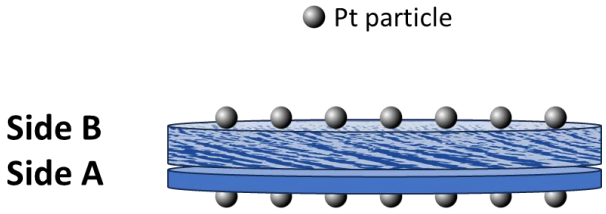

Figure 54 schematic representation of conventions and membranes considered in Table 23

As reported in Table 23 and Figure 54, membranes tested in this section were Pt activated to promote both hydrogen activation and water splitting reactions while avoiding surface kinetic effects on permeation. Hydrogen permeation performances were thoroughly investigated modifying the following parameters: (i) temperature, (ii) feed stream composition, (iii) drop casting deposition solvent, (iv) porous layer thickness, (v) streams configuration. First and foremost, the effect of the deposition solvent was investigated, employing membrane Mbr2.00w and Mbr2.00 (Table 23), for the same explanation reported in section 4.5. Results are reported in the following figures.

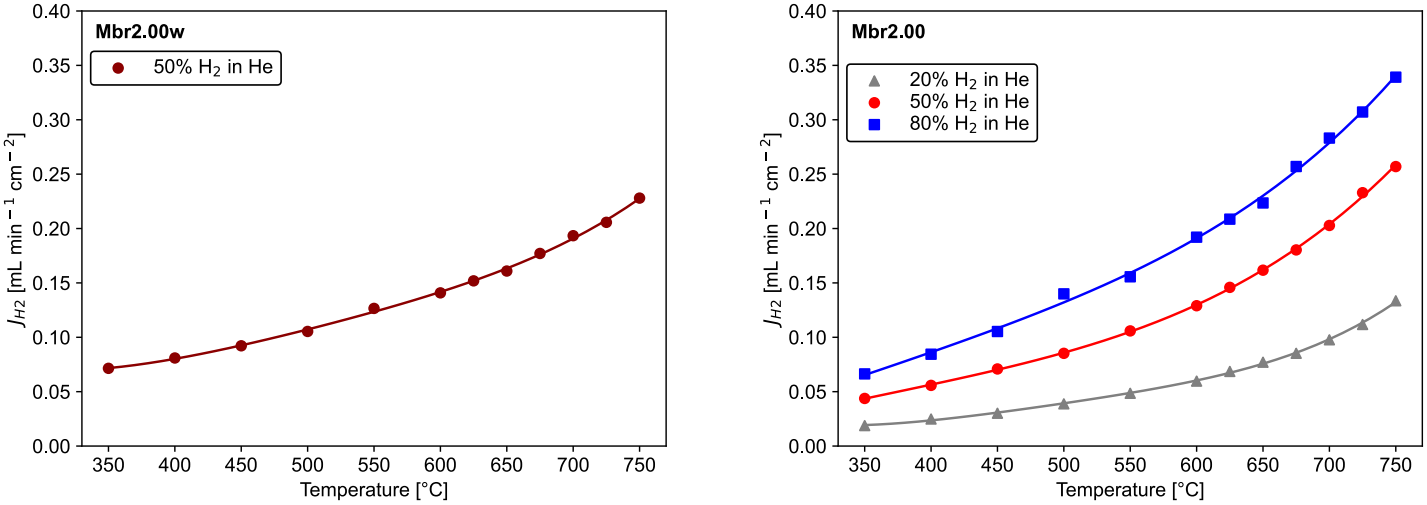

Figure 55 H_2 flow (mL min^{-1} cm^{-2}) as a function of temperature, feed stream composition and deposition solvent.

Membranes Mbr2.00w and Mbr2.00 have roughly similar thickness, and thus the main effect observed in hydrogen flows should be reasonably linked to the drop casting solvent modification. Figure 55 plots hydrogen permeation performance as a function of temperature and feed stream composition. Sadly, membrane Mbr2.00w was mechanically stable only for the tracing of the 50% H_2 in He and no further data was acceptable. It is possible to observe that increasing temperature results in increased permeation for both membranes and for every feed composition. Highest recorded values for membrane Mbr2.00w is 0.23 mL min^{-1} cm^{-2} at 750°C, 50% H_2 in He (%vol) while for membrane Mbr2.00 is 0.34 mL min^{-1} cm^{-2} at 750°C, 80% H_2 in He (%vol), in both cases feed and sweep streams were humidified. In order to better observe the effect of the deposition solvent, the following comparative plot is reported.

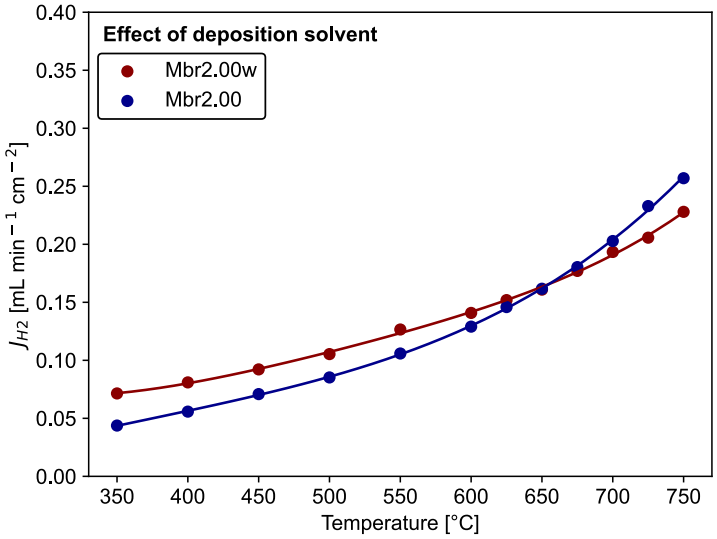

Figure 56 H_2 flow (mL min^{-1} cm^{-2}) as a function of temperature and different drop casting solvent.

Figure 56 can be described by observing permeation results divided in two sections, at low (<650°C) and high (>650°C) temperatures. At lower temperatures, membrane Mbr2.00w shows higher J_{H2} values, with an average of 0.019 mL min^{-1} cm^{-2} difference between points. At higher temperatures, membrane Mbr2.00 shows a rapid increase of permeation performances, reaching 0.26 mL min^{-1} cm^{-2} at 750°C, with both current humidified, while membrane Mbr2.00w 0.23 mL min^{-1} cm^{-2} with the same permeation condition. The effect of deposition solvent might affect, once again, the WSR predominantly, by modifying Pt catalyst morphology. To confirm this hypothesis, SEM analysis was carried out on both membrane, and results are reported hereafter.

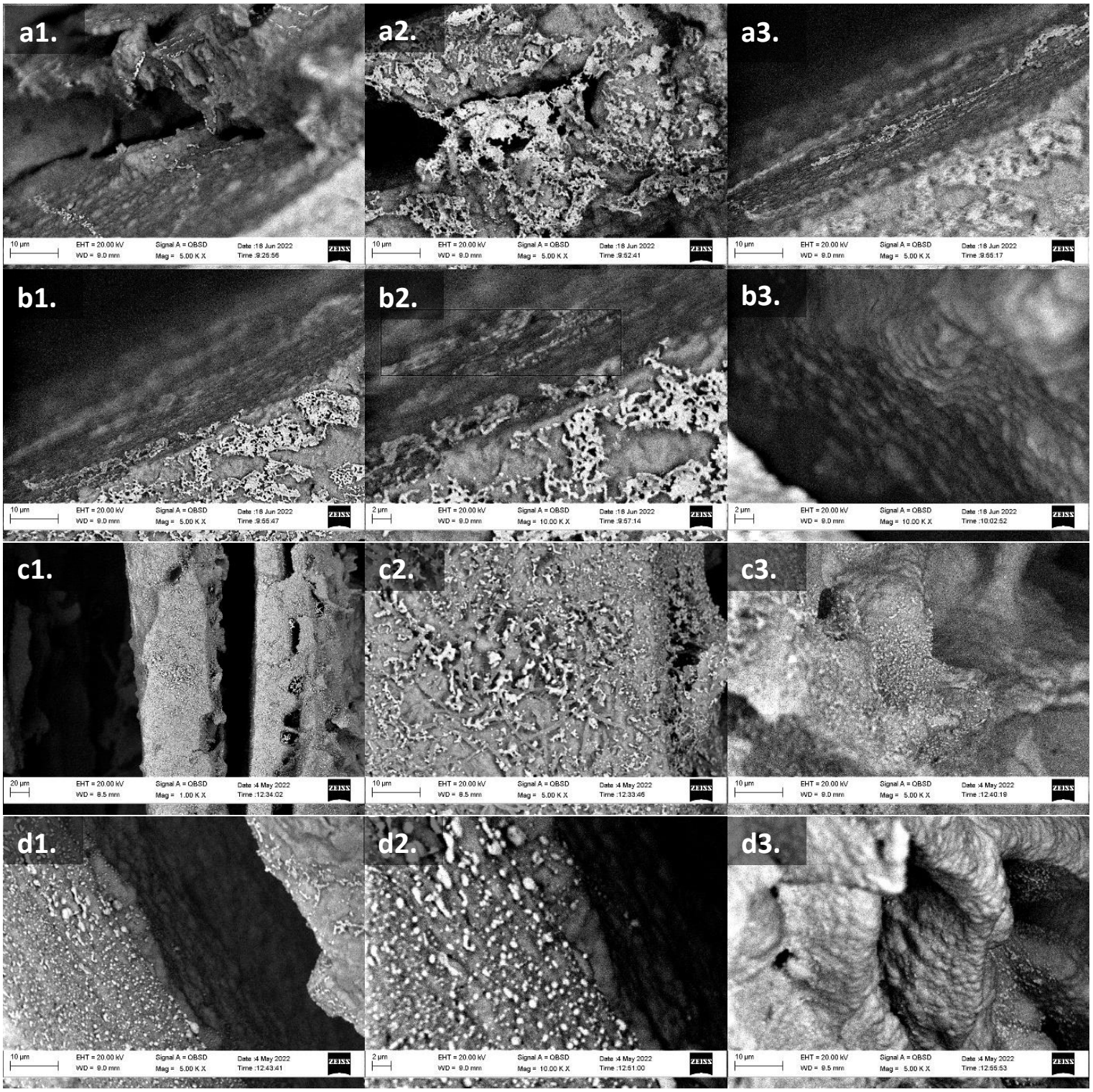

Figure 57 Representative SEM acquisitions of membrane Mbr2.00w (a, b) and Mbr2.00 (c, d).

Figure 57 reports SEM pictures acquired on different side of membranes' surface, namely some flat surface on top and, where possible, inside the pores. Membrane Mbr2.00w (Figure 57 (a, b)) presented predominantly big Pt agglomerates, especially on top flat available surfaces of the membrane (Figure 57 a2, b1). When pores cavity is investigated, it is possible to observe lack of Pt particles (Figure 57 a1, b3), accompanied by presence of occasional Pt agglomerates (Figure 57 a3, b1). This particular Pt particle distribution is mainly attributed to water solvent properties, that

produces Pt agglomerates with poor cavity penetration. On the contrary, membrane Mbr2.00 shows presence of Pt particles, with average radius of 0.5 µm, (Figure 57 c1, c2, d2) and no agglomerates were observed. For what concerns pores cavity, presence of Pt particles has been observed (Figure 57 c3, d3) deep inside the pores, to a certain extent. The presence of Pt particles on Mbr2.00, with higher available surface might better favour WSR at higher temperatures (>650°C) with respect to lower active surface Pt agglomerates present in membrane Mbr2.00w. At lower temperatures (<650°C), where hydrogen permeation major contribution comes mostly from proton conduction, the effect of membrane microstructure (*e.g.* dense layer thickness) could be mostly prominent. *Post mortem* XRD analysis showed absence of structural modification after permeation testing (Figure 58).

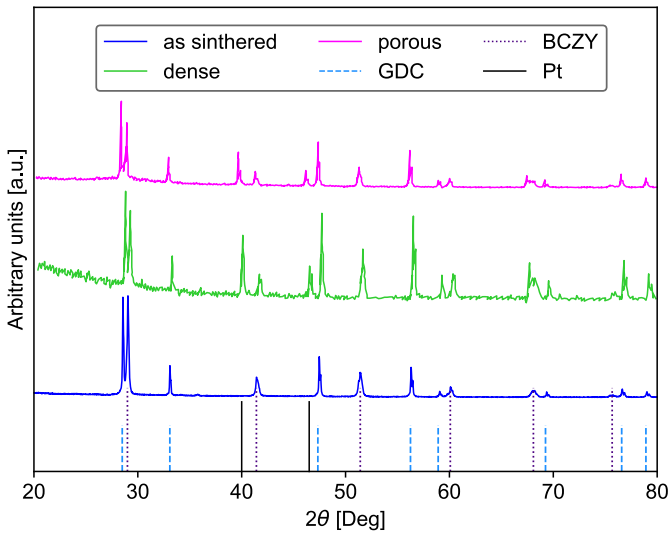

Figure 58 XRD diffractogram of porous and dense sides of the hierarchically-structured BCZYGDC membrane generated through screen printing/freeze casting obtained before and after permeation testing (adpt.)[192].

The dense membrane layer's XRD diffractogram indicates the preservation of pure BCZY-GDC phases, showing that the production process had no effect on the stability of the dual perovskite-fluorite phases [192]. On XRD diffractograms of dense and porous layers of post-permeation membrane the presence of platinum peaks can be observed, while this is absent on the "as sintered" spectrum, as expected. In order to better understand different mechanism contribution for hydrogen permeation, activation energy was calculated as following (Figure 59).

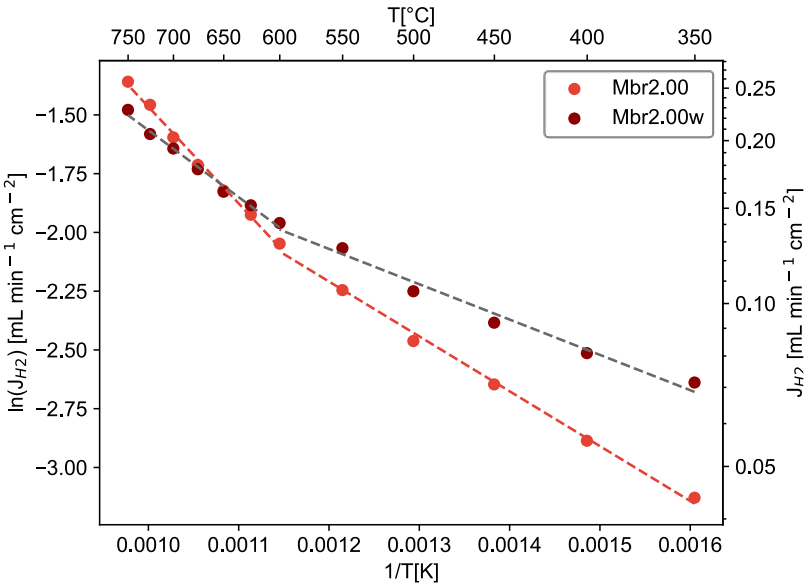

Figure 59 Arrhenius plot of membrane Mbr2.00 and Mbr2.00w. H_2 flows recorded at 50% H_2 in He (%vol) with both current humidified to saturation at 28°C.

The numerical results are reported in the following table (Table 24).

Membrane	Temperature (°C)	Activation Energy (eV)
Mbr2.00w	<600	0.13
	>600	0.24
Mbr2.00	<600	0.20
	>600	0.35

Table 24 summary of activation energy calculated in different temperature ranges for membrane Mbr2.00w and Mbr2.00.

Both membranes presents different value for different temperature ranges, 0.13 eV and 0.24 eV for membrane Mbr2.00w, 0.20 eV and 0.35 eV for membrane Mbr2.00 [192]. This discrepancy has already been observed in literature [3] and is attributable to the predominance of various transport pathways, as previously described. At T > 600°C, a larger activation energy is owing to the predominant oxygen ion transport followed by water splitting, whereas a lower activation energy is due to a greater proportion of proton transfer through the membrane. In both temperature ranges, membrane Mbr2.00w present lower activation energy values with respect to membrane Mbr2.00. Considering permeation measurement (Figure 56) and SEM pictures (Figure 57) as well as apparent activation energy (Table 24), investigations point to the hypothesis that WS reaction and subsequent hydrogen permeation is positively affected by drop casting solvent modification, thanks to the improved Pt catalyst morphology. For what concerns hydrogen separation temperature, the ideal value should be relatively close to the industrial application, that, due to technological challenges, still relies on reforming of natural gas and the gasification of coal [61]. Typically, natural gas reforming is a strongly endothermic reaction and the reactor temperature is quite high (700°C – 1000°C) [42], [221], [222], so the ceramic membrane should be employed at high temperature, to avoid cooling costs. For this particular reason, it was considered appropriate to utilize the solvent mixture (Acetone and Water, 50% %vol) to deposit Pt on the next membrane.

The material reported in the following section is part of a published literature paper [192]. Asymmetric architecture configurations are utilized with the intention of connecting a mechanically robust porous structure with a slim compact layer, resulting in a reduction of the operative compact membrane portion's dimension (L) and an increase in permeation [216]. In systems of this nature, the layer that is porous functions as a mechanical foundation for the thin layer that is active and densely packed, thereby providing the requisite mechanical stability to the entire system. Nonetheless, it is essential to engineer the porosity of the support in a suitable manner so as to reduce the resistance associated with mass transfer [215], [223] and eventually enable it to be activated with a catalyst that is specific to its needs. In order to gain an understanding of the impact that variations in porous support thickness may have on the ultimate hydrogen permeation results, we have analysed membranes which possess a comparable dense layer thickness yet differ in their respective porous support thicknesses. Specifically, we have investigated membranes designated as Mbr2.00 and Mbr0.85, with thicknesses of 2.00 mm and 0.85 mm, respectively (for further detail, see Table 23). Permeation performances are reported in (Figure 60). The temperature range of 350 to 750 ◦C was utilized for the purpose of studying three distinct compositions of feed streams, which include 80%, 50%, and 20% (H_2 %vol). The increase in permeated hydrogen in both sets of samples is directly proportional to the escalation in temperature and hydrogen partial pressure, as predicted by the Wagner equation and water splitting contribution. Upon comparison of the J_{H2} performances of the two membranes, some interesting information was revealed. It is noteworthy that Mbr2.00 exhibits slightly higher J_{H2} at temperatures lower than 700 °C, while this tendency is reversed at 750 °C, where the Mbr0.85 membrane evidences a sharp rise in permeation values. This pattern is in agreement with a different degree of the two separation phenomena discussed earlier, which occur in Pt-activated BCZY-GDC based membranes: (1) movement of protons and electrons through the dense layer, (2) water splitting reaction in the sweep side, owing to oxide-ion conduction of the composite at temperatures higher than 650 °C [138], [146], [149], [223], [224].

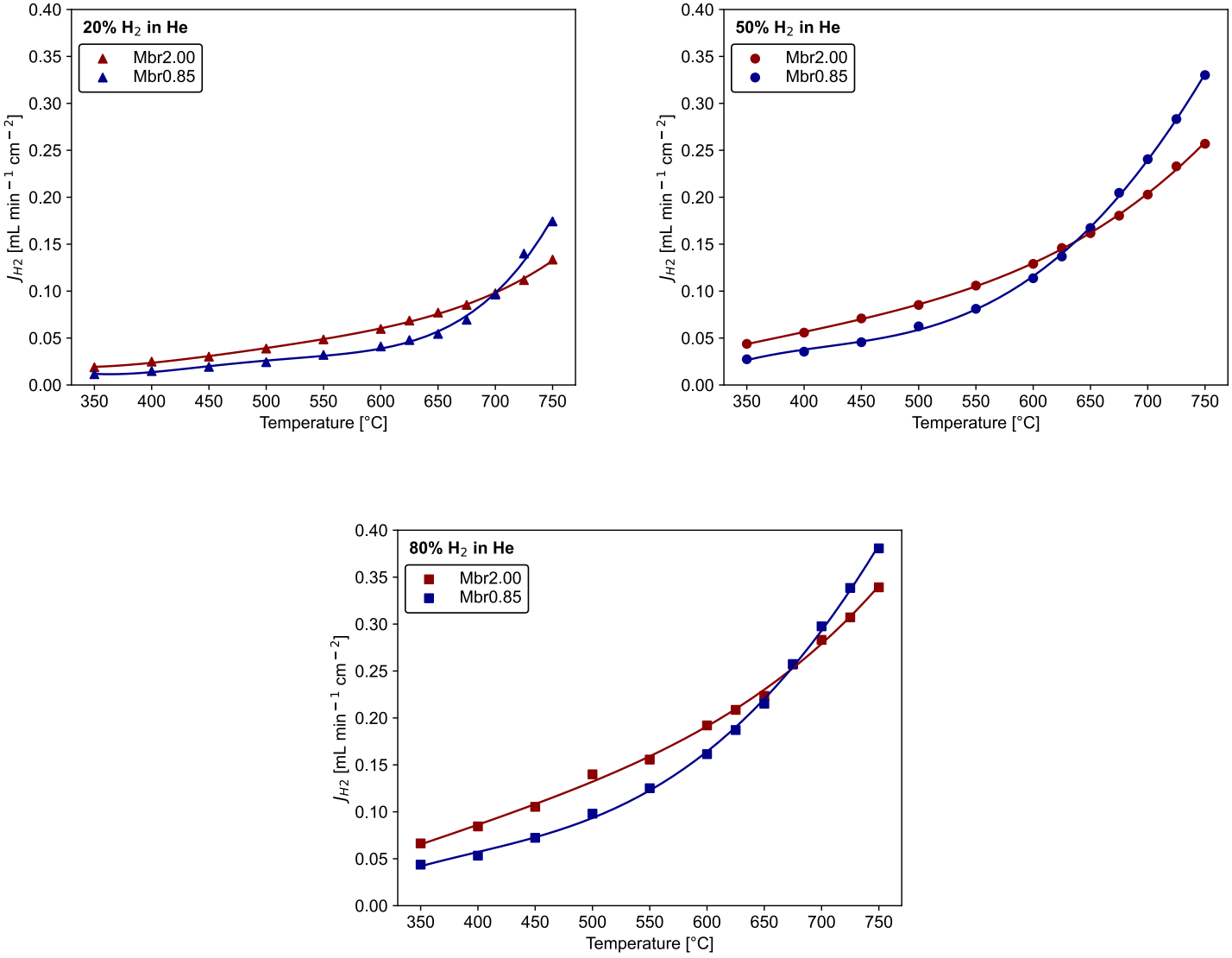

Figure 60 H_2 permeation flows (mL min^{-1} cm^{-2}) as a function of temperature and feed stream composition for membrane Mbr2.00 (red) and Mbr0.85 (blue) (adpt.)[192].

The aforementioned occurrence is linked to the existence of Pt within the permeable structure. During lower temperatures, the primary occurrence is the diffusion of hydrogen through the dense layer, whereas during higher temperatures, the process of water splitting plays a more significant role. The significant rise observed in the Mbr0.85 permeation curve, when the temperature exceeds 700 °C, can be explained by the presence of Pt locations in proximity to the dense layer. This results in a more efficient transportation of O^{2-}, thereby augmenting the rate of the water splitting reaction in the thinner membrane. The dilution of Pt particles in the Mbr2.00 porous substrate is believed to be the primary cause for this phenomenon in respect to membrane Mbr0.85, considering the same Pt loading used for the two different samples (Figure 61).

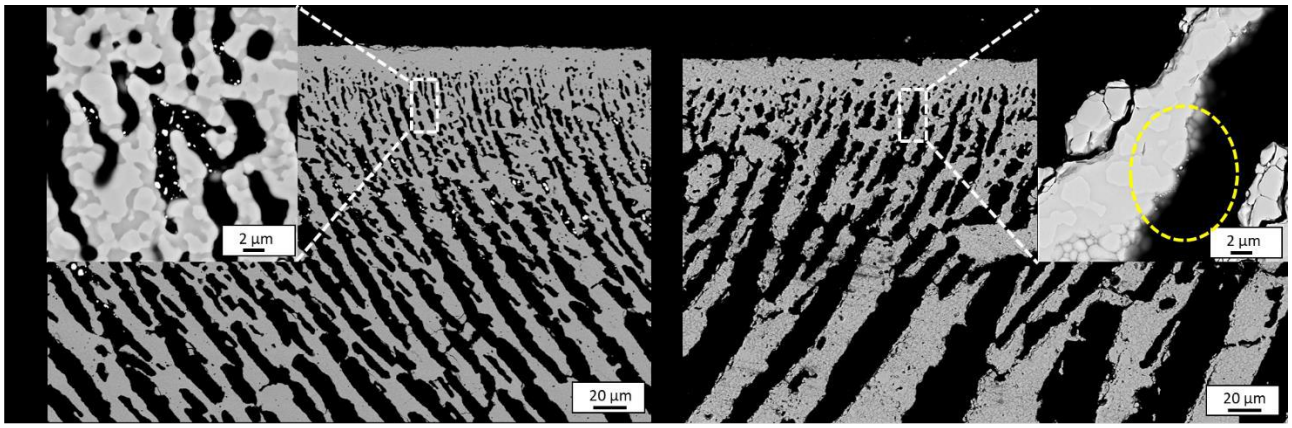

Figure 61 SEM micrographs of the polished cross-section of the BCZY-GDC membrane following permeation tests, Mbr0.85 (left) and Mbr2.00 (right) at varying magnifications. The Pt nanoparticles are denoted by white dots, while the yellow circle highlights the region where Pt was detected. It should be noted, however, that this characterization approach is not suitable for providing quantitative information regarding the catalyst's concentration and penetration depth within the supports (adpt.)[192].

The increased thickness of Mbr2.00 indicates that a substantial portion of the Pt is farther away from the dense side, or at the very least, less densely concentrated (assuming identical Pt penetration depth) compared to Mbr0.85, necessitating a longer path for O^{2-} transportation across the porous matrix. Conversely, Mbr0.85 displays a greater concentration of Pt particles in close proximity to the dense side (Figure 61 left) compared to Mbr2.00 (Figure 61 right). The transport phenomena constraints of Mbr0.85 in the water splitting reaction are significantly improved due to this positive effect. However, the permeation performances achieved at temperatures below 600 °C, which are mainly influenced by proton and electron transfer through the dense active layer, have a complex relation with various factors such as average thickness, residual porosity (Table 25), surface roughness, and sample homogeneity in terms of defects and microstructure. Hence, it is important to comprehensively analyse these factors to optimize the overall performance of the system.

Sample	Membrane Thickness (mm)	Total open porosity ISO (%)	Dense layer thickness (µm)	Residual porosity (%)
Mbr0.85	0.85 ± 0.01	49.8 ± 2.2	13.0 ± 1.0	1.5 ± 0.7
Mbr2.00	2.00 ± 0.01	51.9 ± 1.1	14.5 ± 1.5	1.3 ± 1.0

Table 25 features of the BCZY-GDC membranes with a hierarchical structure employed for the purposes of conducting hydrogen permeation tests.

Based on our analysis, we posit that the marginally elevated permeation flux observed for Mbr2.00 within the 350-650 °C range may be attributable to a comparatively thinner and/or more compact active layer in relation to Mbr0.85. However, the restricted standard deviation of the morphological parameters (thickness/residual porosity) of the dense layers of the two membranes precludes a definitive morphology-permeation correlation. Consequently, more precise scrutiny of the microstructure (e.g., via micro-CT techniques) will be conducted to further investigate this tendency at lower temperatures. The observation of distinct water splitting behaviour between the two systems was further confirmed upon examination of the results in the form of percent increase in permeation between J_{H2} values recorded at 500 °C (a temperature at which water splitting is negligible) and at 750 °C. Through extensive calculation of data obtained with 50% H_2 in He (H_2

%vol), a notable increase in hydrogen permeation from 500 to 750 °C was observed, as detailed in the accompanying equations:

$$Mbr0.85\Delta\% = \frac{J_{H_2 750-500°C}}{J_{H_2 750°C}} = 80\%$$

$$Mbr2.00\Delta\% = \frac{J_{H_2 750-500°C}}{J_{H_2 750°C}} = 66\%$$

In order to conduct a more extensive analysis of the impact of membrane architecture and the thickness of the porous layer on the various phenomena that occur during H_2 permeation, the fluxes of streams were reversed. Specifically, the feed current was directed towards the porous side of the membrane (known as the Inverse Fluxed, F.I.), while the sweep stream (where water splitting occurs) was directed towards the dense side. These tests were conducted on the same membrane, with the inlet permeate and retentate flows being swapped in order to achieve the inversion of flows. (Figure 62) plots H_2 permeation performances as a function of temperature and streams configurations, namely standard configuration (feed current on dense side, F.S.) and inverse configuration (feed current on porous side, F.I.).

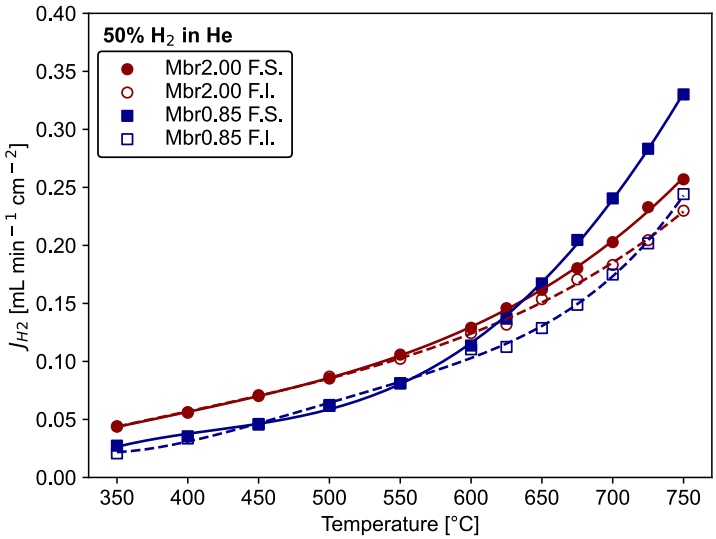

Figure 62 H_2 fluxes (mL min^{-1} cm^{-2}) as a function of temperature. Measurements were performed in both configurations: i) feeding with 50% H_2 in He (H_2%vol) the porous support (configuration F.I.) and, ii) feeding with 50% H_2 in He (H_2 %vol) the dense side (configuration F.S.). In both configuration, feed stream and sweep stream were humidified to equilibrium at 28°C (adpt.)[192].

For both types of membranes, altering the feed stream from the standard fluxes on the dense side (F.S.) to the inverted fluxes on the porous side (F.I.) does not yield distinct J_{H2} values at temperatures below 600 °C. However, at temperatures above 600 °C, a difference in permeation between the two configurations is observed, particularly for Mbr0.85, wherein an increase in permeation occurs when the permeate is directed to the porous side. It is important to note that the amount of Pt present on the porous side is 10 times greater than that on the dense side. Thus, it is imperative for the systems to exhibit a heightened catalytic effect on water splitting during evaluation in the standard configuration, wherein the porous support is subjected to a humidified sweep stream.

Mbr0.85 conforms to this requirement. On the contrary, Mbr2.00 demonstrates similar curves for both standard (F.S.) and reverse flow (F.I.) configurations, indicating that the Pt amount has negligible impact on permeation performances. This occurrence can be attributed to the low concentration of Pt particles in the thicker porous support and the existence of mass transfer limitations (Figure 61). The phenomenon of concentration polarization effect, can be attributed to the porous setting of the material in question, even though is characterized by well oriented pores. It is noteworthy that an interesting study has demonstrated the potential for avoiding concentration polarization in the case of uniform freeze casted pores. However, it is important to note that this avoidance can only be achieved if the average diameter of the pores is higher than 20 μm [225]. Present membranes reported in this study are distinguished by their notably diminutive average pore diameters, which are discernible from the scanning electron microscope (SEM) images that are illustrated in Figure 61. Therefore, it is plausible that the performance of said membranes could be restricted by the concentration polarization effect. Ultimately, after conducting a thorough investigation, the apparent activation energies of both membranes were carefully calculated in order to obtain a deeper understanding of the contribution to permeation resulting from various phenomena. This information is presented in Table 26. Specifically, the apparent activation energies that were calculated for Mbr0.85 and Mbr2.00 (0.26 and 0.20 eV at T < 600 °C, and 0.55 and 0.35 eV at T > 600 °C, respectively) are notably comparable to those of other dense ceramic membranes that have been documented in the literature (as outlined in Table 16). It is noteworthy that these membranes exhibit two distinct activation energies within the temperature range that falls below and above 600 °C. This disparity has been previously reported in relevant literature [3].

Sample	T < 600°C	T > 600°C
Mbr0.85	0.26 eV	0.55 eV
Mbr2.00	0.20 eV	0.35 eV

Table 26 Activation energy summary for membrane Mbr0.85 and Mbr2.00. Calculation have been carried on permeation performances recorded with 50% H_2 in He (% vol) feed stream. Both feed and sweep streams were humidified to equilibrium at 28°C.

The reason for the aforementioned phenomenon can be attributed to the existence and prevalence of a multitude of diverse transport mechanisms, as previously expounded upon. An increase in activation energy is intrinsically linked to the preponderance of oxygen ion transportation, which is succeeded by water splitting at temperatures surpassing 600 °C. Conversely, a diminution in activation energy at lower temperatures arises as a result of a heightened participation of proton transfer through the membrane.

Further investigation is required to comprehensively analyse and contrast the morphological and microstructural characteristics, specifically tortuosity, average pore opening diameter, specific surface area, and porosity, of the porous supports generated through traditional tape-casting and freeze casting methods. Furthermore, in conjunction with optimizing the morphological and microstructural properties, such as thickness and densification level, of the thin active layer, these findings will be of paramount significance in constructing models that can effectively recognize the key parameters, including material properties, catalysts, microstructural properties, and operational conditions, that are most influential in enhancing the H_2 permeation of ceramic

membranes. Nevertheless, although the results presented in this elaborate [192] are groundbreaking and lay the foundation for future research aimed at creating ceramic-based membranes utilizing non-conventional techniques for generating hierarchically engineered porosity, additional investigations are still required.

4.14 Freeze Casting membranes – conclusions

An innovative type of ceramic membrane for hydrogen separation was investigated for the first time. A set of hierarchically-structured $BaCe_{0.65}Zr_{0.20}Y_{0.15}O_{3-\delta}$(BCZY) – $Gd_{0.2}Ce_{0.8}O_{2-\delta}$ (GDC) membranes was investigate thoroughly varying (1) temperature, (2) feed composition, (3) deposition solvent, (4) porous layer thickness, (5) streams configurations. Hydrogen permeation tests were conducted in the 350–750 °C temperatures range using three different feed compositions (20%, 50% and 80% H_2 in He, %vol). The effect of temperature and feed composition was in good agreement with Wagner's law. Increasing either temperature or feed composition resulted in increased J_{H2} values.

The effect of deposition method was Investigated observing H_2 permeation of two membranes, Mbr2.00w and Mbr2.00, where Pt catalyst deposition solvent was 100% H_2O and 50% H_2O:Acetone respectively. Employing a mixture of Acetone and water resulted in better hydrogen permeation at temperatures (T > 650°C), reaching 0.26 mL $min^{-1}cm^{-2}$ at 750°C with 50% H_2 in He (%vol) for Membrane Mbr2.00. Pt particles, analysed by means of SEM imaging, benefited by the presence of Acetone in the solvent mixture, resulting in detected particle of smaller dimensions. It is also worth noticing the presence of Pt particles inside the pores of the membrane Mbr2.00.

The next investigation concerned the effect of porous layer thickness, employing two comparable membranes, Mbr0.85 and Mbr2.00, with comparable active dense layer and a porous layer of 0.85 mm and 2.00 mm respectively. The reduction of porous layer thickness led to a hydrogen apparent permeated flow of 0.33 mL $min^{-1}cm^{-2}$, at 750°C with 50% H_2 in He (%vol), with both streams humidified at 28°C. This was ascribed to the Pt-catalysed WS reaction, at high temperature, favoured by more concentrated Pt particles in the tri-dimensional porous framework of the thinned membrane. Further investigation will be required in the near future to better understand the effect of material key properties onto permeation, to better engineer membrane production with the goal of reaching higher hydrogen flows to spark industrial interest.

4.15 Comparison of freeze-dried and tape-cast support microstructure on H_2 permeation performance

As previously stated, the employment of freeze casting porosity shaping method allow the production of asymmetric membrane with advantageous characteristics. It is reported in literature though, that a non-adequate engineerization of the microstructure of the support might negatively affect the gas permeation performance because of polarization resistance, due to gas transfer becoming rate limiting step[235], [236], [237], [238], [239]. For this reason, it was deemed relevant to attempt a comparison between two membranes produced by different porosity shaping method. Geometric and microstructural properties are briefly reported in Table 27.

membrane	porosity shaping method	Total open porosity [%]	Thickness [mm]	Active layer thickness [µm]	Pt amount (dense side-porous side) [mg cm-2]
BCZY-GDC-A-2	Tape casting	48	0,68	20	0,15-1,5
Mbr0.85	Freeze casting	49.8	0,85	13	0,15-1,5

Table 27 Geometric properties and microstructure of selected membrane for comparison of porosity shaping method.

Unfortunately, the two membranes have slightly different properties, due to natural variability of production methods outputs, that cannot produce exactly identical materials. Despite natural variability occurrence, qualitative discussion is still possible. The following figure (Figure 63) shows the permeation performances under similar feed stream conditions. The active layer thickness is relevant for permeation performances, and it is necessary for a correct evaluation to normalize the permeation on the active layer thickness.

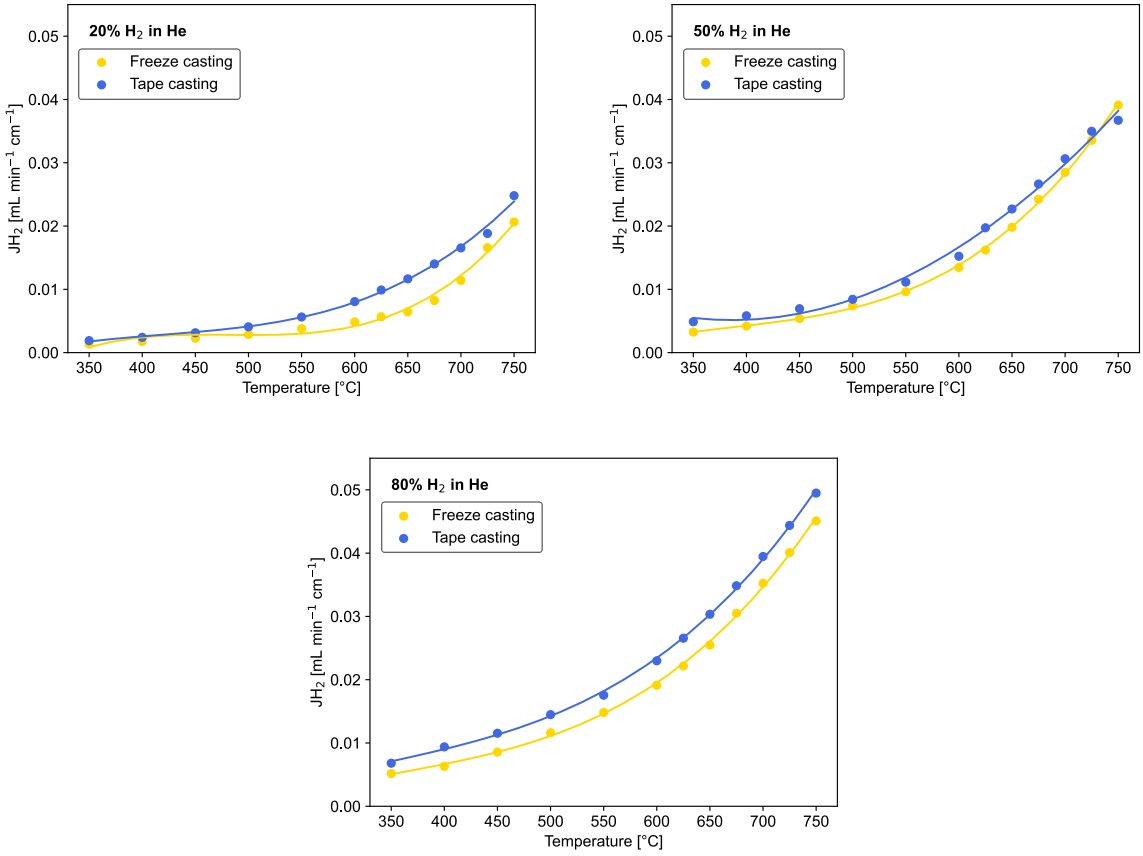

Figure 63 Comparison of permeation performances of asymmetric membranes with tape casting (blue) and freeze casting (yellow) as a function of temperature and feed stream composition (20, 50, 80% H_2 in He, %vol).

Figure 63 shows the active layer thickness normalized permeation performances. A small difference in permeation is visible for all curves, and to appreciate better the intensity of this difference the following value is plotted separately (Figure 64).

$$\Delta\%J_{H_2} = \frac{J_{H_2}(\text{tape casting}) - J_{H_2}(\text{freeze casting})}{J_{H_2}(\text{tape casting})} * 100$$

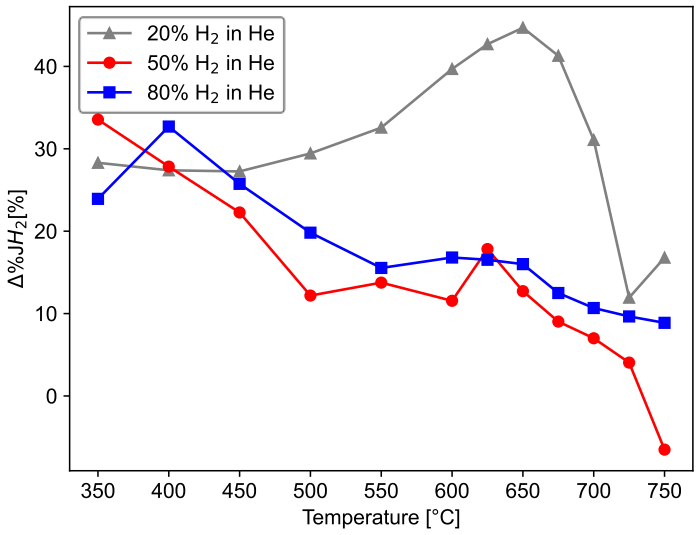

Figure 64 percent difference in permeation (J_{H2}) between freeze casting and tape casting membrane, as a function of temperature and feed stream composition (20, 50, 80% H_2 in He, %vol).

Due to natural variability of permeation results the scatter plot in Figure 64 might have difficult interpretation, and due to this reason average $\Delta\%J_{H_2}$ is reported in Table 28

Feed composition	**Average $\Delta\%J_{H_2}$ [%]**
20% H_2 in He	31
50% H_2 in He	14
80% H_2 in He	17

Table 28 average percent difference in permeation between freeze casting and tape casting membrane

When average values are confronted, there a clear indication that with 20% H_2 in He the difference is *circa* two times the value encountered with feed composition 50% H_2 in He and 80% H_2 in He. It is worth reporting the results obtained reversing the configuration of flows, with feed stream flowing on porous layer.

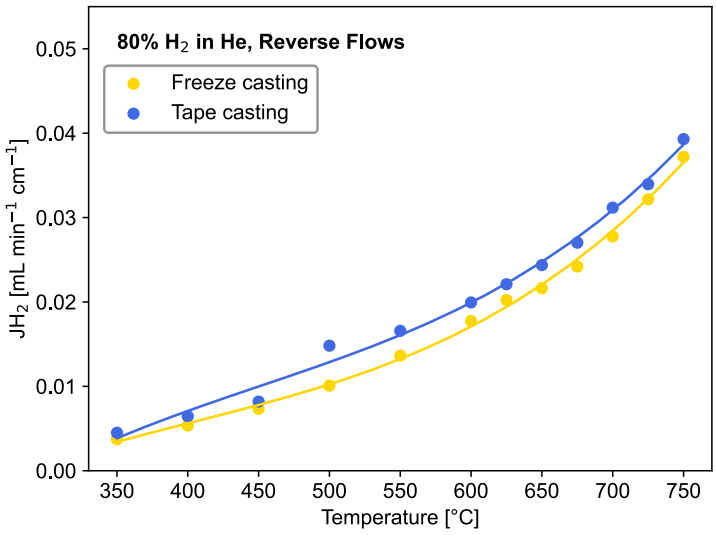

Figure 65 Comparison of permeation performances of asymmetric membranes with tape casting (blue) and freeze casting (yellow) as a function of temperature and employing reverse flows configuration (feed stream flowing on porous layer).

As calculated for standard flow configuration, the average $\Delta\%J_{H_2}$ was calculated and it is reported to be 13%. As previously reported by Schulze-Küppers *et al.*[240], the presence of discordant difference in permeation might be related to concentration polarization inside the support. It was reported that when the concentration of H_2 in the feed streams increases, if reverse configuration is employed (feed stream flowing on porous layer), the effect of mass transfer over membrane driving force become less relevant. Unfortunately, the dataset presented in this case is missing lower H_2 concentration with reverse flow configuration due to mechanical failure of tape casting membrane. Nevertheless, some qualitative evaluation can be still done. If one observes the results obtained with standard flow configuration (feed stream flowing on dense layer), there a stable lower permeation performance for the freeze casting membrane. This difference is more pronounced at lower H_2 feed composition but remains more or less similar for more concentrated H_2 feed (Table 28). Directly linking this to H_2 mass transfer limitation is not applicable in this case, as H_2 flows on the dense side. A similar value in average $\Delta\%J_{H_2}$ is observed with the reverse flow configuration. It could be said that the main cause of decreased permeation for freeze casting membrane is probably due to the thickness of the dense active layer. Once again, extensive membrane microstructural characterization is necessary for deeper understanding of results, and it will be implemented for future works.

5.0 Conclusions

The primary objective that was pursued in this elaborate was to meticulously establish a well-organized and thoroughly structured investigation on the process of catalyst deposition, with the ultimate aim of gaining a comprehensive understanding of the extent to which modifications can exert influence on the apparent hydrogen permeation. Simultaneously, we sought to assess the impact of various porous layer characteristics on the aforementioned phenomenon, in order to ensure that all pertinent factors that contribute to apparent hydrogen permeation were taken into account and thoroughly scrutinized.

Studied materials were ceramic membranes with composition $BaCe_{0.65}Zr_{0.20}Y_{0.15}O_{3-\delta}$(BCZY) – $Gd_{0.2}Ce_{0.8}O_{2-\delta}$ (GDC), characterized by flat-disk shape. After an initial exploration, the configuration of the membrane was distinguished by an asymmetric architecture, featuring a dense active layer that measured approximately 20 µm in thickness and a porous layer that exhibited variability. The porosity of the membranes was determined by employing two distinct methods of porosity shaping, namely tape casting and freeze casting. A comprehensive examination of the membranes was carried out with alterations made to the following variables: (1) the shapes of porosity, (2) the configurations of streams, (3) the thickness of the porous layer, (4) the Pt catalyst, (5) the temperature, and (6) the composition of the feed stream.

For what concerns tape casting membranes, the impact of temperature, feed composition and catalyst quantity on the process was scrutinized with the aid of humidified streams that were fully saturated at 28°C. This was accomplished by studying three different feed compositions, namely 20%, 50% and 80% H_2 in He (H_2 %vol), across a temperature range of 350 °C to 750 °C. Specifically, the dense side of the membranes was loaded with 0.15 mg cm^{-2} of Platinum, while three distinct quantities of Platinum were tested to enhance the water splitting reaction on the sweep side, which were 0.15, 1.5 and 4.5 mg cm^{-2}. The explanation for the incongruity observed in the quantity of Pt can be attributed to the contribution of permeated hydrogen. To achieve optimal performance, it was necessary to deposit 1.5 mg cm^{-2} of Pt onto the porous layer, which yielded a flux of 0.642 mL $min^{-1}cm^{-2}$ when 80% H_2 in He was employed as the feed. The deposition technique for Pt is significantly influenced by the concentration of the Pt precursor, which in turn leads to variations in the morphology of the catalyst. Particularly, an increased concentration of precursors has been observed to give rise to the formation of Pt agglomerates, which ultimately leads to the production of less effective Pt catalyst particles for the WS reaction when subjected to high temperatures. It was, then tried to optimize the deposition method, using a mixture of acetone and water as drop casting solvent. This revealed a winning composition in reducing the formation of agglomerate, revealing, through SEM analysis, that the dimensions of Pt particles are similar to those obtained previously using 100% H_2O as a drop casting solvent. However, it is worth noting that the SEM analysis did not reveal any incidence of Pt agglomerate. Regarding permeation performance, the findings indicated a distinct improvement of J_{H2} values for the acetone modified membrane, particularly at elevated temperatures (T > 450°C). This empirical evidence was attributed to the dominant influence of Pt morphology on water splitting reaction, which is further pronounced at higher temperatures [3]. It is worth noticing that the use of modified drop casting method provided higher Pt catalyst efficiency, in terms of hydrogen permeation per gram of Pt catalyst.

Despite having previously elucidated this notion on several occasions within this elaborate, the author is compelled to reiterate it once more. It could potentially communicate the sensation of circularity, but for the sake of clarity and scientific rigor it is once more reported. This study has brought to light the discovery that the metallic catalyst, commonly utilized in literature to overcome limitations in surface kinetics, is unequivocally involved in the permeation performance of membranes. This revelation is of paramount importance as it sheds new light on the complex interplay between catalysts and membranes. The implications of this finding are far-reaching, as it has the potential to revolutionize the current understanding of membrane technology and its applications. Furthermore, this research underscores the need for a more comprehensive understanding of the fundamental mechanisms governing the interaction between catalysts and membranes.

For what concerns freeze casting membranes, two major explorations led to positive effects on hydrogen permeation performances: (1) the effect of solvent for Pt deposition, (2) the effect of the porous layer thickness. The first investigation concerned the effect of the drop casting solvent modification. The utilization of a mixture of acetone and water resulted in superior hydrogen permeation at temperatures exceeding 650°C. The hydrogen permeation reached a peak value of 0.26 mL $min^{-1}cm^{-2}$ at 750°C with 50% H_2 in He (%vol). The presence of Acetone in the solvent mixture benefitted the Pt particles, as analysed by means of SEM imaging, resulting in the detection of particles of smaller dimensions also inside the pores, contrary to 100% H_2O. The literature at the time of production of this elaborate did not include any performance description of membrane with porosity shaped with Freeze Casting method, thus comparison is not possible. The subsequent inquiry delved into the impact of the thickness of the porous layer, utilizing two comparable membranes, namely Mbr0.85 and Mbr2.00, which possessed a similar active dense layer as well as a porous layer measuring 0.85 mm and 2.00 mm respectively. The reduction in thickness of the porous layer resulted in a discernible hydrogen apparent permeated flow of 0.33 mL $min^{-1}cm^{-2}$, at a temperature of 750°C, with a gaseous mixture containing 50% H_2 in He (%vol), with both flowing streams being humidified at a temperature of 28°C. This phenomenon was attributed to the Pt-catalysed WS reaction, which occurs at high temperatures and is catalyzed by more concentrated Pt particles in the tri-dimensional porous framework of the thinned membrane. Further studies will be required in the immediate future to gain a more comprehensive understanding of the effect of material key properties on permeation, in order to facilitate more efficient engineering of membrane production with the ultimate objective of enhancing performance.

References

[1] N. A. Al-Mufachi, N. V. Rees, and R. Steinberger-Wilkens, 'Hydrogen selective membranes: A review of palladium-based dense metal membranes', *Renewable and Sustainable Energy Reviews*, vol. 47, pp. 540–551, Jul. 2015, doi: 10.1016/j.rser.2015.03.026.

[2] S. S. Penner, 'Steps toward the hydrogen economy', *Energy*, vol. 31, no. 1, pp. 33–43, Jan. 2006, doi: 10.1016/j.energy.2004.04.060.

[3] D. Montaleone, E. Mercadelli, S. Escolástico, A. Gondolini, J. M. Serra, and A. Sanson, 'All-ceramic asymmetric membranes with superior hydrogen permeation', *J. Mater. Chem. A*, vol. 6, no. 32, pp. 15718–15727, Aug. 2018, doi: 10.1039/C8TA04764B.

[4] U. Nations, 'Global Issue, Population', United Nations. Accessed: Feb. 08, 2023. [Online]. Available: https://www.un.org/en/global-issues/population

[5] H. Ishaq, I. Dincer, and C. Crawford, 'A review on hydrogen production and utilization: Challenges and opportunities', *International Journal of Hydrogen Energy*, vol. 47, no. 62, pp. 26238–26264, Jul. 2022, doi: 10.1016/j.ijhydene.2021.11.149.

[6] M. Roser, H. Ritchie, E. Ortiz-Ospina, and L. Rodés-Guirao, 'World Population Growth', Our World in Data. Accessed: Feb. 08, 2023. [Online]. Available: https://ourworldindata.org/world-population-growth

[7] 'Global direct primary energy consumption', Our World in Data. Accessed: Feb. 08, 2023. [Online]. Available: https://ourworldindata.org/grapher/global-primary-energy

[8] M. Sankir and N. D. Sankir, *Hydrogen Storage Technologies*. John Wiley & Sons, 2018.

[9] A. L. Dicks and D. A. J. Rand, *Fuel Cell Systems Explained*. John Wiley & Sons, 2018.

[10] S. Dutta, 'A review on production, storage of hydrogen and its utilization as an energy resource', *Journal of Industrial and Engineering Chemistry*, vol. 20, no. 4, pp. 1148–1156, Jul. 2014, doi: 10.1016/j.jiec.2013.07.037.

[11] F. Zhang, P. Zhao, M. Niu, and J. Maddy, 'The survey of key technologies in hydrogen energy storage', *International Journal of Hydrogen Energy*, vol. 41, no. 33, pp. 14535–14552, Sep. 2016, doi: 10.1016/j.ijhydene.2016.05.293.

[12] I. Dincer and C. Acar, 'A review on potential use of hydrogen in aviation applications', *International Journal of Sustainable Aviation*, vol. 2, no. 1, pp. 74–100, Jan. 2016, doi: 10.1504/IJSA.2016.076077.

[13] A. K. Singh, S. Singh, and A. Kumar, 'Hydrogen energy future with formic acid: a renewable chemical hydrogen storage system', *Catal. Sci. Technol.*, vol. 6, no. 1, pp. 12–40, Dec. 2015, doi: 10.1039/C5CY01276G.

[14] G. Cipriani *et al.*, 'Perspective on hydrogen energy carrier and its automotive applications', *International Journal of Hydrogen Energy*, vol. 39, no. 16, pp. 8482–8494, May 2014, doi: 10.1016/j.ijhydene.2014.03.174.

[15] M. Gong, D.-Y. Wang, C.-C. Chen, B.-J. Hwang, and H. Dai, 'A mini review on nickel-based electrocatalysts for alkaline hydrogen evolution reaction', *Nano Res.*, vol. 9, no. 1, pp. 28–46, Jan. 2016, doi: 10.1007/s12274-015-0965-x.

[16] Y. Kalinci, A. Hepbasli, and I. Dincer, 'Techno-economic analysis of a stand-alone hybrid renewable energy system with hydrogen production and storage options', *International Journal of Hydrogen Energy*, vol. 40, no. 24, pp. 7652–7664, Jun. 2015, doi: 10.1016/j.ijhydene.2014.10.147.

[17] A. Mostafaeipour *et al.*, 'Evaluating the wind energy potential for hydrogen production: A case study', *International Journal of Hydrogen Energy*, vol. 41, no. 15, pp. 6200–6210, Apr. 2016, doi: 10.1016/j.ijhydene.2016.03.038.

[18] A. Valente, D. Iribarren, and J. Dufour, 'Harmonising the cumulative energy demand of renewable hydrogen for robust comparative life-cycle studies', *Journal of Cleaner Production*, vol. 175, pp. 384–393, Feb. 2018, doi: 10.1016/j.jclepro.2017.12.069.

[19] A. Maroufmashat, M. Fowler, S. Sattari Khavas, A. Elkamel, R. Roshandel, and A. Hajimiragha, 'Mixed integer linear programing based approach for optimal planning and operation of a smart urban energy network to support the hydrogen economy', *International Journal of Hydrogen Energy*, vol. 41, no. 19, pp. 7700–7716, May 2016, doi: 10.1016/j.ijhydene.2015.08.038.

[20] A. Sgobbi, W. Nijs, R. De Miglio, A. Chiodi, M. Gargiulo, and C. Thiel, 'How far away is hydrogen? Its role in the medium and long-term decarbonisation of the European energy system', *International Journal of Hydrogen Energy*, vol. 41, no. 1, pp. 19–35, Jan. 2016, doi: 10.1016/j.ijhydene.2015.09.004.

[21] D. Gielen, F. Boshell, D. Saygin, M. D. Bazilian, N. Wagner, and R. Gorini, 'The role of renewable energy in the global energy transformation', *Energy Strategy Reviews*, vol. 24, pp. 38–50, Apr. 2019, doi: 10.1016/j.esr.2019.01.006.

[22] D. Parra, L. Valverde, F. J. Pino, and M. K. Patel, 'A review on the role, cost and value of hydrogen energy systems for deep decarbonisation', *Renewable and Sustainable Energy Reviews*, vol. 101, pp. 279–294, Mar. 2019, doi: 10.1016/j.rser.2018.11.010.

[23] G. Pleßmann, M. Erdmann, M. Hlusiak, and C. Breyer, 'Global Energy Storage Demand for a 100% Renewable Electricity Supply', *Energy Procedia*, vol. 46, pp. 22–31, 2014, doi: 10.1016/j.egypro.2014.01.154.

[24] P. Colbertaldo, S. B. Agustin, S. Campanari, and J. Brouwer, 'Impact of hydrogen energy storage on California electric power system: Towards 100% renewable electricity', *International Journal of Hydrogen Energy*, vol. 44, no. 19, pp. 9558–9576, Apr. 2019, doi: 10.1016/j.ijhydene.2018.11.062.

[25] M. Boudellal, *Power-to-Gas: Renewable Hydrogen Economy for the Energy Transition*. Walter de Gruyter GmbH & Co KG, 2023.

[26] J. O. Abe, A. P. I. Popoola, E. Ajenifuja, and O. M. Popoola, 'Hydrogen energy, economy and storage: Review and recommendation', *International Journal of Hydrogen Energy*, vol. 44, no. 29, pp. 15072–15086, Jun. 2019, doi: 10.1016/j.ijhydene.2019.04.068.

[27] H. Blanco and A. Faaij, 'A review at the role of storage in energy systems with a focus on Power to Gas and long-term storage', *Renewable and Sustainable Energy Reviews*, vol. 81, pp. 1049–1086, Jan. 2018, doi: 10.1016/j.rser.2017.07.062.

[28] E. Kötter, L. Schneider, F. Sehnke, K. Ohnmeiss, and R. Schröer, 'The future electric power system: Impact of Power-to-Gas by interacting with other renewable energy components', *Journal of Energy Storage*, vol. 5, pp. 113–119, Feb. 2016, doi: 10.1016/j.est.2015.11.012.

[29] I. Vincent and D. Bessarabov, 'Low cost hydrogen production by anion exchange membrane electrolysis: A review', *Renewable and Sustainable Energy Reviews*, vol. 81, pp. 1690–1704, Jan. 2018, doi: 10.1016/j.rser.2017.05.258.

[30] J. Liu, X. Duan, Z. Yuan, Q. Liu, and Q. Tang, 'Experimental study on the performance, combustion and emission characteristics of a high compression ratio heavy-duty spark-ignition engine fuelled with liquefied methane gas and hydrogen blend', *Applied Thermal Engineering*, vol. 124, pp. 585–594, Sep. 2017, doi: 10.1016/j.applthermaleng.2017.06.067.

[31] D. Parra, X. Zhang, C. Bauer, and M. K. Patel, 'An integrated techno-economic and life cycle environmental assessment of power-to-gas systems', *Applied Energy*, vol. 193, pp. 440–454, May 2017, doi: 10.1016/j.apenergy.2017.02.063.

[32] S. A. Sherif, F. Barbir, and T. N. Veziroglu, 'Wind energy and the hydrogen economy—review of the technology', *Solar Energy*, vol. 78, no. 5, pp. 647–660, May 2005, doi: 10.1016/j.solener.2005.01.002.

[33] C. He, R. Yu, H. Sun, and Z. Chen, 'Lightweight multilayer composite structure for hydrogen storage tank', *International Journal of Hydrogen Energy*, vol. 41, no. 35, pp. 15812–15816, Sep. 2016, doi: 10.1016/j.ijhydene.2016.04.184.

[34] D. Halm, F. Fouillen, E. Lainé, M. Gueguen, D. Bertheau, and T. van Eekelen, 'Composite pressure vessels for hydrogen storage in fire conditions: Fire tests and burst simulation', *International Journal of Hydrogen Energy*, vol. 42, no. 31, pp. 20056–20070, Aug. 2017, doi: 10.1016/j.ijhydene.2017.06.088.

[35] W. Lanz, 'Hydrogen Properties', *Hydrogen Fuel*, 2001.

[36] 'Hydrogen Europe - In a Nutshell', Hydrogen Europe. Accessed: Feb. 13, 2023. [Online]. Available: https://hydrogeneurope.eu/in-a-nutshell/

[37] 'The hydrogen colour spectrum| National Grid Group'. Accessed: Sep. 26, 2023. [Online]. Available: https://www.nationalgrid.com/stories/energy-explained/hydrogen-colour-spectrum

[38] IEA, 'Global hydrogen production by technology in the Net Zero Scenario, 2019-2030', IEA. Accessed: Feb. 13, 2023. [Online]. Available: https://www.iea.org/data-and-statistics/charts/global-hydrogen-production-by-technology-in-the-net-zero-scenario-2019-2030

[39] 'Road map to a US hydrogen economy: reducing emissions and driving growth across the nation.', Fuel Cell & Hydrogen Energy Association. Accessed: Feb. 14, 2023. [Online]. Available: https://www.fchea.org/us-hydrogen-study

[40] A. Demirbas, H. Alidrisi, and M. A. Balubaid, 'API Gravity, Sulfur Content, and Desulfurization of Crude Oil', *Petroleum Science and Technology*, vol. 33, no. 1, pp. 93–101, Jan. 2015, doi: 10.1080/10916466.2014.950383.

[41] K. Jangam, Y.-Y. Chen, L. Qin, and L.-S. Fan, 'Perspectives on reactive separation and removal of hydrogen sulfide', *Chemical Engineering Science: X*, vol. 11, p. 100105, Aug. 2021, doi: 10.1016/j.cesx.2021.100105.

[42] E. L. G. Oliveira, C. A. Grande, and A. E. Rodrigues, 'Methane steam reforming in large pore catalyst', *Chemical Engineering Science*, vol. 65, no. 5, pp. 1539–1550, Mar. 2010, doi: 10.1016/j.ces.2009.10.018.

[43] B. Castro-Dominguez *et al.*, 'Integration of Methane Steam Reforming and Water Gas Shift Reaction in a Pd/Au/Pd-Based Catalytic Membrane Reactor for Process Intensification', *Membranes*, vol. 6, no. 3, Art. no. 3, Sep. 2016, doi: 10.3390/membranes6030044.

[44] R. F. Drnevich, '(54) STEAM METHANE REFORMING METHOD', US 7,037,485 B1

[45] Z. Navas-Anguita, D. García-Gusano, J. Dufour, and D. Iribarren, 'Revisiting the role of steam methane reforming with CO2 capture and storage for long-term hydrogen production', *Science of The Total Environment*, vol. 771, p. 145432, Jun. 2021, doi: 10.1016/j.scitotenv.2021.145432.

[46] M. Al-Zareer, I. Dincer, and M. A. Rosen, 'Analysis and assessment of a hydrogen production plant consisting of coal gasification, thermochemical water decomposition and hydrogen compression systems', *Energy Conversion and Management*, vol. 157, pp. 600–618, Feb. 2018, doi: 10.1016/j.enconman.2017.11.047.

[47] T. Grube and D. Stolten, 'Electromobility with fuel cells and batteries: Advantages for the use of hydrogen', *BWK- Energie-Fachmagazin*, vol. 62, no. 4, pp. S16–S17, 2010.

[48] A. Mohammadi and M. Mehrpooya, 'A comprehensive review on coupling different types of electrolyzer to renewable energy sources', *Energy*, vol. 158, pp. 632–655, Sep. 2018, doi: 10.1016/j.energy.2018.06.073.

[49] K. E. Ayers *et al.*, 'Research Advances towards Low Cost, High Efficiency PEM Electrolysis', *ECS Trans.*, vol. 33, no. 1, p. 3, Oct. 2010, doi: 10.1149/1.3484496.

[50] P. Moçoteguy and A. Brisse, 'A review and comprehensive analysis of degradation mechanisms of solid oxide electrolysis cells', *International Journal of Hydrogen Energy*, vol. 38, no. 36, pp. 15887–15902, Dec. 2013, doi: 10.1016/j.ijhydene.2013.09.045.

[51] M. A. Laguna-Bercero, 'Recent advances in high temperature electrolysis using solid oxide fuel cells: A review', *Journal of Power Sources*, vol. 203, pp. 4–16, Apr. 2012, doi: 10.1016/j.jpowsour.2011.12.019.

[52] R. Ramachandran, 'An overview of industrial uses of hydrogen', *International Journal of Hydrogen Energy*, vol. 23, no. 7, pp. 593–598, Jul. 1998, doi: 10.1016/S0360-3199(97)00112-2.

[53] T. A. Czuppon, S. A. Knez, and D. S. Newsome, *Kirk-Otkmer Encyclopedia of Chemical Technology.*, 5° edizione (12 marzo 2007). Wiley-Interscience.

[54] A. Dehghani, H. Bridjanian, and A. Farshi, 'Selection Separation Method for Hydrogen and Light Hydrocarbons Gases from Waste-Gas Streams of a Petroleum Refinery', *Petroleum Science and Technology*, vol. 30, no. 21, pp. 2196–2207, Nov. 2012, doi: 10.1080/10916466.2010.499408.

[55] A. Julbe and M. Drobek, 'Zeolite X: Type', in *Encyclopedia of Membranes*, E. Drioli and L. Giorno, Eds., Berlin, Heidelberg: Springer, 2015, pp. 1–2. doi: 10.1007/978-3-642-40872-4_607-1.

[56] M. W. Ackley and M. S. A. Baksh, 'Pressure Swing Adsorption Process For the Production of Hydrogen', US 6,340,382 B1

[57] W. H. Isalski, *Separation of Gases*. Clarendon Press, 1989.

[58] F. P. Wilcher, G. Q. Miller, and M. J. Mitariten, 'Technologies for the separation and recovery of hydrogen from refinery streams', Art. no. CONF-950801-, Dec. 1995, Accessed: Feb. 16, 2023. [Online]. Available: https://www.osti.gov/biblio/215030

[59] G. Q. Miller, 'NPRA Annual Meeting', presented at the NPRA Annual Meeting, San Francisco CA, Mar. 1989, pp. 1–35.

[60] W. Wolf, 'Optimizing thermal plants for cryogenic process', *OGJ*, vol. 80, pp. 88–91, 1976.

[61] Z. Tao, L. Yan, J. Qiao, B. Wang, L. Zhang, and J. Zhang, 'A review of advanced proton-conducting materials for hydrogen separation', *Progress in Materials Science*, vol. 74, pp. 1–50, Oct. 2015, doi: 10.1016/j.pmatsci.2015.04.002.

[62] K. Scott, 'MEMBRANE MATERIALS, PREPARATION AND CHARACTERISATION', in *Handbook of Industrial Membranes*, K. Scott, Ed., Amsterdam: Elsevier Science, 1995, pp. 187–269. doi: 10.1016/B978-185617233-2/50005-2.

[63] J. D. Perry, K. Nagai, and W. J. Koros, 'Polymer Membranes for Hydrogen Separations', *MRS Bulletin*, vol. 31, no. 10, pp. 745–749, Oct. 2006, doi: 10.1557/mrs2006.187.

[64] W. J. Koros, Y. H. Ma, and T. Shimidzu, 'Terminology for membranes and membrane processes (IUPAC Recommendations 1996)', *Pure and Applied Chemistry*, vol. 68, no. 7, pp. 1479–1489, Jan. 1996, doi: 10.1351/pac199668071479.

[65] A. Iulianelli and A. Basile, 'Special issue on "Hydrogen separation/purification via membrane technology"', *International Journal of Hydrogen Energy*, vol. 45, no. 12, p. 7265, Mar. 2020, doi: 10.1016/j.ijhydene.2019.10.054.

[66] G. Bernardo, T. Araújo, T. da Silva Lopes, J. Sousa, and A. Mendes, 'Recent advances in membrane technologies for hydrogen purification', *International Journal of Hydrogen Energy*, vol. 45, no. 12, pp. 7313–7338, Mar. 2020, doi: 10.1016/j.ijhydene.2019.06.162.

[67] E. Drioli, A. Brunetti, G. D. Profio, and G. Barbieri, 'Process intensification strategies and membrane engineering', *Green Chem.*, vol. 14, no. 6, pp. 1561–1572, Jun. 2012, doi: 10.1039/C2GC16668B.

[68] C.-H. Kim, J.-Y. Han, H. Lim, K.-Y. Lee, and S.-K. Ryi, 'Methane steam reforming using a membrane reactor equipped with a Pd-based composite membrane for effective hydrogen production', *International Journal of Hydrogen Energy*, vol. 43, no. 11, pp. 5863–5872, Mar. 2018, doi: 10.1016/j.ijhydene.2017.10.054.

[69] B. Cifuentes, F. Bustamante, J. A. Conesa, L. F. Córdoba, and M. Cobo, 'Fuel-cell grade hydrogen production by coupling steam reforming of ethanol and carbon monoxide removal', *International Journal of Hydrogen Energy*, vol. 43, no. 36, pp. 17216–17229, Sep. 2018, doi: 10.1016/j.ijhydene.2018.07.139.

[70] A. Iulianelli *et al.*, 'From bioethanol exploitation to high grade hydrogen generation: Steam reforming promoted by a Co-Pt catalyst in a Pd-based membrane reactor', *Renewable Energy*, vol. 119, pp. 834–843, Apr. 2018, doi: 10.1016/j.renene.2017.10.050.

[71] K. E. Lamb, M. D. Dolan, and D. F. Kennedy, 'Ammonia for hydrogen storage; A review of catalytic ammonia decomposition and hydrogen separation and purification', *International Journal of Hydrogen Energy*, vol. 44, no. 7, pp. 3580–3593, Feb. 2019, doi: 10.1016/j.ijhydene.2018.12.024.

[72] P. Nikolaidis and A. Poullikkas, 'A comparative overview of hydrogen production processes', *Renewable and Sustainable Energy Reviews*, vol. 67, pp. 597–611, Jan. 2017, doi: 10.1016/j.rser.2016.09.044.

[73] Y. Shirasaki and I. Yasuda, '12 - Membrane reactor for hydrogen production from natural gas at the Tokyo Gas Company: a case study', in *Handbook of Membrane Reactors*, vol. 2, A. Basile, Ed., in Woodhead Publishing Series in Energy, vol. 2. , Woodhead Publishing, 2013, pp. 487–507. doi: 10.1533/9780857097347.2.487.

[74] M. Voldsund, K. Jordal, and R. Anantharaman, 'Hydrogen production with CO2 capture', *International Journal of Hydrogen Energy*, vol. 41, no. 9, pp. 4969–4992, Mar. 2016, doi: 10.1016/j.ijhydene.2016.01.009.

[75] H. P. Hsieh, 'General Characteristics of Inorganic Membranes', in *Inorganic Membranes Synthesis, Characteristics and Applications*, R. R. Bhave, Ed., Dordrecht: Springer Netherlands, 1991, pp. 64–94. doi: 10.1007/978-94-011-6547-1_3.

[76] A. F. Ismail and L. I. B. David, 'A review on the latest development of carbon membranes for gas separation', *Journal of Membrane Science*, vol. 193, no. 1, pp. 1–18, Oct. 2001, doi: 10.1016/S0376-7388(01)00510-5.

[77] L. Shao, B. T. Low, T.-S. Chung, and A. R. Greenberg, 'Polymeric membranes for the hydrogen economy: Contemporary approaches and prospects for the future', *Journal of Membrane Science*, vol. 327, no. 1, pp. 18–31, Feb. 2009, doi: 10.1016/j.memsci.2008.11.019.

[78] T. Graham, 'On the molecular mobility of gasses', *J. Chem. Soc. Lond.*, vol. 17, pp. 334–339, 1864.

[79] K. Ghosal and B. D. Freeman, 'Gas separation using polymer membranes: an overview', *Polymers for Advanced Technologies*, vol. 5, no. 11, pp. 673–697, 1994, doi: 10.1002/pat.1994.220051102.

[80] L. M. Robeson, W. F. Burgoyne, M. Langsam, A. C. Savoca, and C. F. Tien, 'High performance polymers for membrane separation', *Polymer*, vol. 35, no. 23, pp. 4970–4978, Nov. 1994, doi: 10.1016/0032-3861(94)90651-3.

[81] A. J. Burggraaf and L. Cot, *Fundamentals of Inorganic Membrane Science and Technology, Volume 4 - 1st Edition*. 1996. Accessed: Feb. 27, 2023. [Online]. Available: https://www.elsevier.com/books/fundamentals-of-inorganic-membrane-science-and-technology/burggraaf/978-0-444-81877-5

[82] P. F. Lito, S. P. Cardoso, A. E. Rodrigues, and C. M. Silva, 'Kinetic Modeling of Pure and Multicomponent Gas Permeation Through Microporous Membranes: Diffusion Mechanisms and Influence of Isotherm Type', *Separation & Purification Reviews*, vol. 44, no. 4, pp. 283–307, Oct. 2015, doi: 10.1080/15422119.2014.908918.

[83] R. Krishna, 'Problems and pitfalls in the use of the fick formulation for intraparticle diffusion', *Chemical Engineering Science*, vol. 48, no. 5, pp. 845–861, Jan. 1993, doi: 10.1016/0009-2509(93)80324-J.

[84] N. W. Ockwig and T. M. Nenoff, 'Membranes for Hydrogen Separation', *Chem. Rev.*, vol. 110, no. 4, pp. 2573–2574, Apr. 2010, doi: 10.1021/cr078108l.

[85] S. Smart, J. Beltramini, J. C. Diniz da Costa, S. P. Katikaneni, and T. Pham, '9 - Microporous silica membranes: fundamentals and applications in membrane reactors for hydrogen separation', in *Handbook of Membrane Reactors*, vol. 1, A. Basile, Ed., in Woodhead Publishing Series in Energy, vol. 1. , Woodhead Publishing, 2013, pp. 337–369. doi: 10.1533/9780857097330.2.337.

[86] A. Ayral, A. Julbe, V. Rouessac, S. Roualdes, and J. Durand, 'Microporous Silica Membrane: Basic Principles and Recent Advances', *Membrane Science and Technology*, vol. 13, pp. 33–79, Dec. 2008, doi: 10.1016/S0927-5193(07)13002-3.

[87] M. C. Duke, J. C. D. da Costa, D. D. Do, P. G. Gray, and G. Q. Lu, 'Hydrothermally Robust Molecular Sieve Silica for Wet Gas Separation', *Advanced Functional Materials*, vol. 16, no. 9, pp. 1215–1220, 2006, doi: 10.1002/adfm.200500456.

[88] C. Algieri, G. Barbieri, and E. Drioli, *Zeolite Membranes for Gas Separations*. 2011. Accessed: Feb. 28, 2023. [Online]. Available: https://books.rsc.org/books/edited-volume/1766/chapter/1411984/Zeolite-Membranes-for-Gas-Separations

[89] S. P. Cardoso, I. S. Azenha, Z. Lin, I. Portugal, A. E. Rodrigues, and C. M. Silva, 'Inorganic Membranes for Hydrogen Separation', *Separation & Purification Reviews*, vol. 47, no. 3, pp. 229–266, Jul. 2018, doi: 10.1080/15422119.2017.1383917.

[90] A. F. Ismail, D. Rana, T. Matsuura, and H. C. Foley, *Carbon-based Membranes for Separation Processes*. Springer Science & Business Media, 2011.

[91] S. Lagorsse, M. C. Campo, F. D. Magalhães, and A. Mendes, 'Water adsorption on carbon molecular sieve membranes: Experimental data and isotherm model', *Carbon*, vol. 43, no. 13, pp. 2769–2779, Nov. 2005, doi: 10.1016/j.carbon.2005.05.042.

[92] B. Zornoza, C. Casado, and A. Navajas, 'Chapter 11 - Advances in Hydrogen Separation and Purification with Membrane Technology', in *Renewable Hydrogen Technologies*, L. M. Gandía, G. Arzamendi, and P. M. Diéguez, Eds., Amsterdam: Elsevier, 2013, pp. 245–268. doi: 10.1016/B978-0-444-56352-1.00011-8.

[93] T. L. Ward and T. Dao, 'Model of hydrogen permeation behavior in palladium membranes', *Journal of Membrane Science*, vol. 153, no. 2, pp. 211–231, Feb. 1999, doi: 10.1016/S0376-7388(98)00256-7.

[94] A. Caravella, G. Barbieri, and E. Drioli, 'Modelling and simulation of hydrogen permeation through supported Pd-alloy membranes with a multicomponent approach', *Chemical Engineering Science*, vol. 63, no. 8, pp. 2149–2160, Apr. 2008, doi: 10.1016/j.ces.2008.01.009.

[95] A. Basile, F. Gallucci, and S. Tosti, 'Synthesis, Characterization, and Applications of Palladium Membranes', in *Membrane Science and Technology*, vol. 13, in Inorganic Membranes: Synthesis, Characterization and Applications, vol. 13. , Elsevier, 2008, pp. 255–323. doi: 10.1016/S0927-5193(07)13008-4.

[96] B. Morreale *et al.*, 'Gasification and Associated Degradation Mechanisms Applicable to Dense Metal Hydrogen Membranes', in *Inorganic Membranes for Energy and Environmental Applications*, A. C. Bose, Ed., New York, NY: Springer, 2009, pp. 173–201. doi: 10.1007/978-0-387-34526-0_10.

[97] A. L. Athayde, R. W. Baker, and P. Nguyen, 'Metal composite membranes for hydrogen separation', *Journal of Membrane Science*, vol. 94, no. 1, pp. 299–311, Sep. 1994, doi: 10.1016/0376-7388(94)00042-5.

[98] S. Tosti, R. Borelli, F. Borgognoni, P. Favuzza, C. Rizzello, and P. Tarquini, 'Study of a dense metal membrane reactor for hydrogen separation from hydroiodic acid decomposition', *International Journal of Hydrogen Energy*, vol. 33, no. 19, pp. 5106–5114, Oct. 2008, doi: 10.1016/j.ijhydene.2008.07.030.

[99] B. Ernst, S. Haag, and M. Burgard, 'Permselectivity of a nickel/ceramic composite membrane at elevated temperatures: A new prospect in hydrogen separation?', *Journal of Membrane Science*, vol. 288, no. 1, pp. 208–217, Feb. 2007, doi: 10.1016/j.memsci.2006.11.017.

[100] M. Wang, J. Song, X. Wu, X. Tan, B. Meng, and S. Liu, 'Metallic nickel hollow fiber membranes for hydrogen separation at high temperatures', *Journal of Membrane Science*, vol. 509, pp. 156–163, Jul. 2016, doi: 10.1016/j.memsci.2016.02.025.

[101] S. I. Jeon and J. H. Park, 'Hydrogen permeation properties of Pd-coated V89.8Cr10Y0.2 alloy membrane using WGS reaction gases', *International Journal of Hydrogen Energy*, vol. 38, no. 14, pp. 6085–6091, May 2013, doi: 10.1016/j.ijhydene.2013.01.172.

[102] S. I. Jeon, J. H. Park, E. Magnone, Y. T. Lee, and E. Fleury, 'Hydrogen permeation of Pd-coated V90Al10 alloy membranes at different pressures in the presence and absence of carbon dioxide', *Current Applied Physics*, vol. 12, no. 2, pp. 394–400, Mar. 2012, doi: 10.1016/j.cap.2011.07.036.

[103] E. Fleury, J.-Y. Suh, D. Kim, C. H. Jeong, and J. H. Park, 'Hydrogen permeation characteristics of rolled V85Al10Co5 alloys', *Current Applied Physics*, vol. 12, no. 4, pp. 1131–1138, Jul. 2012, doi: 10.1016/j.cap.2012.02.007.

[104] A. F. Sammells and M. V. Mundschau, 'Nonporous Inorganic Membranes', p. 292.

[105] Korjus, 'Eesti: perovskite', commons.wikimedia.org. Accessed: Apr. 14, 2023. [Online]. Available: https://commons.wikimedia.org/wiki/File:Perovskite_ABO3.jpg

[106] H. D. Megaw, 'Crystal structure of double oxides of the perovskite type', *Proc. Phys. Soc.*, vol. 58, no. 2, p. 133, Mar. 1946, doi: 10.1088/0959-5309/58/2/301.

[107] A. Esquirol, J. Kilner, and N. Brandon, 'Oxygen transport in La0.6Sr0.4Co0.2Fe0.8O3−δ/Ce0.8Ge0.2O2−x composite cathode for IT-SOFCs', *Solid State Ionics*, vol. 175, no. 1, pp. 63–67, Nov. 2004, doi: 10.1016/j.ssi.2004.09.013.

[108] H. Uchida, N. Maeda, and H. Iwahara, 'Relation between proton and hole conduction in SrCeO3-based solid electrolytes under water-containing atmospheres at high temperatures', *Solid State Ionics*, vol. 11, no. 2, pp. 117–124, Oct. 1983, doi: 10.1016/0167-2738(83)90048-6.

[109] H. Iwahara, T. Yajima, T. Hibino, and H. Ushida, 'Performance of Solid Oxide Fuel Cell Using Proton and Oxide Ion Mixed Conductors Based on BaCe1 − x Sm x O 3 − α', *J. Electrochem. Soc.*, vol. 140, no. 6, p. 1687, Jun. 1993, doi: 10.1149/1.2221624.

[110] N. Bonanos, K. S. Knight, and B. Ellis, 'Perovskite solid electrolytes: Structure, transport properties and fuel cell applications', *Solid State Ionics*, vol. 79, pp. 161–170, Jul. 1995, doi: 10.1016/0167-2738(95)00056-C.

[111] H. Iwahara, 'High temperature proton conductors based on perovskite-type oxides', in *Proton Conductors: Solids, Membranes and Gels - Materials and Devices*, P. Colomban, Ed., in Chemistry of Solid State Materials. , Cambridge: Cambridge University Press, 1992, pp. 122–137. doi: 10.1017/CBO9780511524806.009.

[112] S. Stotz and C. Wagner, 'Die Löslichkeit von Wasserdampf und Wasserstoff in festen Oxiden', *Berichte der Bunsengesellschaft für physikalische Chemie*, vol. 70, no. 8, pp. 781–788, 1966, doi: 10.1002/bbpc.19660700804.

[113] T. Norby and Y. Larring, 'Concentration and transport of protons in oxides', *Current Opinion in Solid State and Materials Science*, vol. 2, no. 5, pp. 593–599, Oct. 1997, doi: 10.1016/S1359-0286(97)80051-4.

[114] Y. Liu, X. Tan, and K. Li, 'Mixed Conducting Ceramics for Catalytic Membrane Processing', *Catalysis Reviews*, vol. 48, no. 2, pp. 145–198, Jul. 2006, doi: 10.1080/01614940600631348.

[115] E. C. C. de Souza and R. Muccillo, 'Properties and applications of perovskite proton conductors', *Mat. Res.*, vol. 13, pp. 385–394, Sep. 2010, doi: 10.1590/S1516-14392010000300018.

[116] K.-D. Kreuer, A. Fuchs, and J. Maier, 'HD isotope effect of proton conductivity and proton conduction mechanism in oxides', *Solid State Ionics*, vol. 77, pp. 157–162, Apr. 1995, doi: 10.1016/0167-2738(94)00265-T.

[117] K. H. Ryu and S. M. Haile, 'Chemical stability and proton conductivity of doped BaCeO3–BaZrO3 solid solutions', *Solid State Ionics*, vol. 125, no. 1, pp. 355–367, Oct. 1999, doi: 10.1016/S0167-2738(99)00196-4.

[118] R. Kannan, K. Singh, S. Gill, T. Fürstenhaupt, and V. Thangadurai, 'Chemically Stable Proton Conducting Doped BaCeO3 -No More Fear to SOFC Wastes', *Sci Rep*, vol. 3, no. 1, Art. no. 1, Jul. 2013, doi: 10.1038/srep02138.

[119] S. Yamaguchi and N. Yamada, 'Thermal lattice expansion behavior of Yb-doped BaCeO3', *Solid State Ionics*, vol. 162–163, pp. 23–29, Sep. 2003, doi: 10.1016/S0167-2738(03)00249-2.

[120] K. Künstler, H.-J. Lang, A. Maiwald, and G. Tomandl, 'Synthesis, structure and electrochemical properties of In-doped BaCeO3', *Solid State Ionics*, vol. 107, no. 3, pp. 221–229, Apr. 1998, doi: 10.1016/S0167-2738(97)00542-0.

[121] J.-X. Wang *et al.*, 'Structure, thermal expansion and transport properties of BaCe1−xEuxO3−δ oxides', *Materials Chemistry and Physics*, vol. 86, no. 1, pp. 150–155, Jul. 2004, doi: 10.1016/j.matchemphys.2004.02.021.

[122] Z. Wu and M. Liu, 'Stability of BaCe0.8Gd0.2 O 3 in a H 2 O -Containing Atmosphere at Intermediate Temperatures', *J. Electrochem. Soc.*, vol. 144, no. 6, p. 2170, Jun. 1997, doi: 10.1149/1.1837759.

[123] F. L. Chen, O. T. Sørensen, G. Y. Meng, and D. K. Peng, 'Preparation of Nd-doped BaCeO3 proton-conducting ceramic and its electrical properties in different atmospheres', *Journal of the European Ceramic Society*, vol. 18, no. 10, pp. 1389–1395, Jan. 1998, doi: 10.1016/S0955-2219(97)00136-2.

[124] A. N. Virkar and H. S. Maiti, 'Oxygen ion conduction in pure and yttria-doped barium cerate', *Journal of Power Sources*, vol. 14, no. 4, pp. 295–303, Apr. 1985, doi: 10.1016/0378-7753(85)80045-8.

[125] P. Ranran, W. Yan, Y. Lizhai, and M. Zongqiang, 'Electrochemical properties of intermediate-temperature SOFCs based on proton conducting Sm-doped BaCeO3 electrolyte thin film', *Solid State Ionics*, vol. 177, no. 3, pp. 389–393, Jan. 2006, doi: 10.1016/j.ssi.2005.11.020.

[126] F. Zhao, Q. Liu, S. Wang, K. Brinkman, and F. Chen, 'Synthesis and characterization of BaIn0.3−xYxCe0.7O3−δ (x = 0, 0.1, 0.2, 0.3) proton conductors', *International Journal of Hydrogen Energy*, vol. 35, no. 9, pp. 4258–4263, May 2010, doi: 10.1016/j.ijhydene.2010.02.080.

[127] K. D. Kreuer, 'Proton-Conducting Oxides', *Annual Review of Materials Research*, vol. 33, no. 1, pp. 333–359, 2003, doi: 10.1146/annurev.matsci.33.022802.091825.

[128] C. Zhang, H. Zhao, N. Xu, X. Li, and N. Chen, 'Influence of ZnO addition on the properties of high temperature proton conductor Ba1.03Ce0.5Zr0.4Y0.1O3−δ synthesized via citrate–nitrate

method', *International Journal of Hydrogen Energy*, vol. 34, no. 6, pp. 2739–2746, Mar. 2009, doi: 10.1016/j.ijhydene.2009.01.061.

[129] E. Rebollo *et al.*, 'Exceptional hydrogen permeation of all-ceramic composite robust membranes based on BaCe 0.65 Zr 0.20 Y 0.15 O 3−δ and Y- or Gd-doped ceria', *Energy & Environmental Science*, vol. 8, no. 12, pp. 3675–3686, 2015, doi: 10.1039/C5EE01793A.

[130] S.-J. Song, E. D. Wachsman, J. Rhodes, S. E. Dorris, and U. Balachandran, 'Numerical modeling of hydrogen permeation in chemical potential gradients', *Solid State Ionics*, vol. 164, no. 1, pp. 107–116, Oct. 2003, doi: 10.1016/j.ssi.2003.08.033.

[131] N. Bonanos, 'Transport properties and conduction mechanism in high-temperature protonic conductors', *Solid State Ionics*, vol. 53–56, pp. 967–974, Jul. 1992, doi: 10.1016/0167-2738(92)90278-W.

[132] C.-S. Tu, R. R. Chien, V. H. Schmidt, S.-C. Lee, C.-C. Huang, and C.-L. Tsai, 'Thermal stability of Ba(Zr0.8−xCexY0.2)O2.9 ceramics in carbon dioxide', *Journal of Applied Physics*, vol. 105, no. 10, p. 103504, May 2009, doi: 10.1063/1.3117835.

[133] C. Zuo *et al.*, 'Hydrogen Permeation and Chemical Stability of Cermet [Ni – Ba (Zr0.8 − x Ce x Y0.2) O3] Membranes', *Electrochem. Solid-State Lett.*, vol. 8, no. 12, p. J35, Oct. 2005, doi: 10.1149/1.2081807.

[134] R. Kannan, S. Gill, N. Maffei, and V. Thangadurai, 'BaCe0.85-xZrxSm0.15O3-δ (0.01 < x < 0.3) (BCZS): Effect of Zr Content in BCZS on Chemical Stability in CO2 and H2O Vapor, and Proton Conductivity', *J. Electrochem. Soc.*, vol. 160, no. 1, p. F18, Nov. 2012, doi: 10.1149/2.029301jes.

[135] X. Tan, X. Tan, N. Yang, B. Meng, K. Zhang, and S. Liu, 'High performance BaCe0.8Y0.2O3−a (BCY) hollow fibre membranes for hydrogen permeation', *Ceramics International*, vol. 40, no. 2, pp. 3131–3138, Mar. 2014, doi: 10.1016/j.ceramint.2013.09.132.

[136] M. Cai, S. Liu, K. Efimov, J. Caro, A. Feldhoff, and H. Wang, 'Preparation and hydrogen permeation of BaCe0.95Nd0.05O3-δ membranes', *Journal of Membrane Science*, vol. 343, no. 1–2, pp. 90–96, 2009, doi: 10.1016/j.memsci.2009.07.011.

[137] H. Zhang and B. A. Wilhite, 'Electrical conduction and hydrogen permeation investigation on iron-doped barium zirconate membrane', *Journal of Membrane Science*, vol. 512, pp. 104–110, Aug. 2016, doi: 10.1016/j.memsci.2016.04.001.

[138] S. Escolástico, M. Ivanova, C. Solís, S. Roitsch, W. A. Meulenberg, and J. M. Serra, 'Improvement of transport properties and hydrogen permeation of chemically-stable proton - conducting oxides based on the system BaZr 1-x-y Y x M y O 3-δ', *RSC Advances*, vol. 2, no. 11, pp. 4932–4943, 2012, doi: 10.1039/C2RA20214J.

[139] S.-J. Song, E. D. Wachsman, J. Rhodes, S. E. Dorris, and U. Balachandran, 'Hydrogen permeability of SrCe1−xMxO3−δ (x=0.05, M=Eu, Sm)', *Solid State Ionics*, vol. 167, no. 1, pp. 99–105, Feb. 2004, doi: 10.1016/j.ssi.2003.12.010.

[140] X. Wei, J. Kniep, and Y. S. Lin, 'Hydrogen permeation through terbium doped strontium cerate membranes enabled by presence of reducing gas in the downstream', *Journal of Membrane Science*, vol. 345, no. 1, pp. 201–206, Dec. 2009, doi: 10.1016/j.memsci.2009.08.041.

[141] X. Qi and Y. S. Lin, 'Electrical conduction and hydrogen permeation through mixed proton–electron conducting strontium cerate membranes', *Solid State Ionics*, vol. 130, no. 1, pp. 149–156, May 2000, doi: 10.1016/S0167-2738(00)00281-2.

[142] J. Kniep and Y. S. Lin, 'Effect of Zirconium Doping on Hydrogen Permeation through Strontium Cerate Membranes', *Ind. Eng. Chem. Res.*, vol. 49, no. 6, pp. 2768–2774, Mar. 2010, doi: 10.1021/ie9015182.

[143] M. Matsuka, R. D. Braddock, H. Matsumoto, T. Sakai, I. E. Agranovski, and T. Ishihara, 'Experimental and theoretical studies of hydrogen permeation for doped strontium cerates', *Solid State Ionics*, vol. 181, no. 29, pp. 1328–1335, Sep. 2010, doi: 10.1016/j.ssi.2010.07.002.

[144] W. H. Yuan, L. L. Mao, and L. Li, 'Novel SrCe0.75Zr0.20Tm0.05O3−δ membrane for hydrogen separation', *Chinese Chemical Letters*, vol. 21, no. 3, pp. 369–372, Mar. 2010, doi: 10.1016/j.cclet.2009.11.002.

[145] W. Yuan, C. Xiao, and L. Li, 'Hydrogen permeation and chemical stability of In-doped SrCe0.95Tm0.05O3−δ membranes', *Journal of Alloys and Compounds*, vol. 616, pp. 142–147, Dec. 2014, doi: 10.1016/j.jallcom.2014.07.050.

[146] S. Escolástico, C. Solís, T. Scherb, G. Schumacher, and J. M. Serra, 'Hydrogen separation in La5.5WO11.25−δ membranes', *Journal of Membrane Science*, vol. 444, pp. 276–284, Oct. 2013, doi: 10.1016/j.memsci.2013.05.005.

[147] E. Vøllestad, C. K. Vigen, A. Magrasó, and R. Haugsrud, 'Hydrogen permeation characteristics of La27Mo1.5W3.5O55.5', *Journal of Membrane Science*, vol. 461, pp. 81–88, Jul. 2014, doi: 10.1016/j.memsci.2014.03.011.

[148] Y. Chen, S. Cheng, L. Chen, Y. Wei, P. J. Ashman, and H. Wang, 'Niobium and molybdenum co-doped La5.5WO11.25− membrane with improved hydrogen permeability', *Journal of Membrane Science*, vol. 510, pp. 155–163, Jul. 2016, doi: 10.1016/j.memsci.2016.02.065.

[149] S. Escolástico, J. Seeger, S. Roitsch, M. Ivanova, W. Meulenberg, and J. Serra, 'Enhanced H-2 Separation through Mixed Proton-Electron Conducting Membranes Based on La5.5W0.8M0.2O11.25-', *ChemSusChem*, vol. 6, Jul. 2013, doi: 10.1002/cssc.201300091.

[150] S. Escolástico, C. Solís, R. Haugsrud, A. Magrasó, and J. M. Serra, 'On the ionic character of H 2 separation through mixed conducting Nd 5.5 W 0.5 Mo 0.5 O 11.25−δ membrane', *International Journal of Hydrogen Energy*, vol. 42, no. 16, pp. 11392–11399, Apr. 2017, doi: 10.1016/j.ijhydene.2017.02.087.

[151] S. S. Hashim, M. R. Somalu, K. S. Loh, S. Liu, W. Zhou, and J. Sunarso, 'Perovskite-based proton conducting membranes for hydrogen separation: A review', *International Journal of Hydrogen Energy*, vol. 43, no. 32, pp. 15281–15305, Aug. 2018, doi: 10.1016/j.ijhydene.2018.06.045.

[152] Y. Wei, J. Xue, W. Fang, Y. Chen, H. Wang, and J. Caro, 'Enhanced stability of Zr-doped Ba(CeTb)O3-δ-Ni cermet membrane for hydrogen separation', *Chemical Communications*, vol. 51, no. 58, pp. 11619–11621, 2015, doi: 10.1039/c5cc03391h.

[153] H. Kim *et al.*, 'Microstructural adjustment of Ni–BaCe0.9Y0.1O3−δ cermet membrane for improved hydrogen permeation', *Ceramics International*, vol. 40, no. 3, pp. 4117–4126, Apr. 2014, doi: 10.1016/j.ceramint.2013.08.066.

[154] C. Zuo, T. H. Lee, S. E. Dorris, U. Balachandran, and M. Liu, 'Composite Ni–Ba(Zr0.1Ce0.7Y0.2)O3 membrane for hydrogen separation', *Journal of Power Sources*, vol. 159, no. 2, pp. 1291–1295, Sep. 2006, doi: 10.1016/j.jpowsour.2005.12.042.

[155] S. Fang, L. Bi, C. Yang, L. Yan, C. Chen, and W. Liu, 'H2S poisoning and regeneration of Ni–BaZr0.1Ce0.7Y0.2O3−δ at intermediate temperature', *Journal of Alloys and Compounds*, vol. 475, no. 1, pp. 935–939, May 2009, doi: 10.1016/j.jallcom.2008.08.070.

[156] S. Fang, K. S. Brinkman, and F. Chen, 'Hydrogen permeability and chemical stability of Ni–BaZr0.1Ce0.7Y0.1Yb0.1O3−δ membrane in concentrated H2O and CO2', *Journal of Membrane Science*, vol. 467, pp. 85–92, Oct. 2014, doi: 10.1016/j.memsci.2014.05.008.

[157] Q. A. Islam, M. W. Raja, and R. N. Basu, 'Zr- and Tb-doped barium cerate-based cermet membrane for hydrogen separation application', *Journal of the American Ceramic Society*, vol. 100, no. 4, pp. 1360–1367, 2017, doi: 10.1111/jace.14737.

[158] Z. Zhu *et al.*, 'Evaluation of hydrogen permeation properties of Ni–Ba(Zr0.7Pr0.1Y0.2)O3−δ cermet membranes', *International Journal of Hydrogen Energy*, vol. 39, no. 22, pp. 11683–11689, Jul. 2014, doi: 10.1016/j.ijhydene.2014.05.163.

[159] S.-Y. Jeon, D.-K. Lim, M.-B. Choi, E. D. Wachsman, and S.-J. Song, 'Hydrogen separation by Pd–CaZr0.9Y0.1O3−δ cermet composite membranes', *Separation and Purification Technology*, vol. 79, no. 3, pp. 337–341, Jun. 2011, doi: 10.1016/j.seppur.2011.03.018.

[160] Y.-C. Tsai *et al.*, 'Palladium based cermet composite for hydrogen separation at elevated temperature', *Journal of Power Sources*, vol. 274, pp. 965–970, Jan. 2015, doi: 10.1016/j.jpowsour.2014.10.085.

[161] W. A. Rosensteel and N. P. Sullivan, 'Fabrication and hydrogen permeation through novel BaZr0.9Y0.1O3−δ – Cu composite ceramic-metallic membranes', *International Journal of Hydrogen Energy*, vol. 42, no. 7, pp. 4216–4223, Feb. 2017, doi: 10.1016/j.ijhydene.2016.10.048.

[162] R. J. Gorte, S. Park, J. M. Vohs, and C. Wang, 'Anodes for Direct Oxidation of Dry Hydrocarbons in a Solid-Oxide Fuel Cell', *Advanced Materials*, vol. 12, no. 19, pp. 1465–1469, 2000, doi: 10.1002/1521-4095(200010)12:19<1465::AID-ADMA1465>3.0.CO;2-9.

[163] U. Balachandran, T. H. Lee, L. Chen, S. J. Song, J. J. Picciolo, and S. E. Dorris, 'Hydrogen separation by dense cermet membranes', *Fuel*, vol. 85, no. 2, pp. 150–155, Jan. 2006, doi: 10.1016/j.fuel.2005.05.027.

[164] H. Cheng *et al.*, 'Dual-layer BaCe0.8Y0.2O3-δ-Ce0.8Y0.2O2-δ/BaCe0.8Y0.2O3-δ-Ni hollow fiber membranes for H2 separation', *Journal of Membrane Science*, vol. 601, p. 117801, Mar. 2020, doi: 10.1016/j.memsci.2019.117801.

[165] J. S. Fish, S. Ricote, R. O'Hayre, and N. Bonanos, 'Electrical properties and flux performance of composite ceramic hydrogen separation membranes', *J. Mater. Chem. A*, vol. 3, no. 10, pp. 5392–5401, Feb. 2015, doi: 10.1039/C5TA00450K.

[166] W. A. Rosensteel, S. Ricote, and N. P. Sullivan, 'Hydrogen permeation through dense BaCe0.8Y0.2O3-δ - Ce0.8Y0.2O2-δ composite-ceramic hydrogen separation membranes', *International Journal of Hydrogen Energy*, vol. 41, no. 4, pp. 2598–2606, 2016, doi: 10.1016/j.ijhydene.2015.11.053.

[167] T. Wang *et al.*, 'SrCe0.95Y0.05O3−δ–ZnO dual-phase membranes for hydrogen permeation', *RSC Adv.*, vol. 6, no. 43, pp. 36786–36793, Apr. 2016, doi: 10.1039/C6RA02921C.

[168] S. Escolástico, C. Solís, C. Kjølseth, and J. M. Serra, 'Outstanding hydrogen permeation through CO2-stable dual-phase ceramic membranes', *Energy and Environmental Science*, vol. 7, no. 11, pp. 3736–3746, 2014, doi: 10.1039/c4ee02066a.

[169] T. Takahashi and H. Iwahara, 'Ionic conduction in perovskite-type oxide solid solution and its application to the solid electrolyte fuel cell', *Energy Conversion*, vol. 11, no. 3, pp. 105–111, Sep. 1971, doi: 10.1016/0013-7480(71)90121-5.

[170] J. W. Stevenson, T. R. Armstrong, D. E. McCready, L. R. Pederson, and W. J. Weber, 'Processing and Electrical Properties of Alkaline Earth-Doped Lanthanum Gallate', *J. Electrochem. Soc.*, vol. 144, no. 10, p. 3613, Oct. 1997, doi: 10.1149/1.1838057.

[171] K. Nomura and S. Tanase, 'Electrical conduction behavior in (La0.9Sr0.1)MIIIO3−δ (MIII=Al, Ga, Sc, In, and Lu) perovskites', *Solid State Ionics*, vol. 98, no. 3, pp. 229–236, Jun. 1997, doi: 10.1016/S0167-2738(97)00101-X.

[172] F. Chen and M. Liu, 'Study of transition metal oxide doped LaGaO3 as electrode materials for LSGM-based solid oxide fuel cells', *J Solid State Electrochem*, vol. 3, no. 1, pp. 7–14, Dec. 1998, doi: 10.1007/s100080050124.

[173] V. V. Kharton *et al.*, 'Ionic conductivity of La(Sr)Ga(Mg,M)O3−δ (M=Ti, Cr, Fe, Co, Ni): effects of transition metal dopants', *Solid State Ionics*, vol. 132, no. 1, pp. 119–130, Jul. 2000, doi: 10.1016/S0167-2738(00)00696-2.

[174] D. Lybye, F. W. Poulsen, and M. Mogensen, 'Conductivity of A- and B-site doped LaAlO3, LaGaO3, LaScO3 and LaInO3 perovskites', *Solid State Ionics*, vol. 128, no. 1, pp. 91–103, Feb. 2000, doi: 10.1016/S0167-2738(99)00337-9.

[175] V. Thangadurai and W. Weppner, 'Synthesis and Electrical Properties of K- and Pr-Substituted LaGaO3 and LaInO3 Perovskites', *J. Electrochem. Soc.*, vol. 148, no. 12, p. A1294, Nov. 2001, doi: 10.1149/1.1414286.

[176] S. Cheng, V. K. Gupta, and J. Y. S. Lin, 'Synthesis and hydrogen permeation properties of asymmetric proton-conducting ceramic membranes', *Solid State Ionics*, vol. 176, no. 35, pp. 2653–2662, Nov. 2005, doi: 10.1016/j.ssi.2005.07.005.

[177] S. Hamakawa, L. Li, A. Li, and E. Iglesia, 'Synthesis and hydrogen permeation properties of membranes based on dense SrCe0.95Yb0.05O3−α thin films', *Solid State Ionics*, vol. 148, no. 1, pp. 71–81, May 2002, doi: 10.1016/S0167-2738(02)00047-4.

[178] I.-M. Hung *et al.*, 'The proton conduction and hydrogen permeation characteristic of Sr(Ce0.6Zr0.4)0.85Y0.15O3−δ ceramic separation membrane', *Journal of the European Ceramic Society*, vol. 35, no. 1, pp. 163–170, Jan. 2015, doi: 10.1016/j.jeurceramsoc.2014.08.019.

[179] J.-H. Kim, Y.-M. Kang, B.-G. Kim, S.-H. Lee, and K.-T. Hwang, 'Preparation of dense composite membrane with Ba-cerate conducting oxide and rapidly solidified Zr-based alloy', *International Journal of Hydrogen Energy*, vol. 36, no. 16, pp. 10129–10135, Aug. 2011, doi: 10.1016/j.ijhydene.2011.02.145.

[180] Y. Wei, J. Xue, H. Wang, and J. Caro, 'Hydrogen permeability and stability of BaCe0.85Tb0.05Zr0.1O3−δ asymmetric membranes', *Journal of Membrane Science*, vol. 488, pp. 173–181, Aug. 2015, doi: 10.1016/j.memsci.2015.04.035.

[181] X. Meng *et al.*, 'Ni–BaCe0.95Tb0.05O3−δ cermet membranes for hydrogen permeation', *Journal of Membrane Science*, vol. 401–402, pp. 300–305, May 2012, doi: 10.1016/j.memsci.2012.02.017.

[182] Z. Zhu, W. Sun, L. Yan, W. Liu, and W. Liu, 'Synthesis and hydrogen permeation of Ni–Ba(Zr0.1Ce0.7Y0.2)O3−δ metal–ceramic asymmetric membranes', *International Journal of Hydrogen Energy*, vol. 36, no. 10, pp. 6337–6342, May 2011, doi: 10.1016/j.ijhydene.2011.02.029.

[183] M. Liu *et al.*, 'High-performance Ni–BaZr0.1Ce0.7Y0.1Yb0.1O3−δ (BZCYYb) membranes for hydrogen separation', *International Journal of Hydrogen Energy*, vol. 38, no. 34, pp. 14743–14749, Nov. 2013, doi: 10.1016/j.ijhydene.2013.09.057.

[184] C. K. Vigen and R. Haugsrud, 'Hydrogen flux in La0.87Sr0.13CrO3–δ', *Journal of Membrane Science*, vol. 468, pp. 317–323, Oct. 2014, doi: 10.1016/j.memsci.2014.06.012.

[185] G. C. Mather, D. Poulidi, A. Thursfield, M. J. Pascual, J. R. Jurado, and I. S. Metcalfe, 'Hydrogen-permeation characteristics of a SrCeO3-based ceramic separation membrane: Thermal, ageing and surface-modification effects', *Solid State Ionics*, vol. 181, no. 3, pp. 230–235, Feb. 2010, doi: 10.1016/j.ssi.2009.03.014.

[186] G. Zhang, S. Dorris, U. Balachandran, and M. Liu, 'Effect of Pd Coating on Hydrogen Permeation of Ni-Barium Cerate Mixed Conductor', *Electrochem. Solid-State Lett.*, vol. 5, no. 3, p. J5, Jan. 2002, doi: 10.1149/1.1446404.

[187] S. Escolástico, C. Kjølseth, and J. M. Serra, 'Catalytic activation of ceramic H2 membranes for CMR processes', *Journal of Membrane Science*, vol. 517, pp. 57–63, Nov. 2016, doi: 10.1016/j.memsci.2016.06.017.

[188] M. E. Ivanova *et al.*, 'Hydrogen separation through tailored dual phase membranes with nominal composition BaCe 0.8 Eu 0.2 O 3-δ :Ce 0.8 Y 0.2 O 2-δ at intermediate temperatures', *Scientific Reports*, vol. 6, no. 1, Art. no. 1, Nov. 2016, doi: 10.1038/srep34773.

[189] E. Mercadelli *et al.*, 'Production strategies of asymmetric BaCe0.65Zr0.20Y0.15O3-δ – Ce0.8Gd0.2O2-δ membrane for hydrogen separation', *International Journal of Hydrogen Energy*, vol. 45, no. 12, pp. 7468–7478, Mar. 2020, doi: 10.1016/j.ijhydene.2019.03.148.

[190] S. Escolástico, C. Solís, C. Kjølseth, and J. M. Serra, 'Catalytic Layer Optimization for Hydrogen Permeation Membranes Based on La5.5WO11.25-δ/La0.87Sr0.13CrO3-δ Composites', *ACS Appl. Mater. Interfaces*, vol. 9, no. 41, pp. 35749–35756, Oct. 2017, doi: 10.1021/acsami.7b08995.

[191] E. Mercadelli, D. Montaleone, A. Gondolini, P. Pinasco, and A. Sanson, 'Tape-cast asymmetric membranes for hydrogen separation', *Ceramics International*, vol. 43, no. 11, pp. 8010–8017, Aug. 2017, doi: 10.1016/j.ceramint.2017.03.099.

[192] A. Gondolini *et al.*, 'Development and hydrogen permeation of freeze-cast ceramic membrane', *Journal of Membrane Science*, vol. 684, p. 121865, Oct. 2023, doi: 10.1016/j.memsci.2023.121865.

[193] A. Gondolini, E. Mercadelli, S. Casadio, and A. Sanson, 'Freeze cast support for hydrogen separation membrane', *Journal of the European Ceramic Society*, vol. 42, no. 3, pp. 1053–1060, Mar. 2022, doi: 10.1016/j.jeurceramsoc.2021.10.063.

[194] S. Baumann, J. M. Serra, M. P. Lobera, S. Escolástico, F. Schulze-Küppers, and W. A. Meulenberg, 'Ultrahigh oxygen permeation flux through supported Ba0.5Sr0.5Co0.8Fe0.2O3−δ membranes', *Journal of Membrane Science*, vol. 377, no. 1, pp. 198–205, Jul. 2011, doi: 10.1016/j.memsci.2011.04.050.

[195] H. Diogrom, 'Experimental Results Plotted on [Hansen's] Phase Diagram'.

[196] D. Metal, 'Thermal Debinding and Sintering 101', Desktop Metal. Accessed: Sep. 26, 2023. [Online]. Available: https://www.desktopmetal.com/resources/sintering-101

[197] P. N. Plessow and F. Abild-Pedersen, 'Sintering of Pt Nanoparticles via Volatile PtO2 - Simulation and Comparison with Experiments'.

[198] A. Kaliyaraj Selva Kumar, Y. Zhang, D. Li, and R. G. Compton, 'A mini-review: How reliable is the drop casting technique?', *Electrochemistry Communications*, vol. 121, p. 106867, Dec. 2020, doi: 10.1016/j.elecom.2020.106867.

[199] J. Li, H. Yoon, and E. D. Wachsman, 'Hydrogen permeation through thin supported SrCe0.7Zr0.2Eu0.1O3−δ membranes; dependence of flux on defect equilibria and operating conditions', *Journal of Membrane Science*, vol. 381, no. 1, pp. 126–131, Sep. 2011, doi: 10.1016/j.memsci.2011.07.032.

[200] S. Zhan *et al.*, 'Preparation and hydrogen permeation of SrCe0.95Y0.05O3−δ asymmetrical membranes', *Journal of Membrane Science*, vol. 340, no. 1, pp. 241–248, Sep. 2009, doi: 10.1016/j.memsci.2009.05.037.

[201] Z. Zhu, L. Yan, H. Liu, W. Sun, Q. Zhang, and W. Liu, 'A mixed electronic and protonic conducting hydrogen separation membrane with asymmetric structure', *International Journal of Hydrogen Energy*, vol. 37, no. 17, pp. 12708–12713, Sep. 2012, doi: 10.1016/j.ijhydene.2012.06.033.

[202] A. Basile, Ed., 'Handbook of Membrane Reactors', in *Handbook of Membrane Reactors*, vol. 1, in Woodhead Publishing Series in Energy, vol. 1. , Woodhead Publishing, 2013, p. iv. doi: 10.1016/B978-0-85709-414-8.50020-1.

[203] G. Panomsuwan and H. Manuspiya, 'Correlation between size and phase structure of crystalline BaTiO3 particles synthesized by sol-gel method', *Mater. Res. Express*, vol. 6, no. 6, p. 065062, Mar. 2019, doi: 10.1088/2053-1591/ab101b.

[204] R. D. Deegan, O. Bakajin, T. F. Dupont, G. Huber, S. R. Nagel, and T. A. Witten, 'Capillary flow as the cause of ring stains from dried liquid drops', *Nature*, vol. 389, no. 6653, Art. no. 6653, Oct. 1997, doi: 10.1038/39827.

[205] H. B. Eral, D. J. C. M. 't Mannetje, and J. M. Oh, 'Contact angle hysteresis: a review of fundamentals and applications', *Colloid Polym Sci*, vol. 291, no. 2, pp. 247–260, Feb. 2013, doi: 10.1007/s00396-012-2796-6.

[206] H. Hu and R. G. Larson, 'Marangoni Effect Reverses Coffee-Ring Depositions', *J. Phys. Chem. B*, vol. 110, no. 14, pp. 7090–7094, Apr. 2006, doi: 10.1021/jp0609232.

[207] D. Tian, Y. Song, and L. Jiang, 'Patterning of controllable surface wettability for printing techniques', *Chem. Soc. Rev.*, vol. 42, no. 12, pp. 5184–5209, May 2013, doi: 10.1039/C3CS35501B.

[208] P. J. Yunker, T. Still, M. A. Lohr, and A. G. Yodh, 'Suppression of the coffee-ring effect by shape-dependent capillary interactions', *Nature*, vol. 476, no. 7360, Art. no. 7360, Aug. 2011, doi: 10.1038/nature10344.

[209] D. Mampallil, J. Reboud, R. Wilson, D. Wylie, D. R. Klug, and J. M. Cooper, 'Acoustic suppression of the coffee-ring effect', *Soft Matter*, vol. 11, no. 36, pp. 7207–7213, Sep. 2015, doi: 10.1039/C5SM01196E.

[210] E. I. Rogers, N. S. Lawrence, and R. G. Compton, 'The electrochemical oxidation of ruthenocene in various room temperature ionic liquids', *Journal of Electroanalytical Chemistry*, vol. 657, no. 1, pp. 144–149, Jul. 2011, doi: 10.1016/j.jelechem.2011.04.007.

[211] C. Batchelor-McAuley, L. M. Gonçalves, L. Xiong, A. A. Barros, and R. G. Compton, 'Controlling voltammetric responses by electrode modification; using adsorbed acetone to switch graphite surfaces between adsorptive and diffusive modes', *Chem. Commun.*, vol. 46, no. 47, pp. 9037–9039, Nov. 2010, doi: 10.1039/C0CC03961F.

[212] J. Bear, *Dynamics of Fluids in Porous Media*. Courier Corporation, 1988.

[213] W. M. Haynes, Ed., *CRC Handbook of Chemistry and Physics*, 95th ed. Boca Raton: CRC Press, 2014. doi: 10.1201/b17118.

[214] F. van der Leeden, F. L. Troise, and D. K. Todd, *Geraghty & Miller ground-water series*. Chelsea, MI, USA: Lewis, 1990.

[215] X. Shao *et al.*, 'Microchannel structure of ceramic membranes for oxygen separation', *Journal of the European Ceramic Society*, vol. 36, no. 13, pp. 3193–3199, Oct. 2016, doi: 10.1016/j.jeurceramsoc.2016.05.005.

[216] C. Gaudillere and J. M. Serra, 'Freeze-casting: Fabrication of highly porous and hierarchical ceramic supports for energy applications', *Boletín de la Sociedad Española de Cerámica y Vidrio*, vol. 55, no. 2, pp. 45–54, Mar. 2016, doi: 10.1016/j.bsecv.2016.02.002.

[217] X. Shao, D. Dong, G. Parkinson, and C.-Z. Li, 'Microstructure control of oxygen permeation membranes with templated microchannels', *J. Mater. Chem. A*, vol. 2, no. 2, pp. 410–417, Dec. 2013, doi: 10.1039/C3TA13744A.

[218] C. Peko, B. Groth, and I. Nettleship, 'The Effect of Polyvinyl Alcohol on the Microstructure and Permeability of Freeze-Cast Alumina', *Journal of the American Ceramic Society*, vol. 93, no. 1, pp. 115–120, 2010, doi: 10.1111/j.1551-2916.2009.03398.x.

[219] C. Gaudillere, J. Garcia-Fayos, M. Balaguer, and J. M. Serra, 'Enhanced Oxygen Separation through Robust Freeze-Cast Bilayered Dual-Phase Membranes', *ChemSusChem*, vol. 7, no. 9, pp. 2554–2561, 2014, doi: 10.1002/cssc.201402324.

[220] C. Gaudillere, J. Garcia-Fayos, and J. M. Serra, 'Enhancing oxygen permeation through hierarchically-structured perovskite membranes elaborated by freeze-casting', *J. Mater. Chem. A*, vol. 2, no. 11, pp. 3828–3833, Feb. 2014, doi: 10.1039/C3TA14069E.

[221] 'Learn About Natural Gas | Enbridge Gas'. Accessed: Oct. 07, 2021. [Online]. Available: https://www.enbridgegas.com/about-enbridge-gas/learn-about-natural-gas

[222] 'Hydrogen Production: Natural Gas Reforming', Energy.gov. Accessed: Oct. 07, 2021. [Online]. Available: https://www.energy.gov/eere/fuelcells/hydrogen-production-natural-gas-reforming

[223] S. Escolástico, C. Solís, and J. M. Serra, 'Study of hydrogen permeation in (La5/6Nd1/6)5.5WO12-δ membranes', *Solid State Ionics*, vol. 216, pp. 31–35, May 2012, doi: 10.1016/j.ssi.2011.11.004.

[224] S. Escolástico, C. Solís, and J. M. Serra, 'Hydrogen separation and stability study of ceramic membranes based on the system Nd5LnWO12', *International Journal of Hydrogen Energy*, vol. 36, no. 18, pp. 11946–11954, Sep. 2011, doi: 10.1016/j.ijhydene.2011.06.026.

[225] F. Schulze-Küppers *et al.*, 'Comparison of freeze-dried and tape-cast support microstructure on high-flux oxygen transport membrane performance', *Journal of Membrane Science*, vol. 564, pp. 218–226, Oct. 2018, doi: 10.1016/j.memsci.2018.07.028.

[226] "Sulfur Recovery Processes THE BASIC CLAUS PROCESS, 670".

[227] P. Nikolaidis and A. Poullikkas, "A comparative overview of hydrogen production processes," 2016, doi: 10.1016/j.rser.2016.09.044.

[228] J. Sehested, “Four challenges for nickel steam-reforming catalysts,” 2005, doi: 10.1016/j.cattod.2005.10.002.

[229] Pham, “THE NATIONAL MONUMURA UTTALE US009745191B2 (12) United States Patent,” 2017.

[230] “2) United States Patent (45) Date of Patent: (54) (71) (72) (73) (*) (21) (22) (65) (62) (51) (52,” 2015.

[231] “Coal utilization - Gasification | Britannica.” Accessed: Jan. 23, 2024. [Online]. Available: https://www.britannica.com/technology/coal-utilization/Gasification

[232] E. Baraj, K. Ciahotný, and T. Hlinčík, “The water gas shift reaction: Catalysts and reaction mechanism,” 2020, doi: 10.1016/j.fuel.2020.119817.

[234] G. Ertl, H. Knozinger, and J. Weitkamp, “Handbook of Heterogeneous Catalysis,” Mar. 2008, doi: 10.1002/9783527610044.

[235] A. Beck *et al.*, “The Extent of Platinum-Induced Hydrogen Spillover on Cerium Dioxide,” *ACS Nano*, vol. 17, pp. 1091–1099, 2023, doi: 10.1021/acsnano.2c08152.

[240] U. Unije, R. Mücke, P. Niehoff, S. Baumann, R. Vaßen, and O. Guillon, “Simulation of the effect of the porous support on flux through an asymmetric oxygen transport membrane,” 2016, doi: 10.1016/j.memsci.2016.10.037.

[241] P. Niehoff *et al.*, “Oxygen transport through supported Ba 0.5 Sr 0.5 Co 0.8 Fe 0.2 O 3Àd membranes,” 2013, doi: 10.1016/j.seppur.2013.07.002.

[242] S. Baumann *et al.*, “Influence of sintering conditions on microstructure and oxygen permeation of Ba 0.5 Sr 0.5 Co 0.8 Fe 0.2 O 3−ı (BSCF) oxygen transport membranes,” *J Memb Sci*, vol. 359, pp. 102–109, 2010, doi: 10.1016/j.memsci.2010.02.002.

[243] J. Sunarso *et al.*, “Mixed ionic-electronic conducting (MIEC) ceramic-based membranes for oxygen separation,” *J Memb Sci*, vol. 320, pp. 13–41, 2008, doi: 10.1016/j.memsci.2008.03.074.

[244] F. Schulze-K ¨ Uppers N, S. Baumann, W. A. Meulenberg, D. Stöver, S. Stöver, and H.-P. Buchkremer, “Manufacturing and performance of advanced supported Ba 0.5 Sr 0.5 Co 0.8 Fe 0.2 O 3 À d (BSCF) oxygen transport membranes,” 2013, doi: 10.1016/j.memsci.2013.01.028.

[245] F. Schulze-Küppers *et al.*, “Comparison of freeze-dried and tape-cast support microstructure on high-flux oxygen transport membrane performance,” 2018, doi: 10.1016/j.memsci.2018.07.028.

[246] Moulijn, J. A., Makkee, M., & van Diepen, A. E. (2013). Chemical Process Technology. In Chemical Process Technology. Wiley. https://www.wiley.com/en-us/Chemical+Process+Technology%2C+2nd+Edition-p-9781444320251